

Theory and Simulations of Nonlinear and Inelastic Processes in Relativistic Laser Plasma Interactions

Inaugural-Dissertation

zur

Erlangung des Doktorgrades der
Mathematisch-Naturwissenschaftlichen Fakultät
der Heinrich-Heine-Universität Düsseldorf

vorgelegt von

Anupam Karmakar
aus Burdwan, Indien

Düsseldorf

Mai, 2008

Aus dem Institut für theoretische Physik I
der Heinrich-Heine-Universität Düsseldorf

Gedruckt mit der Genehmigung der Mathematisch-Naturwissenschaftlichen Fakultät der
Heinrich-Heine-Universität Düsseldorf

Referent: Prof. Dr. Alexander Pukhov
Korreferent: Prof. Dr. K. H. Spatschek

Tag der mündlichen Prüfung: 30. 06. 2008

Theory and Simulations of Nonlinear and Inelastic Processes in Relativistic Laser Plasma Interactions

Anupam Karmakar
May, 2008

Institute for Theoretical Physics I
Heinrich-Heine University
Düsseldorf, Germany

*"To raise new questions, new possibilities, to regard old questions from a new angle,
requires creative imagination and marks real advances in science."*

– Albert Einstein

*Dedicated to my parents Mr. Phanibhusan Karmakar and Mrs. Sonali Karmakar,
the reason of my existence and the supreme support of my life.*

Contents

1	Introduction	11
1.1	Laser Plasma Interaction Physics : Motivation	11
1.2	Thesis Overview	12
1.3	A Brief Historical Overview	13
1.3.1	Plasma based particle acceleration	13
1.3.2	Advanced numerical methods for simulations	14
1.3.3	Relativistic electron beam propagation	15
1.4	Basic Laser-Plasma Interaction Physics	16
1.4.1	Optical field ionization	16
1.4.2	Plasma frequency and Debye length	19
1.4.3	Particle motion in an electromagnetic wave, relativistic threshold	20
1.4.4	Particle Acceleration Mechanisms	24
1.4.5	Weibel and Two-stream Instability	28
2	Acceleration of Electrons Using Ionization	33
2.1	Introduction	33
2.2	Implementation of Tunneling Ionization in VLPL Code	33
2.3	Collimated Attosecond GeV Electron Bunches	36
2.3.1	Electron acceleration from ionization of high-Z material	37
2.3.2	Radially polarized laser pulse	37
2.3.3	Single-cycle laser pulse	41
2.3.4	Acceleration by the Gaussian beam	43
2.3.5	Theoretical explanation	43
2.4	Hot Electron Production from Laser Irradiated Polystyrene Spheres . . .	45
2.4.1	Simulation of the Texas laser droplet interaction experiment . . .	45
2.5	Conclusion and Outlook	49
3	Collisions in Relativistic Laser-Plasma Interactions	51
3.1	Introduction	51
3.2	Numerical Simulation of Electron-Ion Binary Collisions	51
3.2.1	Implementation of the VLPL3d collision module	52
3.3	Benchmarking with Physical Processes	55
3.3.1	Scattering of hot electron beam in ambient collisional plasma . . .	55
3.4	Directed Acceleration of Electrons from Solid Surface	57
3.4.1	3D-PIC simulation of the experiment	58
3.5	Conclusion	65

Contents

4	Implicit PIC-Hydrodynamic Hybrid Simulation Code H-VLPL	67
4.1	Introduction: Motivation	67
4.2	The Hybrid Model	69
4.3	The Numerical Algorithm of H-VLPL	70
4.4	Numerical Dispersion and Stability	75
4.4.1	Dispersion relation for the x-component	75
4.4.2	Dispersion relation for the y- and the z-component	76
4.5	Benchmarking with Physical Processes	79
4.5.1	Reflection and refraction of incident pulse	80
4.5.2	Energy conservation	80
4.5.3	Acceleration of ions from a target back surface (TNSA)	82
4.5.4	Scaling of the skin fields	84
4.5.5	Collisional absorption	86
4.6	Conclusions and Outlook	87
5	Effects of Temperature and Collisions on the Weibel Instability	89
5.1	Introduction	89
5.2	Different Simulation Geometries	90
5.3	Details of the PIC Simulation Parameters	92
5.4	Simulation Results	92
5.4.1	Transverse geometry	92
5.4.2	Longitudinal geometry	98
5.4.3	Full 3D simulations	104
5.5	Analytical Model	105
5.6	Conclusion	110
6	Conclusion	111
	Appendix	113
A	Particle-in-cell (PIC) Simulation Codes	113
A.1	The Basic Equations	113
A.2	The Code VLPL	115
	References	117
	Index	137

1 Introduction

1.1 Laser Plasma Interaction Physics : Motivation

The advent of the chirped pulse amplification (CPA) [1] has made a breakthrough in the technological development of laser production by fabricating the way to produce ultra-short and extremely high power lasers with huge focus intensities. Since then the laser technology has progressed continuously and resulted in a dramatic increase of achievable powers and focus intensities as high as $10^{22}\text{W}/\text{cm}^2$ recently [2]. The very new Optical Parametric Chirped-pulse Amplification (OPCPA) technology is going to result in lasers of few cycle pulses at petawatt (10^{15} Watt) [3, 4] and even exawatt-class (10^{18} Watt) power level [5]. Whenever new intensity levels are achieved ever new physics can be studied with these laser systems.

In this context one should mention that the intensity 10^{16} W/cm² is the ionization threshold, above which the laser field becomes stronger than the atomic fields strength. This leads to instantaneous ionization of any material. Moreover, now-a-days even the table-top laser systems [6, 7] are capable of producing intensities $\sim 10^{18}$ W/cm². Beyond this intensity a fundamental threshold is crossed and the laser plasma interaction becomes relativistic, meaning the quiver velocity of the electrons in the electromagnetic field of the incident laser becomes comparable to the speed of light in vacuum. The physics of laser plasma interaction at intensities higher than 10^{18} W/cm² is extremely non-linear. As a consequence, analytical models of laser plasma interaction in this relativistic regime are highly complicated. The most dependable approaches in this regime are massively parallelized numerical simulations.

One of the most significant applications for such short ultra-intense laser pulses [1, 2] is the acceleration of charged particles [8–14] along a very short distance (precisely, a few hundred microns to couple of centimeters) into directed nano/atto-bunches with energies up to GeVs [12, 13]. Additionally, at these high intensities a series of physical processes like field ionization [15–20], electron-ion binary collision [21–24], collisional ionization [20, 25, 26], generation of quasistatic fields [27–31], pulse compression [32–34], front- and back-surface ion acceleration [35, 36], harmonics generation [37–39], x-ray production [40, 41], extreme pressure generation [42], and many other effects play a significant role. There are several possibilities to exploit these phenomena for high energy electron production [13, 43–46], directed acceleration of particles [14, 36, 47], etc. Moreover, the other very promising application for powerful short-pulse lasers is the so-called Fast-Ignition (FI) [48] scheme of the Inertial Confinement Fusion (ICF), where the transportation of a relativistic electron beam (REB) through an overdense background plasma is a challenging phenomena. However, this configuration is unstable and

sensitive to several instabilities, e.g. Weibel (filamentation) instability [49], two-stream instability [50–53], etc. Extensive understanding of the effects of background plasma collisions and transverse beam temperature in this context is extremely substantive.

On the other hand, the FI plasma has a density of the order of 1000 times compressed solid hydrogen, i.e., of the order of $10^5 n_c$, where $n_c = m_e \omega^2 / 4\pi e^2$ is the critical plasma density, m_e and e are the electron mass and charge and ω is the laser frequency. Similarly, there are increasing demands to simulate laser-solid interactions, where the densities vary over a range $100 - 1000 n_c$ [54]. The classical explicit particle-in-cell (PIC) methods are extremely computationally expensive as they have to resolve the plasma frequency $\omega_p = \sqrt{4\pi n_e e^2 / m_e}$, which is the frequency of the plasma electrostatic oscillations. Therefore, they are limited to be applied to systems with relatively low plasma densities only. Hence, looking from the computational point of view, the usability of classical PIC codes for simulating FI plasma as well as solid density plasmas is facing big question. Thus, developing an advanced and computationally efficient numerical technique, which can deal with virtually arbitrary densities, will be a significant development in the field of plasma simulations [55].

This thesis reports relativistic short-pulse laser-matter interactions concentrating on significant inelastic and nonlinear physical phenomena in high density regime, such as, tunneling ionization, binary collision, collimated attosecond GeV electron bunches production, directed acceleration of electrons, hot electron and x-ray generation, collisional Weibel and two-stream instabilities in the context of FI scheme. Furthermore, successful development of advanced numerical methods for the simulations of ultra-relativistic ultra-short pulse laser interactions with high density plasmas has also been incorporated. These new findings are anticipated to have crucial consequence on a number of practical applications in high energy nuclear physics, material science, ultrafast sciences, computational physics, energy production, radiation biology, molecular physics, etc.

1.2 Thesis Overview

This thesis consists of four major parts dealing with physical phenomena, which appear in laser-plasma interactions in the wide range of laser intensities $10^{16} - 10^{24}$ W/cm². In this work we primarily concentrate on the numerical simulations, however, all these numerical modelings are compared and supported by analytical calculations. Listed below are the topics covered in this thesis:

- The first part of the thesis is devoted to the study of tunneling ionization in relativistic short-pulse laser-plasma interactions, explained in Chapter 2. Developing an ionization module for the three dimensional Particle-in-cell (3D-PIC) code Virtual Laser Plasma Laboratory (VLPL) [see Appendix A for more details] is described in detail. A new concept of particle acceleration using the tunneling ionization of high-Z materials producing energetic electrons around 8 GeV has been studied. Particle acceleration using laser-plasma interaction physics has become a very well accepted mainstream subject recently.

1.3. A Brief Historical Overview

- Chapter 3 deals with the physics of binary collisions in relativistic laser-plasma interactions. Details of implementation and benchmarking of the binary collision module developed by the author for the 3D-PIC code VLPL is reported therein. This collision module has been used in the kinetic plasma simulations to study directed acceleration of electrons from a solid target surface by sub-10-fs laser pulses.
- The third topic is the development of the semi-implicit particle-in-cell (PIC)-hydrodynamic hybrid simulation code, Hybrid Virtual Laser Plasma Laboratory (H-VLPL), for simulating solid state densities and Fast Ignition (FI) plasmas. In the last couple of years there has been an increasing demand to simulate these extremely high density plasmas. The details of the hybrid model, numerical scheme, numerical stability and physical benchmarkings of the code H-VLPL, have been considered in Chapter 4. Development of a code which can deal with virtually arbitrary densities is a remarkable step forward in the computational high-density plasma physics.
- In the last chapter of this thesis we study the extremely significant key topic related to Fast Ignition (FI). The effects of relatively high beam temperature and ambient plasma collisions on Weibel and two-stream instabilities are studied, both numerically and analytically, using a computationally efficient simulation model. An in-depth report on all these works is discussed in Chapter 5.

1.3 A Brief Historical Overview

1.3.1 Plasma based particle acceleration

In the last decade the laser technology has developed extensively and presently able to produce few-cycle pulses of focused intensities $\sim 10^{22}$ W/cm² [2]. The electric field associated with these ultra-intense laser systems, $I > 10^{18}$ W/cm², is huge and if could be utilized, can accelerate charged particles up to relativistic energies very easily [11]. However, using the laser electric field is not straightforward, as the field is fast oscillating and always perpendicular to the wave propagation [77]. Tajima and Dawson [8] proposed a way to overcome this difficulty by using the longitudinal plasma waves excited by laser beams to accelerate electrons.

Plasma based particle accelerators are of great interest because of their ability to sustain extremely large acceleration gradients. The accelerating gradient in conventional accelerators are limited due to breakdown which occurs on the walls of the structure [66]. Plasmas, however, can sustain electron plasma waves with electric field of the order of the non-relativistic wave breaking field [78, 79], given by

$$E_0 \text{ [V/cm]} \approx 0.96n_0^{1/2} \text{ [cm}^{-3}\text{]} \quad (1.1)$$

where n_0 is the ambient electron density. For overdense plasmas, the electron densities can be much higher than $n_c \sim 10^{21} \text{ cm}^{-3}$, which results in the plasma fields a few orders of magnitude greater than those in a conventional accelerator. The relativistic plasma electrons run with the plasma wave with nearly the same speed and get accelerated to very high energies. Some of the well established and experimentally achieved acceleration schemes are laser wakefield accelerators (LWFA) [8, 80], plasma beat-wave accelerators (PBWA) [8, 81]. But, for last couple of years, the “bubble regime” [11] (see 1.4.4) of electron acceleration proved to be very efficient due its mono-energetic nature of the energy spectrum of accelerated electrons and easy attainability. Another, mechanism of electron acceleration, which exploits the properly manipulated laser beams (radially polarized, Bessel pulse etc.) has also opened a new way to achieve very high energy and high charge electron bunches [13, 46, 82] (for details see Chapter. 2 of this thesis). In addition, there have been some significant successes in ion acceleration in the recent past from target back surface by the so-called Target Normal Sheath Acceleration (TNSA) [35, 36] and also from the front surface [83].

Presently, electron energies from 100 MeV [68, 84, 85] up to GeV [12, 86–89] have been achieved in the bubble regime of particle acceleration in plasmas [44]. When the laser pulse propagates in plasmas, its transverse electric field is converted into the longitudinal field of the plasma wave, which accelerates the particles. However, the next generation of the short pulse lasers is designed to achieve focal intensities of 10^{24} W/cm^2 , or even higher. The natural question is arising if these laser fields can accelerate particles to high energies directly, without any conversion to plasma fields. Further discussion on this topic will be carried out in Chapter 2.

1.3.2 Advanced numerical methods for simulations

Numerical simulations are an integrated part of plasma research. It has been proved to be very important for both theoretical and experimental studies. Some of the remarkable physical processes in the laser-plasma physics have been discovered through numerically predicted consequences. Plasma simulations can be divided into two main categories: kinetic and fluid. The kinetic simulations follow the plasma in a 6D phase space and very efficiently simulate the phenomena like laser-plasma interactions. On the contrary, fluid simulations integrate over velocity space to maintain only mean particle velocity and temperature. Fluid codes are widely used to simulate huge complex experiments such as tokamak and astrophysical processes like gamma ray bursts and supernovae [90]. Kinetic simulations, on the contrary, has been a major tool in the research of laser-plasma interaction physics [91, 92].

In the last decade, particle-in-cell (PIC) methods, initially proposed by Dawson [93] and later developed and coded exclusively by Birdsall and others [91, 92], proved to be a very reliable and successful method for kinetic simulations [11]. Large full 3D parallel electromagnetic simulation codes like VLPL [95], OSIRIS [96], VORPAL [97], OOPIC [98], and others have influenced outstandingly the development of extremely nonlinear laser-plasma interaction physics. But, as new physical processes and simulating high density plasmas are becoming very common now-a-days, the need for de-

veloping new numerical techniques and large computational powers are becoming evident. Fortunately, the boundaries of what is possible are always advancing by virtue of Moore's law [99]. The PIC-hydrodynamic hybrid simulation codes [55], implicit PIC algorithms [160], quasi-static PIC algorithm [100], etc. have evolved as an innovative solution to meet the growing need to model very high (solid) density plasmas [54] and FI plasmas [153]. In this connection, it is worthwhile to state here that, Chapter 4 of this thesis is devoted to elaborately discuss the numerical algorithms and benchmarking of the newly developed PIC-hydrodynamic code H-VLPL [55]. On the other hand there has been a significant development on the nonlinear wave equation solver for the laser propagation in a relativistic plasma by proposing a new variant of the Gautschi-type integrator for reducing the number of time steps [101].

1.3.3 Relativistic electron beam propagation

In the context of FI, propagation of laser-generated relativistic electron beam through an over-dense plasma to heat the hot-spot in the core of a pre-compressed fusion fuel target [48], is of extreme importance. On the other hand, the maximum electron current achievable in vacuum is limited by the Alfvén current limit $J_A = (mc^3/e)\gamma = 17\gamma kA$, where m is the electron mass, e is the electronic charge. The forward electron current carried by the these beam electrons, which is higher than the Alfvén limit, is compensated by a return plasma current, thus maintaining the global charge neutrality. This system of beam and a compensating plasma current is unstable and subject to Weibel (filamentation) and the two-stream instabilities. The Weibel instability, first predicted by E. S. Weibel [49], has been studied rigorously in laser plasma interactions [105], and also in the astrophysical scenario [70, 74, 75]. Over a long time the research of Weibel instability has been the main subject for several analytical and numerical [106, 107, 111–119] as well as experimental studies [108–110]. A kinetic modeling of the Weibel instability in the context of charged particle beam transport in accelerator physics have been developed Yoon *et al.* [112]. Nonlinear dynamics of the beam filaments have been studied in [102] and later including movable ions in [103, 116]. The effects of the Rutherford scattering on the Weibel instability were investigated using simulations in [23]. More recently, to study this instability in linear regime a number of theoretical models, both kinetic and hydrodynamic, have been developed [113–115]. A very significant study of the collective stopping of the beam and ion heating in the context of FI have been done by Honda *et al.* [116]. Some current research works have been performed using three-dimensional simulations of resistive beam filamentation focused on the ignition-scale FI configuration [117]. Structures of magnetic fields generated due to the Weibel instability in a collisionless plasma have also been investigated in real three-dimensions by Califano *et al.* [118]. Lately, a series of experiments reported the evidence of Weibel-like dynamics and filamentation of electron beams [108–110]. Modeling for characterization of the initial filamentation of the relativistic electron beam passing through a plasma have also been performed [115] and saturated magnetic fields were studied with numerical simulations in [104]. There are several facts about the physics of the Weibel instability, which are yet to be explored. Such a task, simultaneous effects of plasma collisions and

beam temperature on the Weibel instability will be reported in this thesis in Chapter 5.

1.4 Basic Laser-Plasma Interaction Physics

1.4.1 Optical field ionization

For a laser pulse with extremely high intensity, the corresponding electric and magnetic fields are also massive. This order of intensities is fairly comparable with the inner-atomic field strengths. For the first Bohr's orbit of hydrogen atom this atomic field strength can be estimated as:

$$E_a = \frac{e}{r_B^2} \approx 5.1 \times 10^9 \text{ V/cm}, \quad (1.2)$$

where the Bohr radius

$$r_B = \frac{\hbar^2}{m_e c^2} \approx 5 \times 10^{-9} \text{ cm}. \quad (1.3)$$

The laser pulse intensity corresponding to this atomic field E_a is given by

$$I_{\text{atomic}} = \frac{cE_a^2}{8\pi} \approx 3.4 \times 10^{16} \text{ W/cm}^2. \quad (1.4)$$

This intensity is considered to be the threshold for ionization, as any laser with $I > I_a$ can immediately ionize atoms. Precisely, the mechanism of ionization is very much intensity dependent.

The actual mechanism of ionization in that particular intensity is determined by so-called Keldysh parameter Γ [56]:

$$\Gamma^2 = \frac{I_p}{2\epsilon_{os}}, \quad (1.5)$$

where I_p is the ionization potential and ϵ_{os} is the quiver energy of the electron in the laser pulse with field E and carrier frequency ω . The quiver energy is defined by the formula

$$\epsilon_{os} = \frac{e^2 E^2 (1 + \alpha^2)}{4m_e \omega^2} \quad (1.6)$$

where the parameter $\alpha = 0$ for linear polarization and $\alpha = 1$ for circular polarization. When the value of Keldysh parameter is large, $\Gamma \gg 1$ the mechanism ionization is dominated by multiphoton ionization, whereas, for $\Gamma \ll 1$, optical field ionization (OFI)

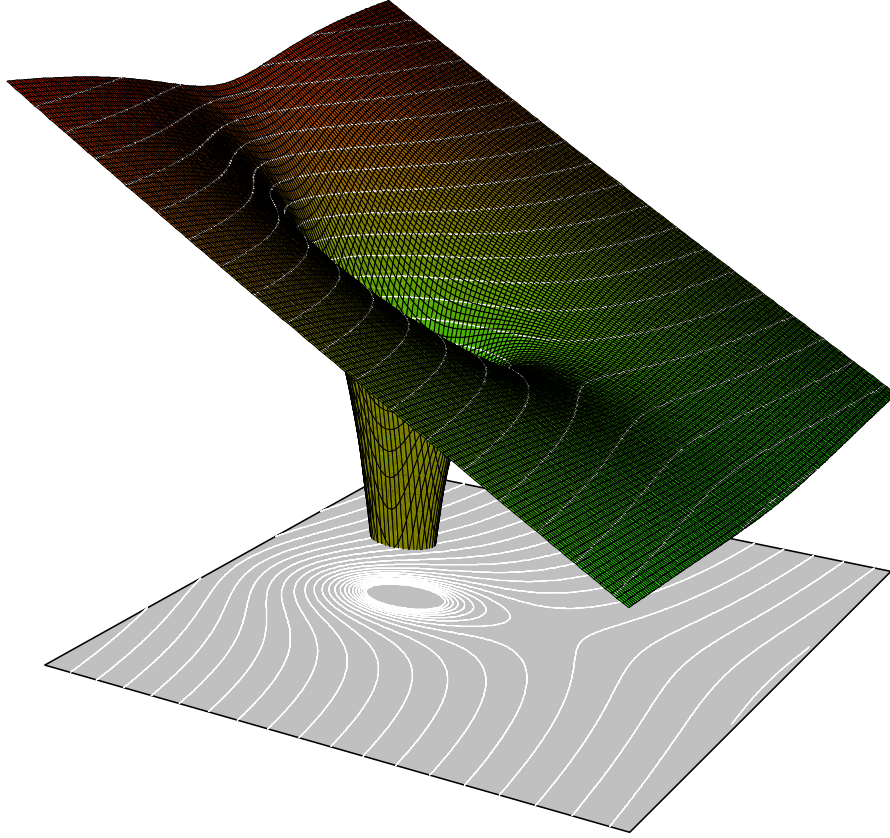


Figure 1.1: A 3D perspective of barrier suppression (BSI) and tunneling ionization: perturbed atomic potential-well when a strong field is applied. An electron sitting inside the potential well has two possibilities to come out from the atomic structure depending upon the intensity of the applied optical field.

almost instantly knocks out the electrons from the atomic levels ensuing plasma formation. This optical field ionization (OFI) can occur in two different mechanisms: barrier suppression ionization (BSI) and tunneling ionization.

A 3D perspective of the atomic potential-well distorted by application of a strong optical field is presented in Fig. 1.1. An electron sits inside the unperturbed atomic potential well on an energy level I_p . Considering the atomic transition frequency is much lower than the laser frequency, the electric field of the laser is normally considered to be static. The applied laser field distorts the atomic potential-well and lowers the potential barrier seen by an electron in the atom/ion. As a result the electron is free to come out of the atomic structure. When the field is strong enough the potential barrier is suppressed below the electron energy level, freeing the electron (see Fig. 1.2). Moreover, the quasi-classical approximations, $\hbar\omega \ll I_p$ and $E \ll E_a$ ($\hbar\omega$ is the emitted photon energy, I_p is the energy of the considered state) has to be satisfied. One can also easily estimate a threshold field $E = I_p^2/(4Z)$ [17], where, Z is the ionic charge. The corresponding threshold laser intensity can be calculated as:

1. Introduction

$$I_{BSI}(\text{W/cm}^2) = 4.00 \times 10^9 \frac{I_p^4(\text{eV})}{Z^2}. \quad (1.7)$$

In the case when the suppression of the Coulomb potential barrier is not able to free the electron, it still has a non-zero quantum mechanical probability of escaping. This process is called tunneling Ionization, illustrated physically in Fig. 1.2. Though this is forbidden by classical laws, it is a predominant effect in the field induced ionization dynamics. Evidently, there has to be a tunneling ionization probability, which is more complex than the rather straightforward ionization mechanism.

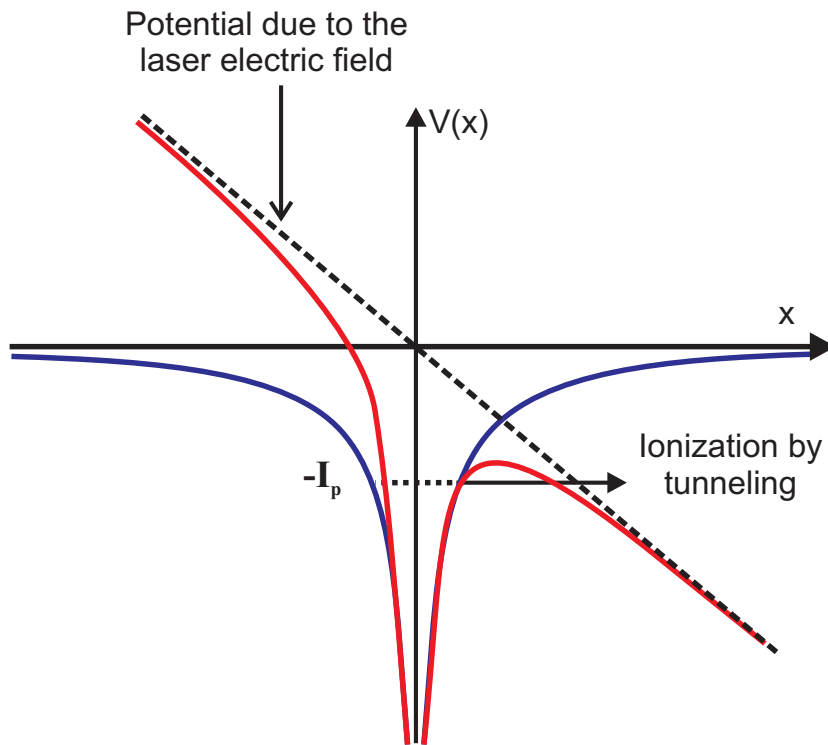


Figure 1.2: A simple illustration of tunneling ionization mechanism. The electric field bends the Coulomb potential to form a barrier through which the electron can tunnel.

There were several attempts for calculating the probability of ionization [15, 56], but the most widely accepted and experimentally verified theory comes from the work of Ammosov, Delone and Krainov, widely known as *ADK-theory* [16]. Considering an external field of the form

$$E = E_0 \cos(\omega t), \quad (1.8)$$

the tunneling probability of the electron located in the Coulomb potential of a complex atom/ion is given by ADK model as:

1.4. Basic Laser-Plasma Interaction Physics

$$W_{\text{ADK}} [s^{-1}] = \omega_A C_{n^*l} f(l, m) I_p \left(\frac{3E}{\pi(2I_p)^{3/2}} \right)^{1/2} \left[\frac{2}{E} (2I_p)^{3/2} \right]^{2n^* - |m| - 1} \quad (1.9)$$

$$\times \exp \left(-\frac{2}{3E} (2I_p)^{3/2} \right)$$

where $\omega_A = 4.134 \times 10^{16} \text{ sec}^{-1}$ is the atomic unit of frequency, E is the laser field in atomic units. The factors f and C are given by

$$f(l, m) = \frac{(2l+1)(l+|m|)!}{2^{|m|}(|m|)!(l-|m|)!}$$

and

$$C_{n^*l} = \left(\frac{2e}{n^*} \right)^{n^*} \frac{1}{(2\pi n^*)^{1/2}}.$$

Here n^* is the effective principal quantum number, l and m are magnetic and orbital quantum numbers, and e is the Euler number.

At this point, we leave this preliminary discussion with the introduction of ADK theory. A more elaborate discussion on tunneling ionization emphasizing on ADK probability will be considered in Chapter 2.

1.4.2 Plasma frequency and Debye length

Due to long-range forces between plasma particles, a plasma behaves in some situations as a system of coupled oscillators. One basic characteristic of oscillation of the plasma state is the electron plasma frequency ω_{pe} , defined as [57]

$$\omega_{pe} = \sqrt{\frac{4\pi n_e e^2}{m_e}}, \quad (1.10)$$

n_e is the particle number density, and m_e is the electron mass. It is customary to call electron plasma frequency ω_{pe} as plasma frequency ω_p as the electrons are lightest particles in a plasma.

In case of ions, one can define the ion plasma frequency as

$$\omega_{pi} = \sqrt{\frac{4\pi Z^2 e^2 n_i}{m_i}}, \quad (1.11)$$

where Ze and n_i are the ion charge and density, respectively. Using the plasma quasi-neutrality condition, one can compare the electron and ion plasma frequency as

$$\frac{\omega_{pi}}{\omega_{pe}} = \sqrt{\frac{m_e}{m_i}} \ll 1. \quad (1.12)$$

1. Introduction

The plasma frequency is often used as a means of specifying the electron density in plasma. It also gives a measure of Debye length, the characteristic length which an electron or ion moving with thermal speed $v_{th} = \sqrt{k_B T / m_e}$ to travel in during the interval of one plasma frequency (ω_p^{-1}). Debye length is defined as

$$\lambda_D = \sqrt{\frac{k_B T}{4\pi n_e e^2}}, \quad (1.13)$$

where k_B is the Boltzmann constant.

1.4.3 Particle motion in an electromagnetic wave, relativistic threshold

Plane electromagnetic wave

A plane electromagnetic wave can be described by its vector potential

$$\mathbf{A}(\mathbf{r}, t) = \text{Re}\{\mathbf{A}_0 \exp i\psi\}, \quad (1.14)$$

where $\mathbf{A}_0 = A_0 \hat{e}_y$ is the laser amplitude for linear polarization (LP) and $\mathbf{A}_0 = A_0(\hat{e}_y \pm i\hat{e}_z)$, (\hat{e}_x , \hat{e}_y and \hat{e}_z are system of unit vectors), for circular polarization (CP) with + and - for right and left-circular polarization, respectively; $\psi = \mathbf{k}\mathbf{r} - \omega t$ is the phase; \mathbf{k} is the wave vector; \mathbf{r} and t are space and time coordinate. The dispersion relation in vacuum is

$$\omega = kc, \quad (1.15)$$

where c is the speed of light and $k = |\mathbf{k}|$. Introducing the wavelength $\lambda = cT = 2\pi c/\omega$, one can rewrite Eq. (1.15) as

$$k = \frac{2\pi}{\lambda} \quad (1.16)$$

Here, we use the standard *Coulomb gauge*, i.e. $\text{div } \mathbf{A} = 0$. Then, the expression for electric field \mathbf{E} and magnetic field \mathbf{B} take the form

$$\begin{aligned} \mathbf{E} &= -\frac{1}{c} \frac{\partial \mathbf{A}}{\partial t} \\ \mathbf{B} &= \text{rot } \mathbf{A}. \end{aligned} \quad (1.17)$$

Using the Poynting vector $\mathbf{S} = (c/4\pi)\mathbf{E} \times \mathbf{B}$, one can write the intensity of light as

$$I = |\mathbf{S}| = \frac{\omega k}{8\pi} A_0^2 \times \begin{cases} (1 + \sin 2\psi), & \text{for LP,} \\ 2, & \text{for CP.} \end{cases} \quad (1.18)$$

1.4. Basic Laser-Plasma Interaction Physics

One has to remember here that the intensity oscillates with twice the phase for linear polarization, while it is independent of the phase for circular polarization. This is a significant factor to make difference when interaction with matter occurs. The intensity averaged over the phase is then given by

$$I = \frac{1}{2\pi} \int_0^{2\pi} I(\psi) d\psi = \zeta \frac{\omega k}{8\pi} A_0^2 \quad (1.19)$$

The factor $\zeta = 1$ for linear polarization and $\zeta = 2$ for circular polarization. Using 1.16 one gets

$$I\lambda^2 = \zeta \frac{\pi}{2} c A_0^2. \quad (1.20)$$

When the electrons caught by the light wave acquire the velocity of light, the relativistic threshold intensity is reached. In non-relativistic case ($\mathbf{v} \ll c$), the motion equation of an electron

$$m \frac{d\mathbf{v}}{dt} = -e \left(\mathbf{E} + \frac{\mathbf{v}}{c} \times \mathbf{B} \right) \approx -e\mathbf{E} \quad (1.21)$$

has the integrals

$$v = \text{Re} \left\{ \frac{e\mathbf{E}}{im\omega} \right\} = -\frac{eA_0}{mc} \begin{cases} \hat{e}_y \cos \psi, & \text{for LP;} \\ (\hat{e}_y \cos \psi \mp \hat{e}_z \sin \psi), & \text{for CP.} \end{cases} \quad (1.22)$$

$$r = \text{Re} \left\{ \frac{e\mathbf{E}}{m\omega^2} \right\} = -\frac{eA_0}{mc} \begin{cases} \hat{e}_y \sin \psi, & \text{for LP;} \\ (\hat{e}_y \sin \psi \mp \hat{e}_z \cos \psi), & \text{for CP.} \end{cases} \quad (1.23)$$

Using *dimensionless light amplitude*

$$a_0 = -\frac{eA_0}{mc^2} \quad (1.24)$$

one can rewrite the previous Eq. (1.20) as

$$I_0\lambda^2 = \zeta \frac{\pi}{2} P_0^2 A_0^2 = \zeta \left[1.37 \times 10^{18} \frac{\text{W}}{\text{cm}^2 \mu\text{m}} \right] a_0^2 \quad (1.25)$$

When the quiver velocity of the electron approaches c , the relativistic threshold is reached, i.e. $a_0 = 1$. Surely, at this condition the trajectory of the electron alters from a simple transverse oscillations described above. This will be discussed in the next part of this Section 1.4.3.

From Eq. (1.25) the relativistic power comes out as

1. Introduction

$$P_0 = \frac{mc^2}{e^2/mc^3} = \frac{mc^5}{e^2} = 8.67 \text{ GW}, \quad (1.26)$$

which may be written as the product of the voltage $mc^2/e = 511 \text{ keV}$ corresponding to the rest energy of the electron and the current unit $J_0 = mc^3/e = 17 \text{ kA}$, which is related to Alfvén current $J_A = J_0\beta\gamma$ with $\beta = v/c$ and $\gamma = 1/\sqrt{1-\beta^2}$. Any current larger than this can not at all be transported in vacuum due to magnetic *self-interactions*. This phenomenon is very important in the physics of Weibel instability, which will be discussed in Chapter 5.

Free particle motion in an electromagnetic wave

Let us now consider the motion of a relativistic particle in the plane light wave of arbitrary amplitude. The relativistic Lagrange function of a particle with mass m and charge q moving in an electromagnetic field with potential ϕ and vector-potential A is given by

$$L(\mathbf{r}, \mathbf{v}, t) = -mc^2\sqrt{1 - \frac{v^2}{c^2}} + \frac{q}{c}\mathbf{v} \cdot \mathbf{A} + q\phi \quad (1.27)$$

From the Euler-Lagrange equation

$$\frac{d}{dt} \frac{\partial L}{\partial \mathbf{v}} - \frac{\partial L}{\partial \mathbf{r}} = 0 \quad (1.28)$$

we obtain the relativistic equation of motion of the particle

$$\frac{d\mathbf{p}}{dt} = q \left(\mathbf{E} + \frac{\mathbf{v}}{c} \times \mathbf{B} \right). \quad (1.29)$$

Here, the full canonical momentum is $\mathbf{p} = \partial L / \partial \mathbf{v} = m\gamma\mathbf{v} + q\mathbf{A}/c = \mathbf{p} + q\mathbf{A}/c$, where $\gamma = 1/\sqrt{1-v^2/c^2}$.

Following [58, 59] we proceed to discuss the solution of Eq. (1.28). For a plane wave, there exists two different symmetries, which provides two constants of motion. The first symmetry appears from the plane wave planar symmetry. Planar symmetry implies $\partial L / \partial \mathbf{r}_\perp = 0$ and hence, conservation of the perpendicular component of the canonical momentum.

$$\frac{\partial L}{\partial \mathbf{v}_\perp} = \mathbf{p}_\perp + \frac{q}{c}\mathbf{A}_\perp = \text{const.} \quad (1.30)$$

The second symmetry appears from the fact, that the laser pulse propagates with a constant phase velocity v_{ph} (in vacuum $v_{ph} = c$) and considering an infinite wave form

1.4. Basic Laser-Plasma Interaction Physics

of $\mathbf{A} = \mathbf{A}(t - x/v_{ph})$. We introduce the Hamiltonian function $\mathbf{H}(\mathbf{x}, \mathbf{p}, t) = E(t)$ [60], which actually refers the total time-dependent energy of the particle. Thus, taking into account $\partial\mathbf{H}/\partial t = -\partial L/\partial t$ and $A_x = 0$ for plane wave, one obtains

$$\frac{\partial E}{\partial t} = -\frac{\partial L}{\partial t} = c\frac{\partial L}{\partial x} = c\frac{d}{dt}\frac{\partial L}{\partial v_x} = c\frac{dp_x^{\text{can}}}{dt} = c\frac{dp_x}{dt}. \quad (1.31)$$

Hence, from this we obtain the second invariant

$$E - cp_x = \text{const.}, \quad (1.32)$$

and, for the electrons initially at rest, the kinetic energy

$$E_{\text{kin}} = E - mc^2 = (\gamma - 1)mc^2 = p_x c. \quad (1.33)$$

Using the relation $E = mc^2\gamma = \sqrt{(mc^2)^2 + p^2c^2}$, one can obtain the expression for kinetic energy as

$$E_{\text{kin}} = \frac{p_x^2}{2m} = \frac{a^2}{2}mc^2. \quad (1.34)$$

A very crucial observation here is that, E_{kin} is directly linked to the amplitude of the light wave a and retreats back to zero as soon as the electron leaves the light field. But in case of real experimental configurations, due to finite beam radius etc., the electron breaks the planar symmetry and obtains a net energy gain.

Relativistic threshold

For $a_0 \sim 1$ we can see from Eq. (1.34), that $E_{\text{kin}} \sim mc^2$. The corresponding intensity I_0 (for a specific λ) is normally considered as the relativistic threshold for a particular sort of particles. In case of motion of electrons this amplitude $a_0 = 1$ corresponds to a laser intensity

$$I_0\lambda^2 = 1.37 \times 10^{18} \text{W cm}^{-2} \mu\text{m}^2. \quad (1.35)$$

One needs to explain the physical significance of this threshold. When $|a| < 1$, i.e. $v_{\perp} \ll c$, the particles oscillate mainly in the direction of laser polarization with a small ponderomotive drift along the wave propagation direction. On the contrary, in the relativistic regime, i.e. $|a| > 1$ and $v_{\perp} \sim c$, the laser ponderomotive force $\mathbf{v} \times \mathbf{B}/c$ pushes the particle forward and under this condition the relativistic motion of the particle become primarily longitudinal.

1. Introduction

Focused laser pulse

In real experiments the laser pulses are not plane waves, rather tightly focused. Near the focal plane, one can write

$$\mathbf{A} = \mathbf{A}(\zeta_g, \mathbf{r}) \exp(k\zeta_{ph}) \quad (1.36)$$

where,

$$\zeta_{ph} = z - v_{ph}t, \quad \zeta_g = z - v_g t.$$

The phase velocity $v_{ph} > c$ and the group velocity $v_g < c$. It follows from the Coulomb gauge condition $\nabla \cdot \mathbf{A} = 0$, that the focused electromagnetic wave has not only the transverse component of the vector potential, but also the longitudinal one

$$\partial_z A_z = -\nabla_{\perp} \cdot A_{\perp}. \quad (1.37)$$

Due to interaction with the focused laser pulse in vacuum, the particles get scattered out from the focal plane. There is no general exact analytical solution for particles' motion in this case. But, for low laser intensities $a \ll 1$, the particle momentum $\bar{\mathbf{p}}$, averaged over the laser period can be described introducing the so-called *relativistic ponderomotive force* (RPF) (see [61] for details) as

$$F_{pond} = \frac{d\bar{\mathbf{p}}}{dt} = -mc\nabla \frac{\bar{p}^2}{2}. \quad (1.38)$$

This concept is valid only if the laser wave amplitude is a slow varying one compared to the phase of the wave. One can see from Eq. (1.38), that the electrons are expelled from the regions of high intensity as the RPF is independent of the laser polarization. It has been shown [62, 63] that the RPF model is still valid even at higher intensities. Hence, Eq. (1.38) takes the form

$$\frac{d\bar{\mathbf{p}}}{dt} = -\frac{mc^2}{\bar{\gamma}} \nabla \bar{\gamma}. \quad (1.39)$$

It has been described by Quensel *et al.* [63] that this process depends upon the dimensionless parameter $\alpha = k\sigma/(1 - v_z/c)$. If $\alpha \ll 1$ the scattering of the electron remains ponderomotive, whereas, in the opposite case, $\alpha > 1$, the electron motion is overcomplicated and polarization asymmetries come into play.

1.4.4 Particle Acceleration Mechanisms

Direct laser acceleration (DLA)

The proposal of direct laser acceleration has initially been predicted from numerical studies of [64]. The underlying physics behind this mechanism is, that the electrons,

1.4. Basic Laser-Plasma Interaction Physics

when propagating in a plasma channel, can resonantly interact with the laser wave propagating in the same direction. These electrons get kicked out from the channel by the ponderomotive force creating a radial electrostatic field. Simultaneously, the light propagating in the channel pushes the electrons in forward direction, which produces a current. An azimuthal magnetic field is generated as a result of this current.

If one approximates the laser plasma channel as a cylinder with uniform electron density $N_e = fN_0$ ($0 \leq f \leq 1$), the radial electric field can be written as

$$-eE_r = (1 - f) \frac{m\omega_{pe}^2}{2} r, \quad (1.40)$$

where ω_{pe} is the electron plasma frequency. Now, the current $-efN_0c$ produces the corresponding azimuthal magnetic field, estimated as

$$-eB_\phi = f \frac{m\omega_{pe}^2}{2} r. \quad (1.41)$$

Hence, in this kind of ideal plasma channel, the motion equation of the electron can be written as

$$m\gamma \frac{d^2 r}{dt^2} = -eE_r - eB_\phi. \quad (1.42)$$

One can calculate the oscillation frequency of the electron, the so-called betatron frequency, as

$$\omega_\beta = \frac{\omega_{pe}}{\sqrt{2}\gamma}. \quad (1.43)$$

In this simplified model the fields operate in such a manner, that the propagation of electrons is mainly confined along the channel axis, on the other hand, the channel works merely as a potential well. In this potential well the electrons get trapped and oscillate radially with a frequency $\approx \omega_\beta$.

As the electrons propagate along channel axial direction with a velocity v_z , they go through a strong down shift of optical frequency. Selection of proper conditions can make the transverse betatron oscillations to be in resonance with the laser. This permits the laser field to drive a fraction of the electrons resonantly.

We note here once again, that the electron oscillations are directed along the laser polarization. In this situation, the electrons can gain energy two times of the laser period due to energy coupling. As a consequence of this, the transverse velocity v_\perp oscillates according to the laser period, whereas, the longitudinal velocity oscillates twice during the whole laser period. This phenomenon results in bunching of electrons in space twice every laser period. It has already been shown in both experiments and simulations,

1. Introduction

that the conversion efficiency in this mechanism goes up to 30-40% [11]. These electrons usually have quasi-static energy spectra, which can be characterized by an exponential slope indicating some effective temperature. The tail of these spectra reaches far beyond the normal ponderomotive energy. Evidently, the phenomenon of electron acceleration using this mechanism is significantly different from the simple picture of a free electrons in a plane electromagnetic wave discussed earlier in Section 1.4.3. A detailed discussion of DLA can be found in [64, 65].

Laser wakefield acceleration

Let us now proceed to describe briefly one other major mechanism of laser induced acceleration of electrons in plasma, called laser wakefield acceleration (LWFA). This acceleration mechanism is different from DLA in a sense that it uses the laser-driven high amplitude plasma waves and their longitudinal electric field to accelerate particles. The DLA process, which produces electrons of a quasi-thermal spectra, is not sufficient for practical applications of high energy physics as they require much better quality of electron beams. Such a kind of beam might be generated using LWFA [8, 66].

When a laser pulse propagates through a underdense plasma, it excites a running plasma wave oscillating at the plasma frequency ω_p . The wave drops back the laser pulse with a phase velocity defined by the laser pulse group velocity

$$v_{ph}^{\text{wake}} = v_g = c \left(1 - \frac{\omega_p^2}{\omega_0^2} \right), \quad (1.44)$$

where, ω_0 is the laser frequency. The electric field of this plasma wave is truly longitudinal, pointing in the laser propagation direction. A relativistic electron can be accelerated to high energies, if it can ride on the plasma wave staying in-phase with the longitudinal electric field.

Excitation of the plasma wave by the laser pulse can occur in different ways. The excitation is most effective, when the laser pulse is shorter than the plasma wavelength, $\lambda_p = 2\pi/\omega_p$, and fits completely into the first wave bucket. This wake field excitation pattern differs significantly for laser pulses longer than plasma period due to self-modulation of the of the laser pulse and resonance with plasma frequency. This regime of wakefield acceleration is called SM-LWFA [67].

The energy gain by the trapped electrons can be estimated as

$$eW \approx eE_m L_d, \quad (1.45)$$

where, E_m is the maximum electric field, L_d is the dephasing length (the length over which the electrons experience the accelerating field). One can estimate this from the relation

$$\omega_p \left(\frac{L_d}{v_p} - t_d \right) \sim \pi \quad (1.46)$$

where, $t_d = L_d/c$.

Bubble regime of electron acceleration

There has been a breakthrough in the laser-induced electron acceleration physics through the invention of the so-called “bubble regime” [44], in which the 3D geometry of the laser pulse was considered. In this regime, the laser wave takes the shape of a solitary plasma cavity, referred to as the bubble.

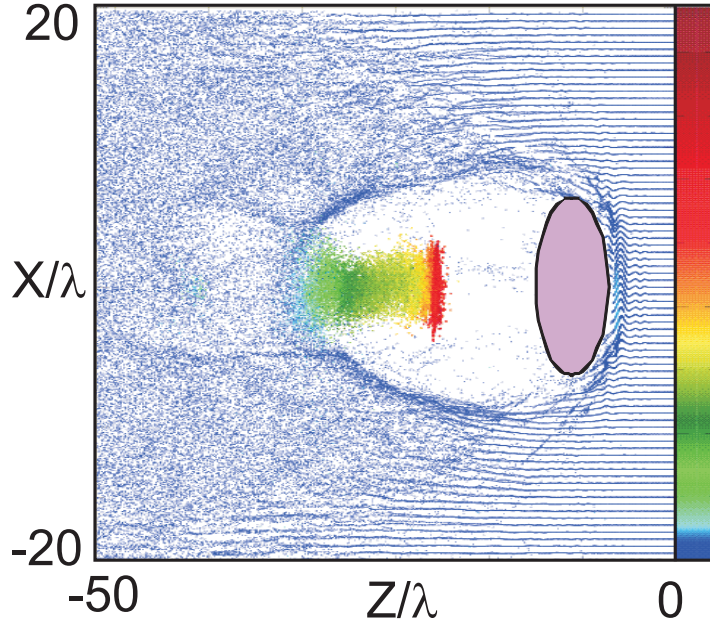


Figure 1.3: Structure of a typical bubble (solitary laser-plasma cavity) produced by 12-J, 33-fs laser pulse (Figure from [44]). The laser pulse (shaded oval) stays in the front of the bubble and the trapped electrons follow this laser pulse.

When the laser pulse is ultra-relativistic and the pulse duration is much shorter than the relativistic plasma period, then the wake field takes the form of a single cavity: the bubble. The bubble is a very efficient device to trap and accelerate electrons. This trapping of electrons is a continuous process and the bubble elongates as the number of trapped electrons increase inside the plasma. The effective bubble velocity decreases and the electrons start to dephase relative to the accelerating field. This causes in self-bunching of the trapped electrons in the phase space. This results in a very significant monoenergetic peak in the energy spectrum of the electrons. Recently, this has also been successfully observed in experiments [68], where the produced electron beam was extremely collimated and quasi-monoenergetic. Some recent studies established that bubbles can be formed at much lower laser power compared to what was initially proposed [38, 40, 69].

Analytical investigation of the theory of bubble is very complicated due to occurrence of system of non-linear kinetic equations and a number of significant parameters. An

1. Introduction

outstanding progress in the development of bubble scaling laws has been performed by Gordienko *et al.* [38], where the similarity theory of the laser-plasma interactions in ultra-relativistic regime was developed. Gordienko *et al.* discussed an optimal configuration for the monoenergetic electron production. The optimal parameters are scaled as: the focal radius $R \approx \sqrt{a_0}/k_p$, where, a_0 is the dimensionless laser amplitude and $k_p = \omega_p/c$.

Using the similarity theory for the regime $c\tau < R$, several scaling laws were obtained. The maximum energy of the monoenergetic peak in the electron spectrum can be calculated as

$$E_{\text{mono}} \approx 0.65 m_e c^2 \sqrt{\frac{P}{P_{\text{rel}}} \frac{c\tau}{\lambda}}, \quad (1.47)$$

where, P is the pulse power and $P_{\text{rel}} = m_e^2 c^5 / e^2 \approx 8.5$ GW. The numerical pre-factors have been obtained directly from 3D Particles-in-cell (3D PIC) simulations.

The similarity parameter, defined as

$$S = \frac{n_e}{a_0 n_c}, \quad (1.48)$$

where, n_e and n_c are the electron and critical densities, respectively, is a very important factor for bubble scaling. The dynamics of the plasmas with $S = \text{const.}$ is similar and electrons move along the same trajectories. The parameter S has the role of relativistically corrected plasma density. It separates relativistically overdense plasmas, $S \gg 1$, from relativistically underdense ones, $S \ll 1$.

1.4.5 Weibel and Two-stream Instability

Discussion about the physics of laser-plasma interaction cannot be completed without talking about instabilities. It is believed that there are thousands of instabilities occurring in plasma physics depending upon the physical conditions and many of them are not yet well understood. In this section we will discuss briefly about Weibel and two-stream instabilities, which are our point of interest for Chapter. 5.

Weibel instability (WI) [49], first predicted by Weibel (1959), is a very frequently encountered plasma instability, occurring in a broad range of physical processes. Fig. 1.4 describes pictorially some of the main possibilities of occurrence of the WI. In case of Fast Ignition [153] scheme of ICF, transportation of relativistic electron beam through a dense ambient plasma is a significant process. Filamentation of the electron beam takes place due to the WI as it propagates towards the precompressed core of the fusion fuel. Secondly, in giant particle accelerators such as, CERN-LHC, SLAC, etc., the accelerated electron beam has to be transported through the large beam lines. These relativistically energized electron beams are also prone to WI during transportation. Moreover, Weibel instability is a very significant phenomenon in astrophysical scenario such as, giant Gamma Ray Bursts (GRB) [74], pulsar, active galactic nuclei [70]. There, this instability is a source of strong cosmic electromagnetic fields. The interesting features for a WI

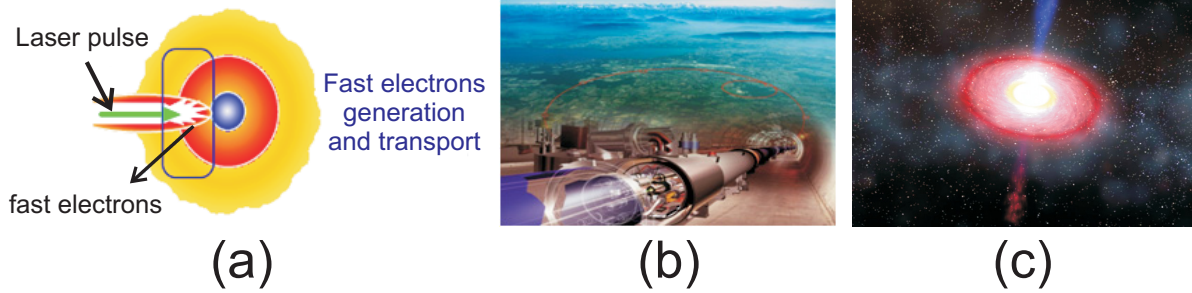


Figure 1.4: Occurrence of Weibel instability. (a) Fusion scenario: transport of relativistic electron beam into the dense background plasma in the FI scheme (Figure from [71]). (b) Accelerator physics: Transportation of accelerated electron beam in large-scale accelerators (Figure source [72]). (c) Astrophysical scenario: generation of strong magnetic fields in the so-called Gamma Ray Burst (GRB), pulsar, active galactic nuclei (Figure from [73]).

are: pinching, filamentation, generation of strong magnetic fields and saturation, etc. However, the analytical modeling of WI is extremely non-linear and complicated.

To give a brief, qualitative description of the Weibel instability mechanism, we consider the Fig. 1.5 [75], where it is illustrated with a simple picture. At first we consider the dynamics of the electrons only and assume that the plasma ions are fixed charge neutralizing background. The electrons are assumed to move along the x -axis with a velocity $v = \pm \hat{x}v_x$ and for net current balance there are equal particle fluxes in opposite direction along the negative x -axis (return electron current). Let us now, add an infinitesimal fluctuation of magnetic field, $\mathbf{B} = \hat{z}B_z \cos(ky)$. The electron trajectories will be deflected as demonstrated by the dashed lines in Fig. 1.5 due to the Lorentz force, $-e(v/c) \times \mathbf{B}$. As a result, the electrons moving to the right will be accumulated in layer I, and, those moving to the left in layer II, and hence, current sheaths form. Thus, the initial magnetic field fluctuation appears to enhance due to this current sheath formation. The growth rate can be written as

$$\Gamma = \omega_p \frac{v_y}{c}, \quad (1.49)$$

where $\omega_p^2 = (4\pi e^2 n/m)$ is the non-relativistic plasma frequency [76]. In a similar consideration, perpendicular electron motions along the y -axis result in the oppositely directed current which, in a way, suppresses the Weibel Instability. Particle velocity along the z -axis is unimportant as they remain unaffected by the magnetic field.

The Lorentz force deflection of the particle trajectories escalates as the amplitude of the magnetic field perturbation gets amplified. This amplified magnetic field is random in the plane perpendicular to the particle motion. After a certain instance the particles will eventually isotropize and the associated thermal energy of the particle motions will be equal to their initial kinetic energy. This will bring the instability to saturation point, in fact, the instability is self saturating. It is to be noted here, that despite its intrinsically kinetic nature, the instability is non-resonant. One needs to mention here,

1. Introduction

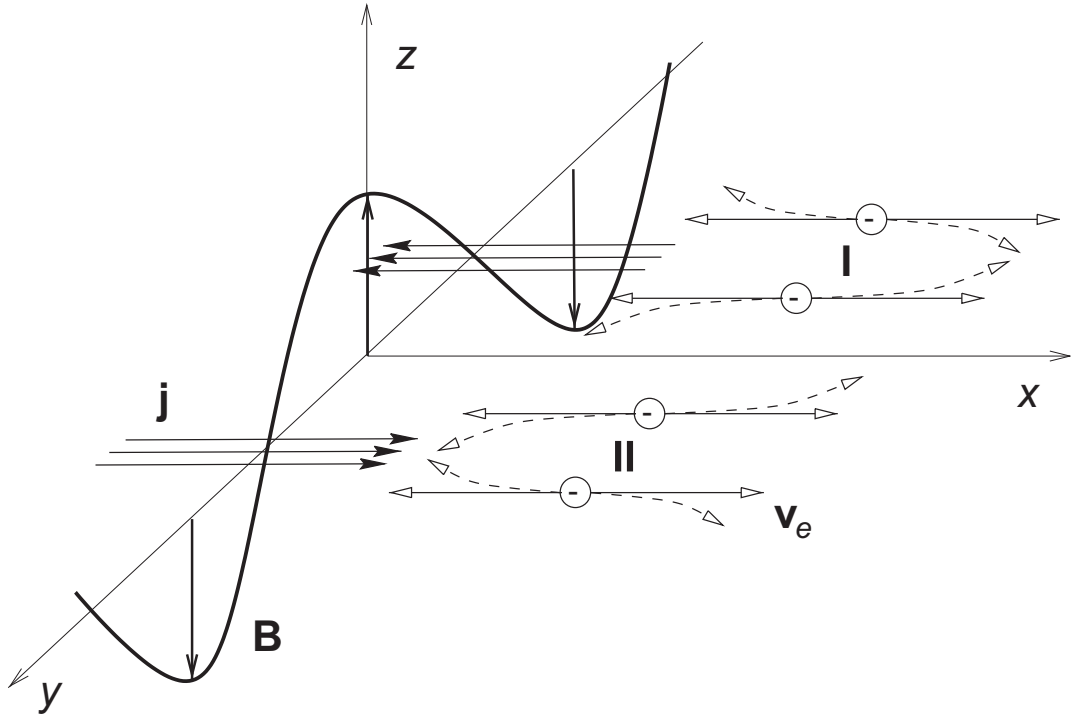


Figure 1.5: Illustration of the Weibel Instability (Figure from [75]). A magnetic field perturbation deflects electron motion along the x-axis and results in current sheets (j) of opposite signs in regions I and II, which in turn amplify the perturbation. The amplified field lies in the plane perpendicular to the original electron motion.

that this instability is temperature sensitive and gets suppressed by a finite temperature spread.

Another kind of instability, a very common in plasma physics, is called the two-stream instability [50–53]. Such kind of instability, similar to Weibel instability, can be triggered by an energetic particle stream injected in a dense plasma. Moreover, different currents for two different species of particles e.g., electron current and ion current, can set off this instability, as well. In this scenario, excitation of the plasma wave can result from the particle energy. The dispersion relation of these plasma waves has a growing wave solution, which is identified as the two-stream instability. If we consider a cold, uniform, and unmagnetized plasma, where ions are stationary and the electrons have velocity \mathbf{v}_0 , that is, the reference frame is moving with the ion stream, then the dispersion relation can be written as

$$\omega_p^2 = \left[\frac{m_e/m_i}{\omega^2} + \frac{1}{(\omega - kv_0)^2} \right] = 1, \quad (1.50)$$

where m_e and m_i are electron and ion masses, respectively, k , wave vector. One can think the two-stream stream instability as the inverse of Landau damping. The roots of Eq. (1.50) can be written as

1.4. Basic Laser-Plasma Interaction Physics

$$\omega_j = \alpha_j^R + i\gamma_j, \quad (1.51)$$

where, α and γ are $\text{Re}(\omega)$ and $\text{Im}(\omega)$, respectively. If the imaginary part $\text{Im}(\omega_j) = 0$, then the solutions represent all the possible modes with no temporal wave growth or damping. The time dependence then is given by

$$\mathbf{E} = \epsilon \exp[i(kx - \omega_j t)] \hat{\mathbf{x}} \quad (1.52)$$

Positive $\text{Im}(\omega_j)$ indicates an exponentially growing wave; negative $\text{Im}(\omega_j)$ indicates a damped wave. Now, if $\text{Im}(\omega_j) \neq 0$, i.e., the solution contains one or more complex roots, then they will occur in conjugate pairs. One of these roots will always be unstable unless all the roots are real. The damped roots are not self-excited and not of our interest for this case.

2 Acceleration of Electrons Using Ionization

2.1 Introduction

Optical field ionization of atoms or ions in a high intensity optical field has long attracted attention in the laser-plasma interaction physics [15–20, 56]. Recently, there have been several theoretical [17–19, 120], numerical [13, 20, 22, 121–123] and experimental [94, 124–126] works performed to understand the ionization physics and to exploit it for different schemes e.g. electron / ion acceleration [11, 12, 68, 84–89]. For all different kind of optical field ionizations (OFI) processes, barrier suppression (BSI) or tunneling, one requires an ionization probability which determines the possibility of ionization of the atom or ion for that particular field intensity. Tunneling ionization probability for Hydrogen like atoms considering potential well was initially proposed by Keldysh [56]. This theory was later extended to ionization from excited electronic states by Perelomov *et al.* [15] and modified for complex ions and atoms by Ammosov *et al.* [16]. In our simulations we mostly concentrate on tunneling ionization. This chapter is dedicated to the implementation of ionization module and understanding the effect of deeper shell ionization of high-Z material in the process of electron acceleration by a radially polarized laser pulse.

The chapter is organized as follows. The first section describes the implementation of the tunnel ionization module in the code VLPL. The second section presents the 3D PIC simulation of generation of collimated attosecond GeV electron bunches from ionization of high-Z material. In the third Section 2.4, 3D PIC simulations of the experiment, performed at Texas laser facility, for production of hot electrons from intense laser irradiated polystyrene spheres is presented followed by an overall discussion and outlook on the study of ionizations in laser-plasma interaction.

2.2 Implementation of Tunneling Ionization in VLPL Code

Virtual Laser Plasma Lab (VLPL) [95] is a relativistic fully electromagnetic Particle-in-cell (PIC) code, written using strongly Object Oriented programming and parallelized using Message Passing Interface (MPI). Up to 10^9 particles and 10^8 mesh cells can be used with the single processor performance $0.5 \mu\text{s}/\text{particle}$, linearly scalable on up to several hundreds nodes. VLPL solves the full sets of Maxwell's equation and equation

2. Acceleration of Electrons Using Ionization

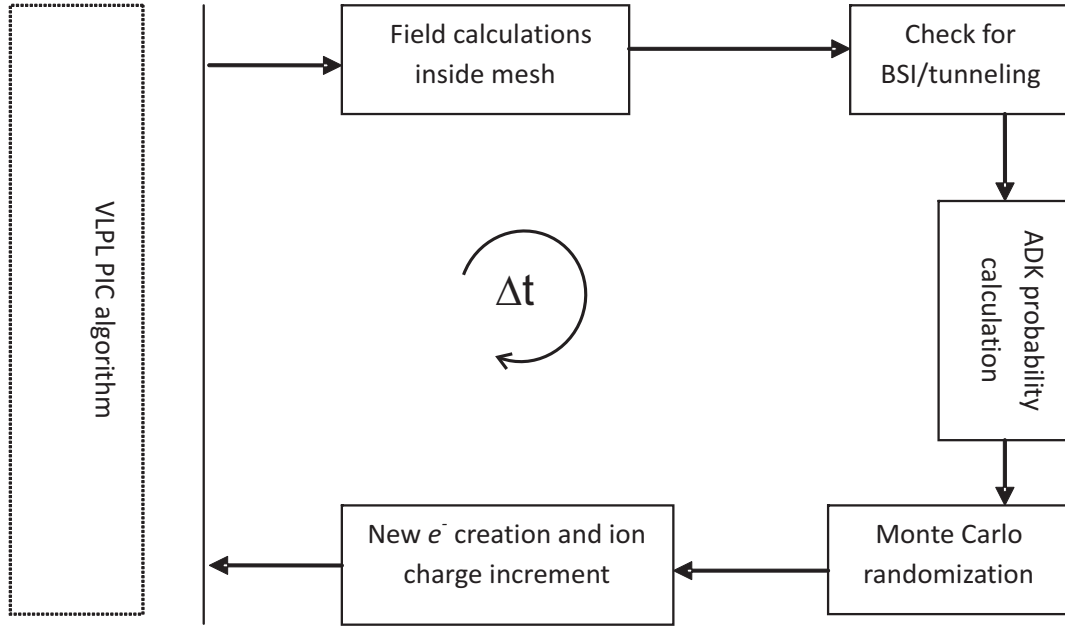


Figure 2.1: An illustration of the ionization methods in one time-step Δt in the 3D PIC code VLPL. Both BSI and Tunneling ionization processes are implemented and the suitable process for the current case is determined by the critical field for ionization E_{crit} .

of motion of the particles. The object oriented configuration allows easy and effective modifications of algorithms.

In VLPL ionization module both Barrier Suppression (BSI) and Tunneling ionization have been implemented. The process taken into account depends on the laser pulse intensity. The key dimensionless parameter that distinguishes between multiphoton and optical field ionization (OFI) is the Keldysh parameter [56]

$$\Gamma = \sqrt{I_p/\varepsilon_{os}}$$

where I_p is the ionization potential and

$$\varepsilon_{os} = \frac{e^2 E^2 (1 + \alpha^2)}{4m\omega^2}$$

is the quiver energy of an electron, α is the polarization parameter and ω , the laser frequency [11]. In this thesis we consider laser intensities well above $\sim 10^{16}$ W/cm², leading to $\Gamma \ll 1$. Thus, we work in the OFI regime, i.e., tunneling and BSI.

The tunneling regime corresponds to low frequency laser fields, $\hbar\omega \ll I_p$, where I_p is the ionization potential. The field must be smaller than the atomic field $E \ll E_a$, where E_a is the atomic field at the corresponding electron orbit. We calculate the ionization probability in the tunneling regime according to the ADK (Ammosov-Delone-Krainov) [16] model.

$$W [s^{-1}] = \omega_A C_{n^*l} f(l, m) I_p \left(\frac{3E}{\pi(2I_p)^{3/2}} \right)^{1/2} \left[\frac{2}{E} (2I_p)^{3/2} \right]^{2n^* - |m| - 1} \times \exp \left(-\frac{2}{3E} (2I_p)^{3/2} \right) \quad (2.1)$$

where $\omega_A = 4.134 \times 10^{16} \text{ sec}^{-1}$ is the atomic unit of frequency, E is the laser field in atomic units. The factors f and C are given by

$$f(l, m) = \frac{(2l + 1)(l + |m|)!}{2^{|m|} (|m|)! (l - |m|)!}$$

and

$$C_{n^*l} = \left(\frac{2e}{n^*} \right)^{n^*} \frac{1}{(2\pi n^*)^{1/2}}.$$

Here n^* is the effective principal quantum number, l and m are magnetic and orbital quantum numbers, and e is the Euler number.

The validity of the ADK theory improves as n^* increases [17]. This occurs for atoms with high atomic numbers and higher charge states, and in our work we focus exactly on these atoms. Further, we introduce the critical electric field [17]

$$E_{crit} = \frac{I_p^2}{4Z},$$

where I_p is the ionization potential and Z is the atomic number corresponding to the threshold laser intensity

$$I_{th}(W/cm^2) = 4 \times 10^9 \frac{I_p^4(eV)}{Z^2}.$$

This critical field distinguishes between the tunneling ionization and BSI. For multiple-electron atoms we implement the sequential ionization only. This means that at every time step, only the bound electron with the lowest ionization potential can be released. For high- Z materials, we use the calculated ionization potentials from Atomic Data Table [128]. Fig. 2.1 shows the numerical scheme of the ionization module in the code. The fields calculated inside the particles motion solver are passed to the method `Mesh:IonizeParticles()`, which ionizes the numerical `IonSpecie` depending on the field strength. In this way a new electron is created and the ion charge is increased. Simultaneously, the new electron gets included into the mesh and continues further.

2. Acceleration of Electrons Using Ionization

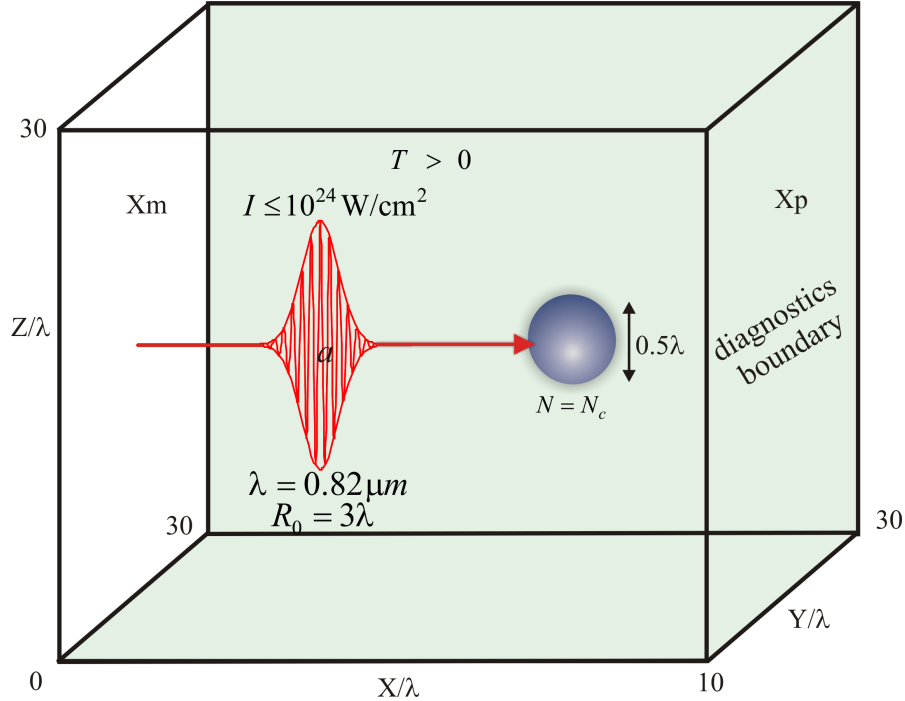


Figure 2.2: Geometrical perspective of the 3D Particle-in-cell simulation. All the lengths are in units of laser wavelength λ . The right hand boundary is the diagnostic boundary for the accelerated electrons. The electrons reaching the diagnostic boundary are captured for post-processing.

2.3 Collimated Attosecond GeV Electron Bunches

In this section, we will describe the three dimensional Particle-in-Cell (3D PIC) simulations of electron acceleration in vacuum with radially polarized ultra-intense laser beams. It is shown that single-cycle laser pulses efficiently accelerate a single attosecond electron bunch to multi-GeV energies. When the laser pulse is longer and consists of several cycles, one has to use ionization of high-Z materials to inject electrons in the accelerating phase at the laser pulse maximum. In this case, a train of highly collimated attosecond electron bunches with quasi-mono-energetic spectra is produced. The radially polarized laser pulse is compared with the usual Gaussian pulse. It is shown that the radially polarized laser pulses are superior both in the maximum energy gain and in the quality of the produced electron beams. The reason is the unique field structure of the radially polarized beams that confines the accelerated electrons and keeps them tightly focused near the optical axis over the full acceleration stage.

Although some semi-analytical studies of electron acceleration with radially polarized electron beams have been published in the last few years [46, 82, 127], here we present the first full electromagnetic 3D PIC simulations. The 3D PIC code VLPL (Virtual Laser Plasma Lab) [95] solves the full set of Maxwell equations. In addition, we have incorporated the Monte-Carlo ionization module that allows us to simulate tunnel ionization of deep electron levels of various high-Z materials.

The most important result of the current study is that one needs electron injection via tunneling ionization into the high-intensity center of the multi-cycle laser pulse to achieve high energy gains. When low- Z materials are used, the target is completely ionized by the very foot of the laser pulse. The electrons are trapped by the low intensity part of the laser pulse and never experience the high-field middle of the pulse. As a consequence, electron energy gains are low. The situation changes when high- Z materials are used. If some deep electron shells of the high- Z material survive the laser field, electrons are injected at the laser pulse maximum and experience high energy gains. We show that the electron energy spectra contain quasi-monoenergetic features corresponding to ionization of different electronic shells of the high- Z material. This work has been published in *Laser and Particle Beams* in 2007 [13].

In the following sections we will present the 3D PIC simulation results of acceleration of electrons to GeV energies by ionization of high- Z material and then a detailed theoretical discussion on the underlying physics of the current acceleration scheme.

2.3.1 Electron acceleration from ionization of high- Z material

To simulate the laser acceleration of electrons in vacuum we use the three-dimensional (3D) Particle-in-Cell (PIC) code VLPL (Virtual Laser Plasma Lab) with the ionization module as explained in the previous section. The simulation box is $(X \times Y \times Z) = (10 \times 30 \times 30)\lambda^3$, where $\lambda = 0.82 \mu\text{m}$ is the assumed laser wavelength. The simulation domain is sampled with a grid of $200 \times 150 \times 150$ cells.

The laser pulse is either linearly polarized Gaussian, or radially polarized. It propagates in the X – direction. The target is located short in front of the laser focal plane, see Fig. 2.2. It is a tiny spherical droplet of radius 200 nm and atomic density $n = n_c$, where $n_c = m\omega^2/4\pi e$ is the critical density. As the laser pulse reaches the droplet, electrons are trapped and accelerated forward. At this time, the moving window technique is applied and the simulation box follows the relativistic electron bunches. In the simulation, we use 28 atoms or ions per cell. Each atom with Z bound electrons can emit all these during the tunneling or barrier suppression ionization. A single run took around two hours on 32 Intel-Xeon processors.

We were looking for materials with large enough ionization potentials to survive laser fields as high as 10^{24} W/cm^2 (ELI Laser Project). Our choices were Xe and Cu, because the I_p for Xe^{52+} is 39.25 keV and for Cu^{28+} 11.17 keV [128]. We compare these two materials with hydrogen, where $I_p = 13.6 \text{ eV}$. Hydrogen is, of course, ionized completely by the very foot of the laser pulse. Earlier, electron injection into high-intensity Gaussian laser pulses via ionization has been discussed elsewhere [129, 130]. Here, we show the difference between the simple Gaussian laser pulses and the radially polarized pulses.

2.3.2 Radially polarized laser pulse

Here we present the simulation results of a radially polarized laser pulse. At the focal plane, the transverse (radial) component of the laser pulse is

2. Acceleration of Electrons Using Ionization

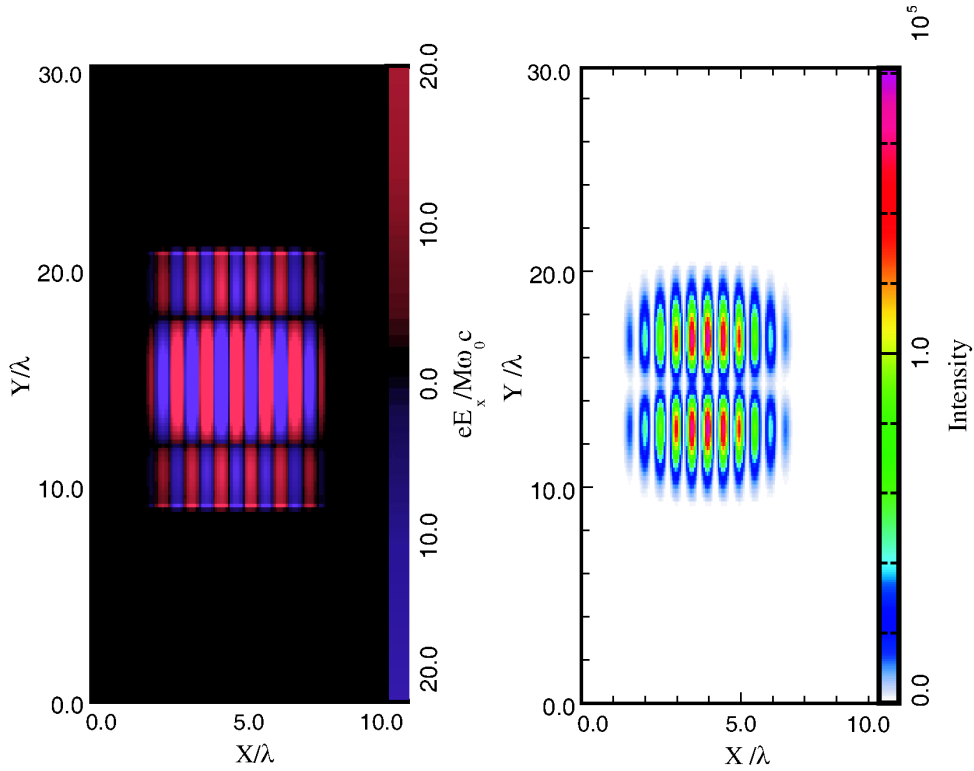


Figure 2.3: $X - Y$ cut of longitudinal field (E_x) (a) and intensity distribution (b) for the radially polarized laser pulse. Axes are in units of λ .

$$E_r = E_0 \frac{r}{\sigma_0} \exp(-r^2/\sigma_0^2) \exp(-t^2/T^2) \cos(\omega t), \quad (2.2)$$

where σ_0 is the focal spot waist and T is the pulse duration. The corresponding longitudinal X -component of the laser field at the focal plane is

$$E_x \approx E_0 \frac{1}{k\sigma_0} \left(1 - \frac{r^2}{\sigma_0^2}\right) \exp(-r^2/\sigma_0^2) \exp(-t^2/\tau_0^2) \sin(\omega t), \quad (2.3)$$

where $k = \omega/c$ is the laser pulse wave number in vacuum. The expression (2.3) gives the first order approximation to the longitudinal laser electric field. The VLPL numerical scheme [95] has the second order accuracy and propagates the fields according to the Maxwell's equations. Fig. 2.3 shows a $X - Y$ cut of the E-field and pulse intensity along the propagation direction inside the simulation box.

One immediately sees from the expression (2.3) that the longitudinal electric field of the radially polarized laser pulse reaches its maximum on-axis. The phase of the longitudinal field is shifted by $\pi/2$ with respect to the transverse component (2.2). This means that a phase range exists, one per laser wavelength, where the longitudinal field is accelerating and the transverse field is focusing.

2.3. Collimated Attosecond GeV Electron Bunches

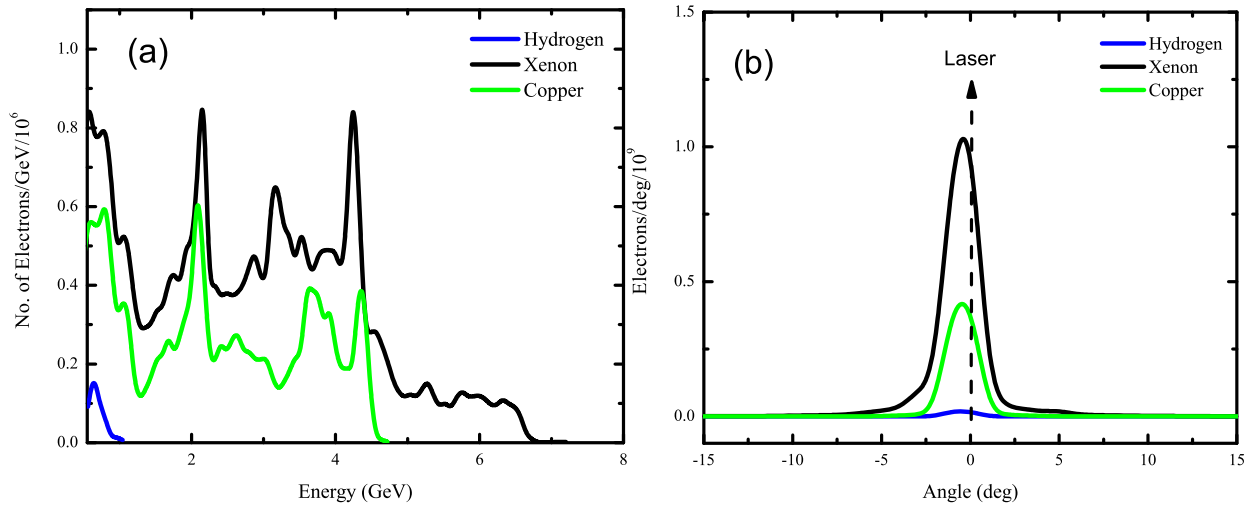


Figure 2.4: (a) Electron energy spectrum (b) angular distribution of accelerated electrons for xenon, copper and hydrogen produced by the 100 PW, 10 fs radially polarized laser pulse with the focused field amplitude $eE_0/mc\omega = 1000$ and $\sigma_0 = 3\lambda$.

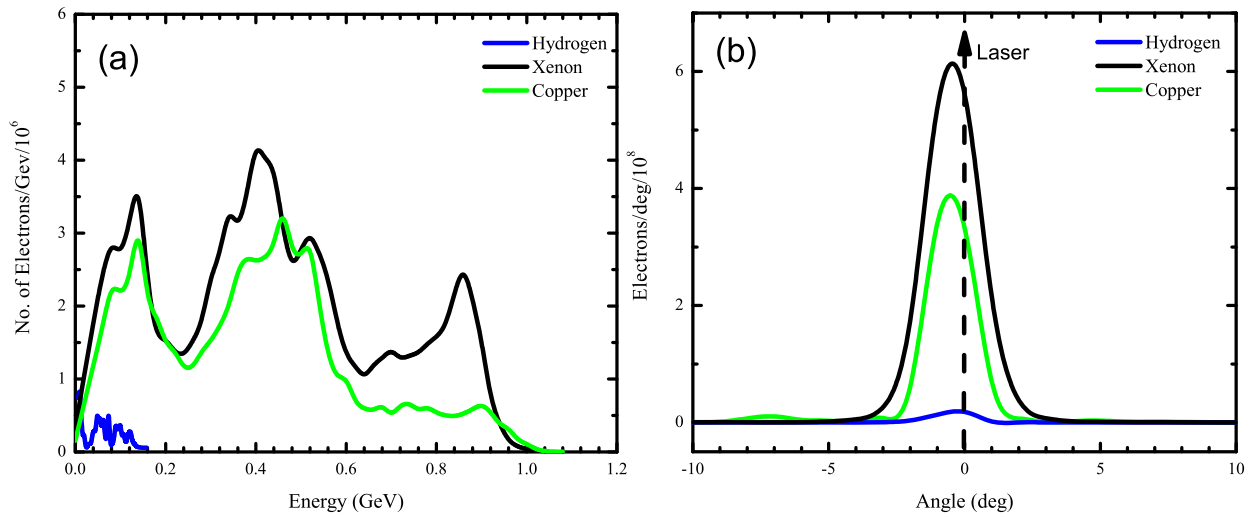


Figure 2.5: (a) Electron energy spectrum and (b) angular distribution of accelerated electrons for xenon, copper and hydrogen produced by the 2 PW, 10 fs radially polarized laser pulse with the focused field amplitude $eE_0/mc\omega = 150$ and $\sigma_0 = 3\lambda$.

2. Acceleration of Electrons Using Ionization

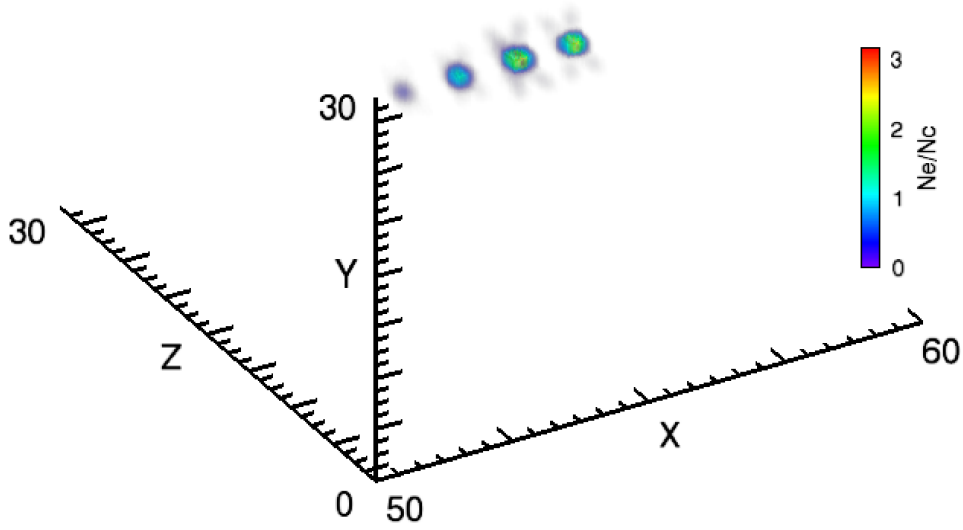


Figure 2.6: Train of attosecond electron bunches produced by the 100 PW, 10 fs radially polarized laser beam for the xenon target after $t = 50$ laser cycles. The axes are in units of wavelength λ .

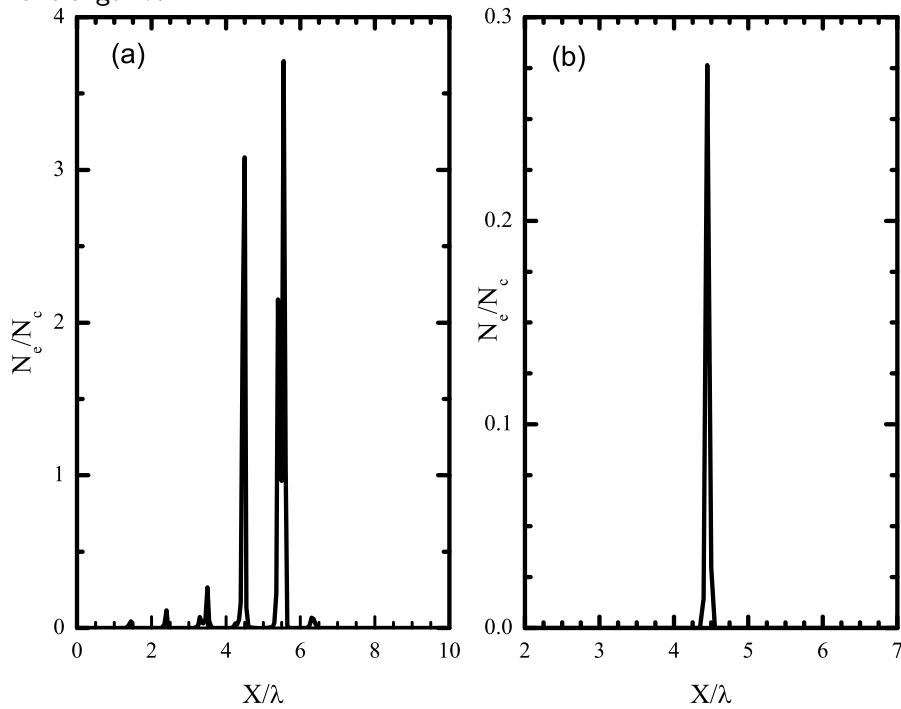


Figure 2.7: 1d-cut of attosecond electron bunches. (a) 100 PW, 10 fs laser pulse, $eE_0/mc\omega = 1000$, $\sigma = 3\lambda$ with Xenon target, (b) single-cycle 100 TW laser pulse with $eE_0/mc\omega = 100$, $\sigma = \lambda$ and hydrogen target.

The group velocity of the focused laser pulse is less than c . Thus, electron buckets trapped and accelerated in this phase range may overtake the laser pulse. If the laser pulse contains many cycles, already its relatively low intense foot wipes electrons away. The electrons will never experience the pulse maximum and the energy gain will be moderate. However, injection due to the ionization of deep levels of high- Z materials can provide an electron source at the pulse maximum. Singh *et al.* described this as self injection of electrons [45].

In the first 3D PIC simulation we take the radially polarized laser pulse (2.2)-(2.3) beam with the power of 100 PW (1 PW=10¹⁵ Watt), 10 fs duration and the focal waist $\sigma_0 = 3\lambda$. The corresponding amplitude $eE_0/mc\omega = 1000$. Such (or stronger) laser pulses are expected within the Extreme Light Infrastructure (ELI) project [5]. Electron energy spectrum and angular distribution of the accelerated electrons are shown in Fig. 2.4.

In the case of high Z atoms (xenon or copper), the maximum electron energies reached are significantly higher compared to Hydrogen. The peak at the lowest energy range corresponds to electrons extracted from the outer shells by the very foot of the pulse. The high energy peaks correspond to ionization of the deep electronic shells. For the angular distribution we take electrons from the high energy peaks of the electron spectrum.

The maximum energies of the accelerated electrons reach ~ 7 GeV for xenon and ~ 5 GeV for copper. This difference is because xenon has deeper inner shells than copper with ionization potentials of those levels four times higher. We observe also a quasi-monoenergetic peak around 4.5 GeV containing some $\sim 10^6$ electrons per GeV. Looking at the degrees of ionization of the atoms we observed Xe⁵²⁺ and Cu²⁷⁺ in this simulation.

Fig. 2.6 and 2.7(a) show the properties of the high energy electron bunches as a 1D on-axis cut (a) and as a 3D volume view (b). Both the results confirm that these are very short and highly compressed dense electrons bunches with attosecond shortness. The spikes in Fig. 2.7(a) *i.e.* the bunches in 3D volume view Fig. 2.6, are around 100 attoseconds short.

To check how the acceleration process scales with the laser power, we performed an additional simulation with the laser pulse of $eE_0/mc\omega = 150$, that corresponds to a power of 2 PW. Results are shown in Fig. 2.5. In this case, the electron energies reach GeV level, indicating the electron energy scaling as $E_{\max} \propto P^{1/2}$, where P is the laser power. In this simulation, we observed ionization up to Xe⁴⁴⁺ and Cu²⁷⁺. Again, there is a drastic difference between the hydrogen target and the high- Z materials.

2.3.3 Single-cycle laser pulse

To get more insight on the performance of radially polarized laser pulses for electron acceleration, we did a further similar simulation with the 100 TW laser pulse, amplitude $eE_0/mc\omega = 100$, waist $\sigma_0 = \lambda$, and duration $T = \lambda/c$. The target material was hydrogen, so that the atoms were instantaneously ionized by the pulse foot. Fig. 2.8 shows the electrons energy spectrum and angular distribution of the accelerated electrons for this case. One observes an excellent monoenergetic peak at 0.9 GeV. Electrons in this peak are collimated within a few degree opening angle. The 3D volume view, Fig. 2.9, shows the single attosecond electron bunch.

2. Acceleration of Electrons Using Ionization

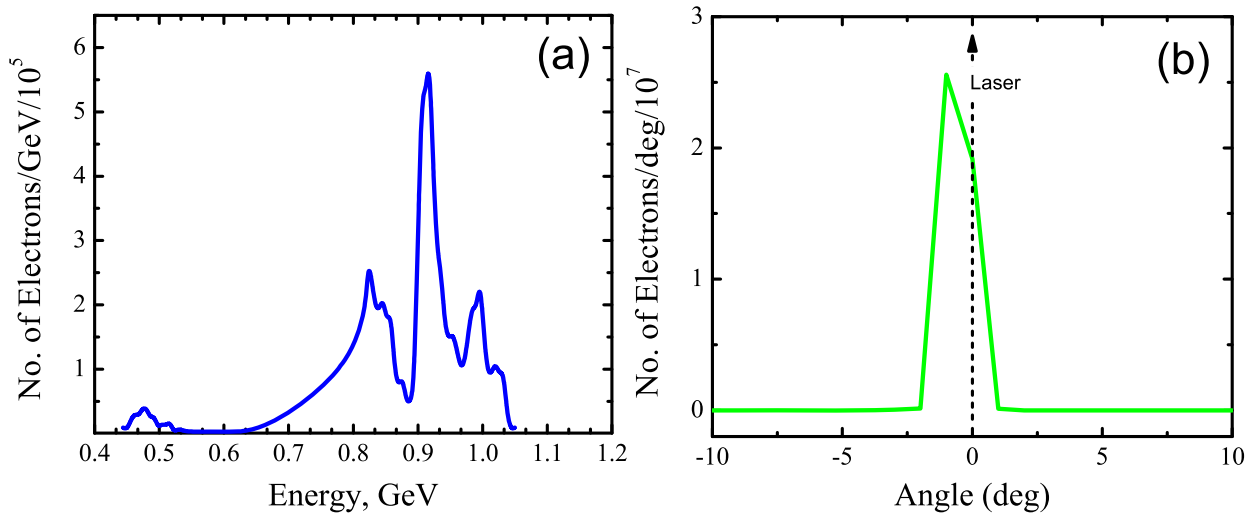


Figure 2.8: (a) Electron energy spectrum and (b) angular distribution for the single cycle 100 TW laser pulse focused down to the amplitude $eE_0/mc\omega = 100$

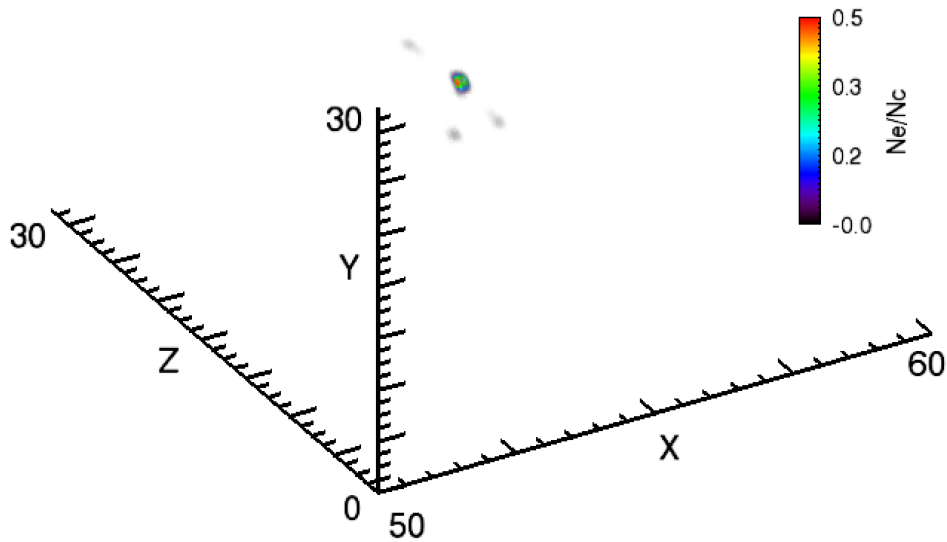


Figure 2.9: 3D volume view of the single attosecond quasi-monoenergetic electron bunch produced by the single cycle radially polarized laser pulse after $t = 50$ laser cycles. The axes lengths are measured in the laser wavelength λ

The electron bunch length in the 1D on axis cut, Fig. 2.7(b), is below 100 attoseconds and is limited by the numerical spatial resolution of this simulation.

2.3.4 Acceleration by the Gaussian beam

In this section we present simulation results for electron acceleration with the linearly polarized Gaussian laser pulse. The transverse electric field of the laser pulse at the focal plane is

$$E_y = E_0 \exp(-r^2/\sigma_0^2) \exp(-t^2/T^2) \cos(\omega t), \quad (2.4)$$

where E_0 , σ_0 , $r = \sqrt{y^2 + z^2}$ and T have the same meaning as that of the radially polarized beam (2.2)-(2.3). The longitudinal component of the Gaussian beam at the focal plane is

$$E_x = -E_0 \frac{2y}{k\sigma_0} \exp(-r^2/\sigma_0^2) \exp(-t^2/T^2) \sin(\omega t). \quad (2.5)$$

Evidently, the longitudinal electric field component of the Gaussian pulse is zero on-axis and reaches its maximum at the pulse periphery.

We perform two simulations with the Gaussian laser pulses. The powers of the Gaussian pulses correspond to those of the radially polarized ones, 100 PW and 2 PW.

The simulation results for these two case are presented in Fig. 2.10 and 2.11. Evidently, electron acceleration with the Gaussian laser pulses is much less efficient and the accelerated electrons have large angular spread. Apparently, the effect of inner shell electron ionization does not improve much the acceleration, as the maximum energy reached by electrons of Xenon or Copper ions are not notably larger compared to that of hydrogen.

2.3.5 Theoretical explanation

In the previous sections we have shown that radially polarized laser pulses are suitable for acceleration of attosecond electron bunches to very high energies. The energy gain of electrons is given by the path integral

$$\int \mathbf{E} \cdot d\mathbf{r} \quad (2.6)$$

along the trajectory. We have seen that it is the longitudinal component of the radially polarized laser pulse (2.3) that accelerates the electrons. This component is of the order of

$$E_x \propto \frac{E_r}{(k\sigma_0)}$$

and decays together with the laser pulse on the distance of the order of the Rayleigh length $Z_R = \pi\sigma_0^2/\lambda$. Thus, the estimate for the energy gain is

2. Acceleration of Electrons Using Ionization

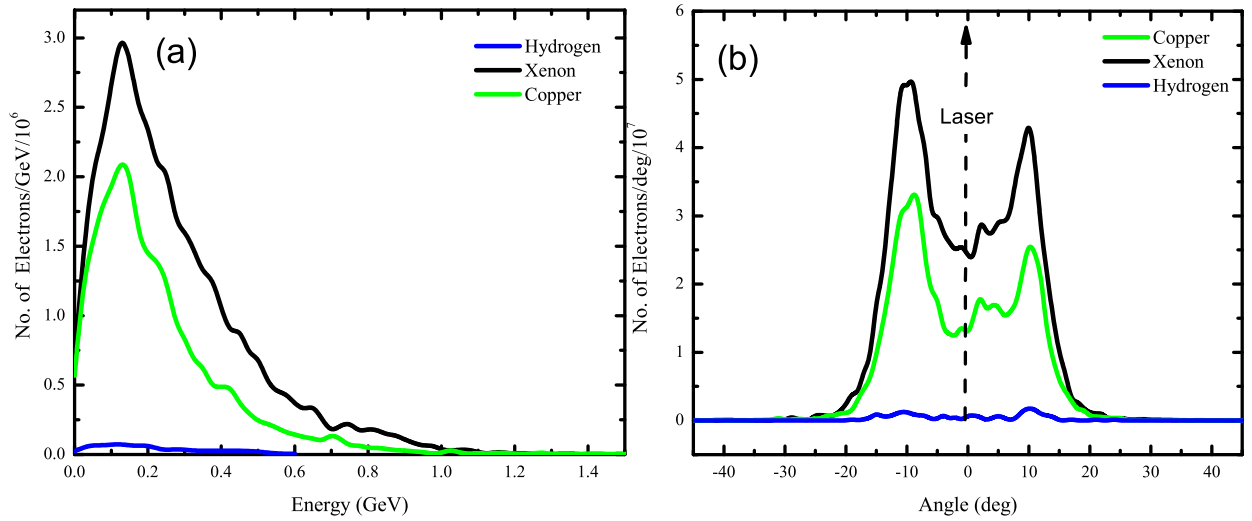


Figure 2.10: (a) Electron energy spectrum and (b) angular distribution for xenon, copper and hydrogen targets for 100 PW, 10 fs Gaussian laser pulse with $\sigma_0 = 3\lambda$. Compare with the radially polarized pulse case, Fig. 2.4

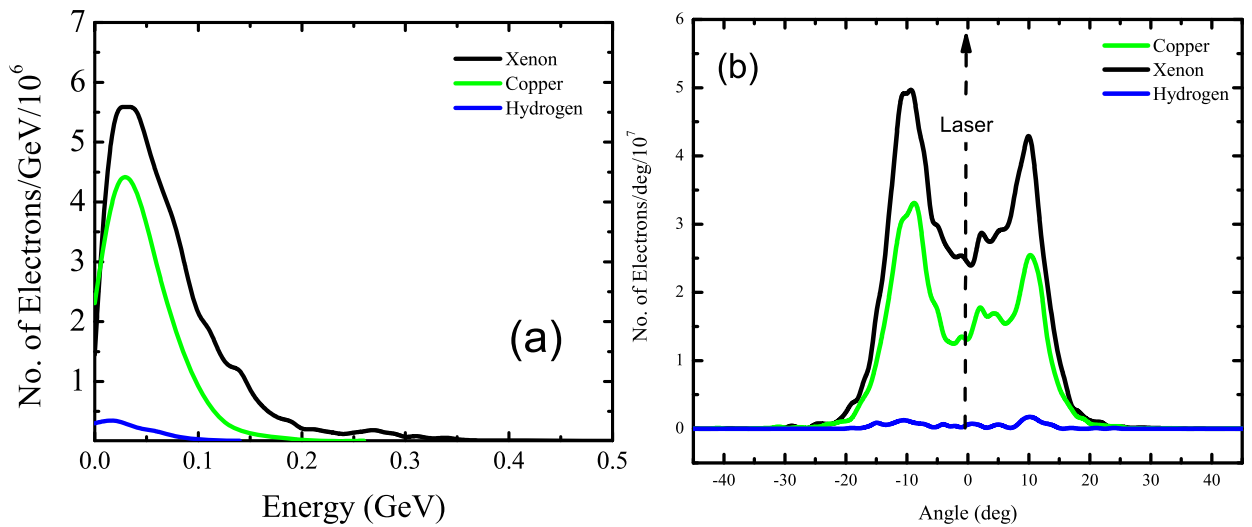


Figure 2.11: (a) Electron energy spectrum and (b) angular distribution for xenon, copper and hydrogen targets for 2 PW, 10 fs Gaussian laser pulse with $\sigma_0 = 3\lambda$. Compare with the radially polarized pulse case, Fig. 2.5

$$\Delta W \propto E_x \cdot Z_R \propto E_R \sigma_0 \propto \sqrt{P}, \quad (2.7)$$

where P is the laser pulse power. This estimate agrees well with the simulation results.

2.4 Hot Electron Production from Laser Irradiated Polystyrene Spheres

2.4.1 Simulation of the Texas laser droplet interaction experiment

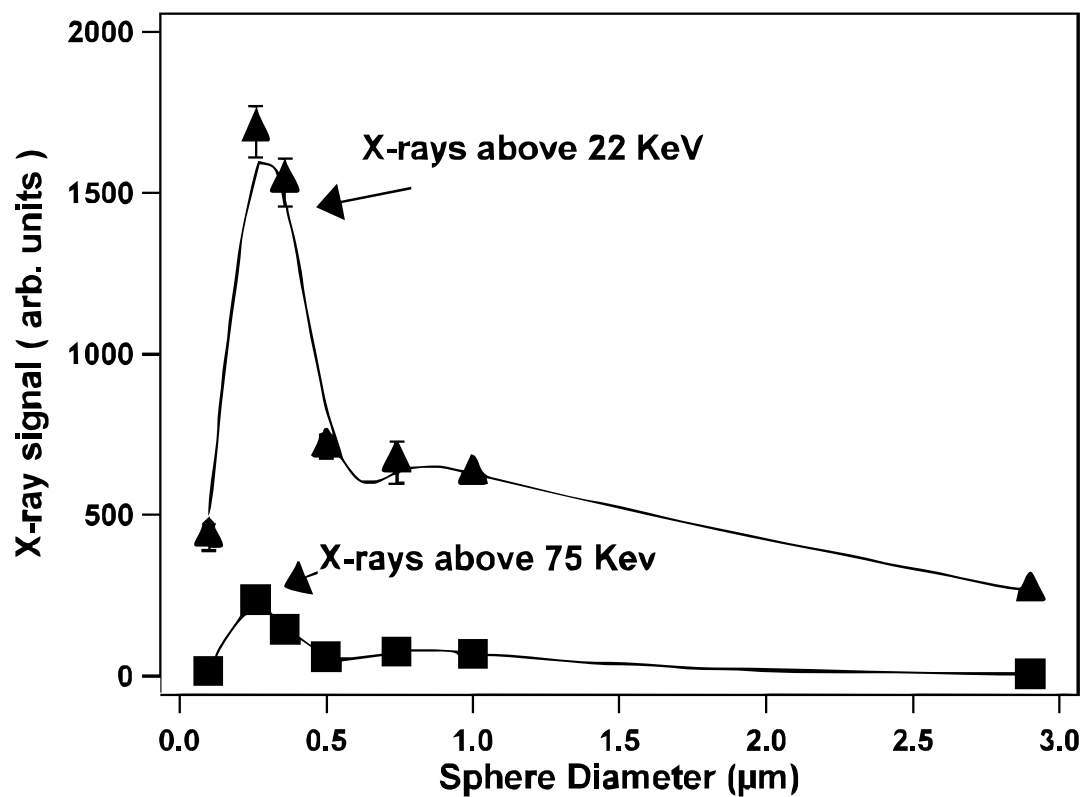


Figure 2.12: Measured x-ray signal as a function of sphere diameter for two different cutoff filters [41]. A significant peak in the x-ray signal is noticeable near the spheres diameter of $0.26 \mu\text{m}$.

This experiment was performed with the THOR laser at the University of Texas at Austin, a high intensity Ti:sapphire laser operating at a central wavelength of 800 nm and capable of delivering 0.7 J on target. In this particular experiment the effects of laser interaction with spheres with a well defined size and of dimensions comparable to the wavelength were attempted to study [41]. Solving for a plane electromagnetic wave impinging on a plasma sphere (Mie resonance) indicates that there should be an

2. Acceleration of Electrons Using Ionization

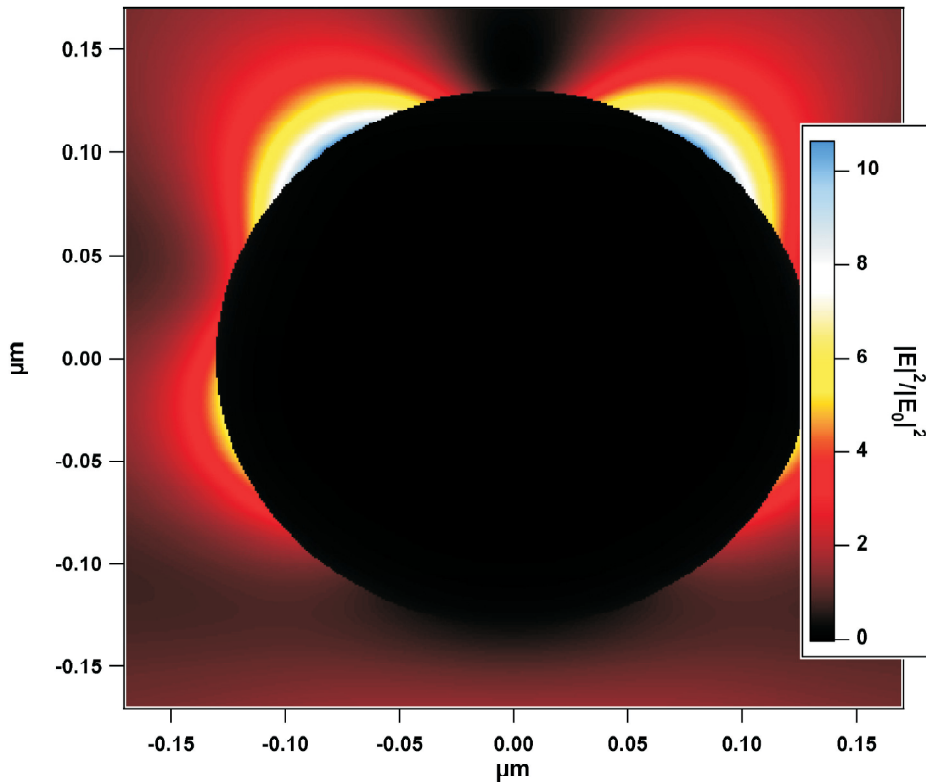


Figure 2.13: An experimental observation showing the enhancement of square of the laser field around a $0.26 \mu\text{m}$ sphere. The color map is in units of laser field incident from the top of the image [41]. Field enhancements are noticeable once again.

enhancement of the local field around the sphere in some parts. This motivated the experiment, to see if this indeed occurs, then one could expect more energetic electrons to be created via vacuum heating.

The target consisted of a glass slide with a covering of a mono-layer of identically sized spheres. Sphere diameters of 100, 170, 260, 360, 540, 740, 1000 and 2900 nm polystyrene spheres have been irradiated. The laser pulse was frequency doubled laser of 400 nm. The spheres were made of polystyrene whose density is 1.05 g/cm^3 and a chemical composition of C_8H_8 . The maximum intensity achieved was $2 \times 10^{17} \text{ Wcm}^{-2}$ with pulse duration of roughly 100 fs. The laser was incident at normal angle to the target. The experimental diagnostics were measuring the x-ray yield with six NaI detectors with various filters. The experimental x-ray yields are plotted in Fig. 2.12. The experimental observations show a peak in the production of total x-rays for the spheres of size 260 nm. The x-ray signal corresponding to this sphere was of the order of three times the strength compared to the 100 or 2900 nm spheres.

The implied electron temperatures were also enhanced but not significantly. From the experiment a simple enhancement of the electric field for a particular sphere size has been seen but that does not seem to give the the results obtained. The enhancement

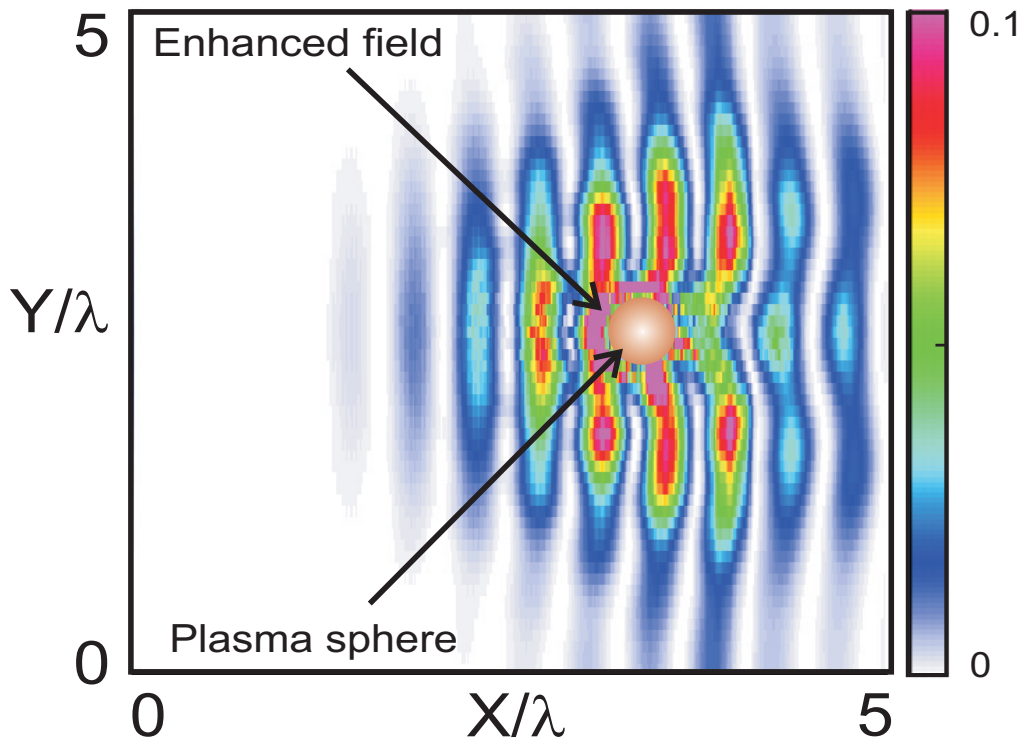


Figure 2.14: A plot of the square of the electric field during an intense pulse interacting with a 250 nm plasma sphere as found from the PIC simulations. The color bar indicates the average of square of the total field $0.5(E^2 + B^2)$.

of the electric fields for the sphere with 0.26 nm diameter is shown in Fig. 2.13. The other idea is that of multiple vacuum heating of the electrons. All these experimental observations strongly motivated us to perform the 3D PIC simulation modeling of the performed experiment with the relativistic parallelized PIC code VLPL [95].

Additionally, another set of experiments with an identical setup was conducted. In this experiment the glass substrate was replaced with silicon and the x-ray k -alpha emission from silicon has been measured. A similar pattern was observed in these x-rays yields. The silicon k -alpha x-ray yield peaked up when using the 260 nm spheres.

To explore the field enhancements around the spheres and x-ray yields, particle-in-cell (PIC) simulations of electron heating were conducted. Together with the simulation results the experimental findings can explain effects of interplay of all of these effects on hot electron production from plasma spheres. In the simulations the laser pulse has been assumed as a 10 fs Gaussian pulse with 400 nm wavelength incident on a plasma sphere with an intensity of $\approx 10^{17} \text{ Wcm}^{-2}$. The plasma spheres are composed of a mixture of carbon and hydrogen ions with an initial electron density $n = 14n_c$, where, n_c is the critical density. Moreover, the effects of ionization of the Carbon (C) and Hydrogen (H) atoms are also taken into account.

The square of the dimensionless field around the plasma sphere of 260 nm diameter is calculated from the simulation results during the laser interaction. This has been

2. Acceleration of Electrons Using Ionization

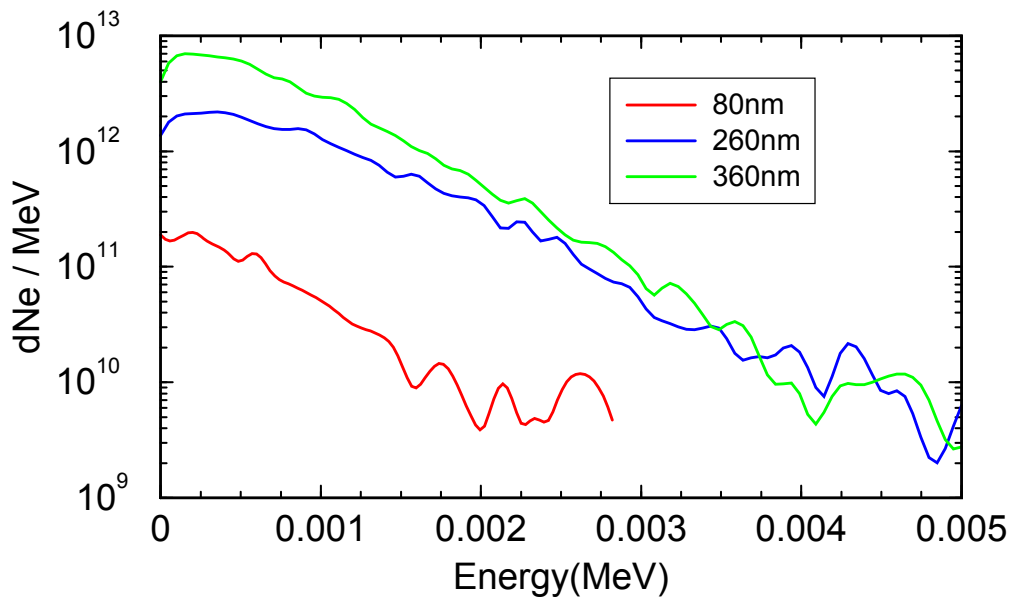


Figure 2.15: Electron energy spectra for the spheres with diameters 80, 260 and 360 nm much after the interaction with the laser pulse.

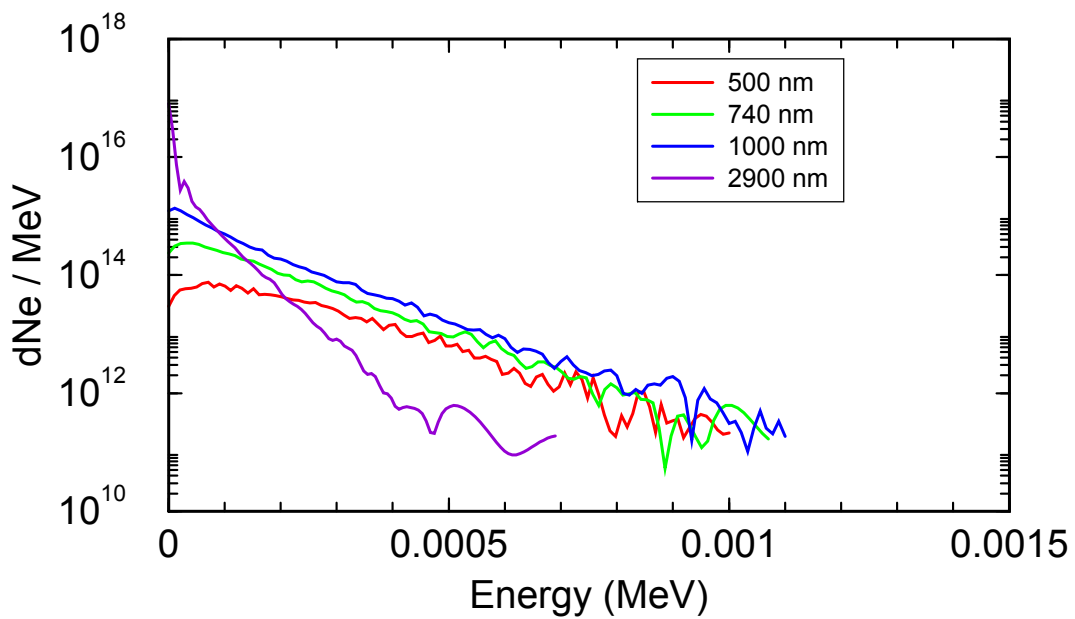


Figure 2.16: Electron energy spectra for the spheres with diameters 540, 740, 1000 and 2900 nm much after the interaction with the laser pulse.

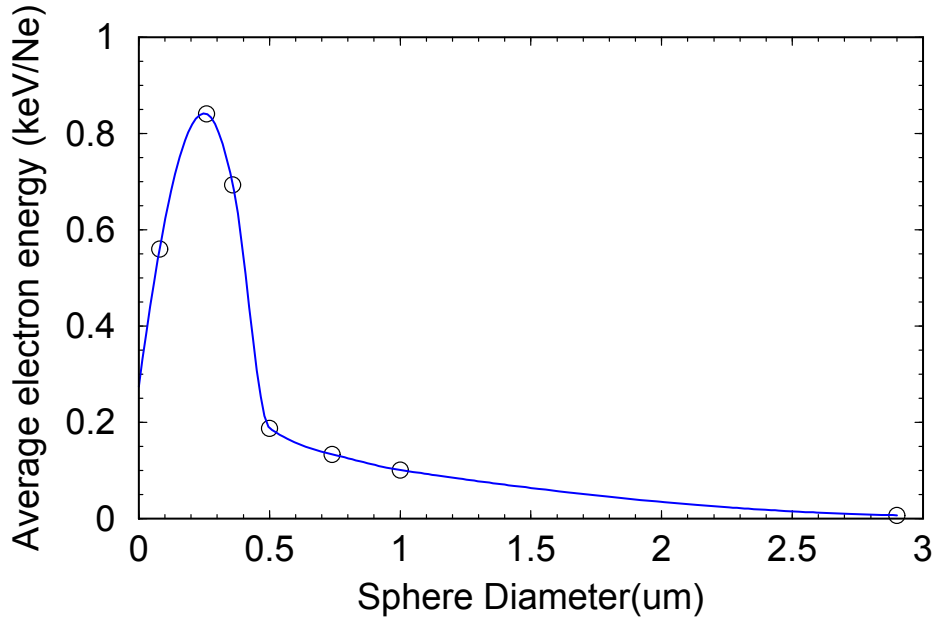


Figure 2.17: A plot of the average hot electron energy in the PIC simulation well after the pulse has passed. The electron energies are normalized with the total number of electrons in that sphere.

illustrated in Fig. 2.14. A well-defined enhancement of the field on the surface of that plasma sphere is evident in this plot. Multiple heating also plays an important role in the final electron temperature. This can be confirmed with the energy spectrum of the electrons inside each type of spheres in Fig. 2.15 and 2.16. The total electron kinetic energy is maximum in case of the 260 nm sphere. Additionally, we noticed a significant resonance for this particular sphere in the simulations.

Fig. 2.17 plots the numerically calculated average electron energy after time $T = 40$, time in laser cycles, into the interaction. This set of simulations show that a maximum in the average energy of the hot electrons occurs for plasma spheres of 250 nm diameter. This represents a remarkable agreement with the trend observed in the experimental data. Hence, at this point, one can conclude from the simulation studies together with the experimental observations, that there exists an optimum sphere diameter for generating hard x-rays from the intense laser irradiated plasma spheres. This is expected to be a consequence of the physics of Mie resonance.

2.5 Conclusion and Outlook

In summary, an ionization module, which includes both BSI and tunneling ionization, has been implemented into our existing relativistic PIC code. Full three dimensional Particle-in-Cell (3D PIC) simulations of acceleration of electrons in vacuum with radially polarized ultra-intense laser beams have been successfully performed. Our simulation results show that single-cycle radially polarized laser pulses, where the longitudinal com-

2. Acceleration of Electrons Using Ionization

ponent of the laser pulse plays the principal role in accelerating the electrons, efficiently accelerate a single extremely collimated quasi-monoenergetic attosecond electron bunch to GeV scale energies. On the other hand, when similar multi-cycle laser pulses are used, one has to properly utilize deeper shell ionization of high-Z materials to inject electrons in the accelerating phase at the laser pulse maximum. In this case, a train of highly collimated attosecond electron bunches with quasi-monoenergetic spectra is produced. A comparison with electron acceleration by Gaussian laser pulses has also been done. It is established that the radially polarized laser pulses are superior both in the maximum energy gain and in the quality of the produced electron beams.

Further, the experimental results of the production of hard x-rays from laser irradiated precisely controlled microscopic spheres were magnificently reproduced with the ionization enabled VLPL code. Moreover, the simulation results were able to explain the enhancements of hard x-rays production for an optimum diameter. These enhancements, from Mie resonance and multiple heating for a sphere of diameter roughly half that of laser wavelength, leads to substantial increase in total number of hot electrons. These enhancements results in the uprise of x-ray yield. This has also been successfully reconfirmed with the numerical simulations.

3 Collisions in Relativistic Laser-Plasma Interactions

3.1 Introduction

In relativistic laser-plasma physics, collisions or rather binary collisions are very frequently encountered inelastic processes. Electron-ion binary collisions play a crucial role in the relativistic beam transportation process of Fast Ignition (FI) scheme of Inertial Confinement Fusion (ICF) [131]. Classical Particle-in-cell (PIC) codes, most widely used to simulate collisionless plasmas, have the possibility to efficiently incorporate collision processes [91, 92]. But implementing collision into the classical PIC scheme has always been a challenge for numerical plasma physicists. Many different approaches both with kinetic and fluid description of plasma e.g. binary PIC-MCC (Particle-in-cell–Monte-Carlo-Collision) model [133–135], Coulomb collision model [136], Langevin approach [132], Gyrokinetic Simulation model [137] and Grid-Based Coloumb Collision model [138], have been adopted to effectively simulate collisional cases of laser-plasma interaction physics. Theoretical models have also been continuously developed to interpret binary collisions more accurately in plasmas under relativistic laser fields [21, 139–141]. In this chapter, we will discuss about the implementation and benchmarking of a collision module incorporated into the relativistic PIC code VLPL [95], followed by the results of a 3D collisional PIC simulations of the electron acceleration experiment performed at Düsseldorf fs-laser system and lastly a conclusion to this chapter.

3.2 Numerical Simulation of Electron-Ion Binary Collisions

It is well understood that collisional impacts in plasma always occur in a distance scale much smaller than the spatial grid size δx of a PIC algorithm, and hence, it has always been difficult to model collision physics in a PIC code [90]. To overcome this complexity, one needs to lower the spatial grid size below the Debye length λ_D , otherwise, there are risks of artificial numerical heating. This in return will increase λ_D , ruining the energy conservative nature of the scheme, until $\lambda_D > \delta x$. However, as the classical closest approach parameter for an electron (b_{\min}), to be deflected through large angle, is of the order of N_D^{-1} , where N_D is the total number of electrons in Debye sphere, even when $\delta x < \lambda_D$, it is troublesome for PIC codes to resolve collision physics properly [145].

Due to such complex nature of collisions, most of the well known PIC codes, initially,

were refrained to include collision algorithms. But there have been several successful developments on implementing collision into the PIC codes. One of the basic approaches are to reduce the collision process restricting to electron-ion binary scattering only, then the collision parameters, such as cross-section, probability, etc. can well be calculated taking into account the electron velocity and ion densities inside the cells of a PIC code. Electrons can then be scattered using a well-know Monte-Carlo randomizing algorithm to give them some altered motion. This approach is a very fruitful, simple and not always wrong. It is important to mention here that, when the fields are computed from direct solutions of Coulomb's law, one can avoid resolving Debye length [142]. Hence, we can summarize at this point, that implementation of collisions in a PIC code is difficult, tricky but not impossible. There have been successful implementations of collision models in some PIC codes and some more complex extensions using Tree Codes [143] and Fokker-Planck modeling [144] have also been performed successfully.

As a matter of fact, this has also motivated us to study the extremely interesting but not trivial electron ion-binary collisions in laser plasma interactions. A Monte-Carlo collision module for the code VLPL has been implemented into the PIC. Afterwards, this implementation, with some test simulations, have been benchmarked successfully. In the following subsection, the implementation of the algorithm 3.2.1 and also a benchmarking simulation 3.3 will be presented in detail.

3.2.1 Implementation of the VLPL3d collision module

At this point it is worthy to remind that, the benefit of a PIC numerical method is that it solves a system of ordinary differential equations for every particle, which involve a long-range electromagnetic force, i.e. Lorentz force. The current collision method includes electron-ion binary collisions in overdense plasma in a precise manner. For the sake of simplicity it is presumed that all simultaneous collisions are avoided although multiple collisions may, of course, occur in this consideration. In a collisional plasma the position coordinates of the numerical '*macroparticles*' satisfy all the characteristics numerical equations of the collisionless case, whereas, the particle momentum equations do not. Hence, the particle motion equations have to be rewritten for the short-range Coulomb collisions in the following way [132]:

$$\frac{d}{dt}\mathbf{p} = e\mathbf{E} + e\left(\frac{\mathbf{v}}{c} \times \mathbf{B}\right) + \mathbf{F}_{\text{coll}} \quad (3.1)$$

where \mathbf{F}_{coll} is the effective collisional force acting on the particles.

At the same time, one has to rethink the way to find the collisional force \mathbf{F}_{coll} . Moreover, it is also a matter of concern that modifying the implicit particle momentum in the main PIC algorithm can be potentially dangerous for the momentum/energy conservation methods therein. A couple of faithful ways to do it are: solving the Fokker-Planck-Landau equation [57] or solving for the well known BGK equation etc. But these may become extremely computationally expensive for cases like, ultrashort relativistic laser produced plasmas, high density or Fast Ignition (FI) plasmas. Hence, two crucial considerations need to be taken into account in choosing the collision algorithm:

3.2. Numerical Simulation of Electron-Ion Binary Collisions

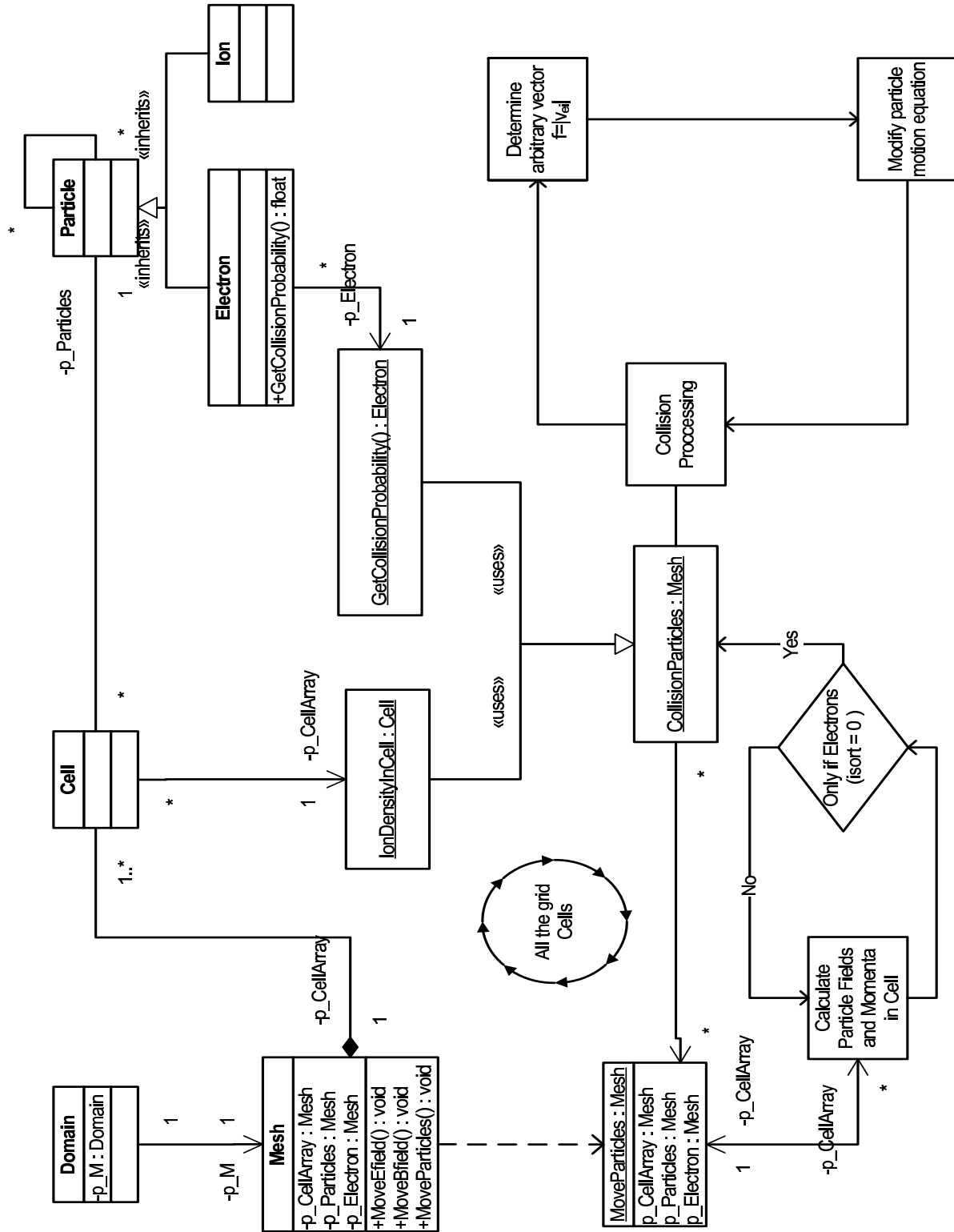


Figure 3.1: Description of the UML Class interface of the VLPL code with the flowchart diagram of the implicit collision algorithm. The method `void Mesh::moveparticles()` executes the motion equation for all the particles inside the Mesh.

3. Collisions in Relativistic Laser-Plasma Interactions

1. The model needs to define efficiently well, the binary collisions preserving the energy conservation methods of the PIC scheme. Therefore, one can avoid the risk of numerical instabilities and unwanted forced conservation methods.
2. The numerical model should be computationally optimal. Hence, one can increase the efficiency as it will not be extremely time consuming for very high density plasmas, like fusion plasma, where the density corresponds to $10^5 n_c$ and one has to choose couple of hundred of particles-per-cell in a PIC simulation.

In Fig. 3.1 the technical descriptions of the VLPL3D collision module has been provided with an interface of the VLPL3D UML class definitions coupled with collision algorithm flowchart diagram. The particle motion equations are modified inside the the method `Mesh::MoveParticles()`. The first important task is to calculate the collision probability of the electrons. Since the ions are 1836 times heavier than the electrons, we only calculate the collision probability ν_{ei} for the numerical electrons inside each cell of the simulation domain in a single time-step T_s . Now, the distance traversed by an electron in a single time-step (T_s) is given by

$$d = \frac{|\mathbf{p}|}{\sqrt{1 + |\mathbf{p}|^2}} T_s. \quad (3.2)$$

Implicit ion densities inside each numerical cell (N_i) has been considered to calculate the mean free-path length of the binary collision as

$$\lambda_{\text{free}} = \frac{1}{N_i \sigma}, \quad (3.3)$$

where σ is the differential scattering cross-section, which can be obtained from a list of experimental values. Thus, the numerical scattering probability ν_{ei} comes out to be

$$\nu_{ei} = \frac{d}{\lambda_{\text{free}}}. \quad (3.4)$$

Now, we generate a unit vector of of arbitrary orientation \mathbf{f} , such that,

$$|\mathbf{f}| = \left| f_x \hat{i} + f_y \hat{j} + f_z \hat{k} \right| = 1. \quad (3.5)$$

This will, at once, allow us to introduce a stochastic change in the particle motion equation. A new vector \mathbf{F} can be constructed right away, such that,

$$|\mathbf{F}| = |\mathbf{f} \cdot \nu_{ei}|, \quad (3.6)$$

3.3. Benchmarking with Physical Processes

where ν_{ei} is the electron-ion collision frequency. Henceforth, we modify the particle motion equation as

$$\frac{d}{dt} \mathbf{p} = e\mathbf{E} + e\frac{\mathbf{v}}{c} \times [\mathbf{B} + \mathbf{f} \cdot \nu_{ei}]. \quad (3.7)$$

We continue to push the same particle into the inherent PIC scheme with the modified motion equation. This implicit method avoids directly modifying the implicit particle momenta \mathbf{p} , hence, keeps off any numerical heating therein. The whole sequence of process loops over all the mesh cells.

This collision module, implemented with the above mentioned scheme, has been benchmarked with a simple and intuitive test collisional simulation. This has been described in the following Section 3.3.

3.3 Benchmarking with Physical Processes

3.3.1 Scattering of hot electron beam in ambient collisional plasma

To benchmark the collision module, we choose to simulate a simple test problem. A narrow, extremely low density cylindrical electron beam which is propagating in the positive X -direction with an initial thermal velocity v_{th} expressed in terms of momentum spread as $p_x \sim 50$ keV as shown in the schematic of Fig. 3.2. The incident electron beam is approximately $2 \mu\text{m}$ wide with a radius of $1 \mu\text{m}$. The beam has a very low electron density, $n_b = 10^{-10}n_0$, where n_0 is the background density, to have a larger free-path λ_{free} . We have chosen different instances of the thickness of the ambient plasma slab to be able to verify the validity of the collision algorithm. The thickness of the overdense ($n = 5n_0$) plasma slab (d) has been altered to five different multiples of λ_{free} . This, in a way, will provide us different multiples of the free-path length. The simulation box dimension is $(X \times Y \times Z) = (5 \times 5 \times 5) \mu\text{m}$. For all the cases the differential collision cross-section is $\sigma = 10^{-16}$ srad/cm². Five different simulations have been performed for thicknesses (a) $d = 0.01\lambda_{\text{free}}$ (b) $d = 0.1\lambda_{\text{free}}$ (c) $d = 1.0\lambda_{\text{free}}$ (d) $d = 3\lambda_{\text{free}}$ (e) $d = 10\lambda_{\text{free}}$ to understand the validity of the collision module. A schematic of the simulation problem has been illustrated in Fig. 3.2.

When the thickness of the plasma slab $d \ll \lambda_{\text{free}}$, free-path of the ambient collisional plasma electrons, i.e., case (a), the beam electrons do not actually get any chance to get scattered by the ambient plasma ions. Hence, relativistic beam electrons can pass through the very thin plasma slab without even facing any noticeable instance of binary collision. This is also the case in a real physical condition. When the slab thickness, on the contrary, has been increased to $d = 0.1\lambda_{\text{free}}$ in case (b), there will be very low possibility of the beam electrons getting scattered due to collisions with the plasma ions. As a consequence, a very small number of beam electrons may get spread out, which is also evident from the Fig. 3.3(b).

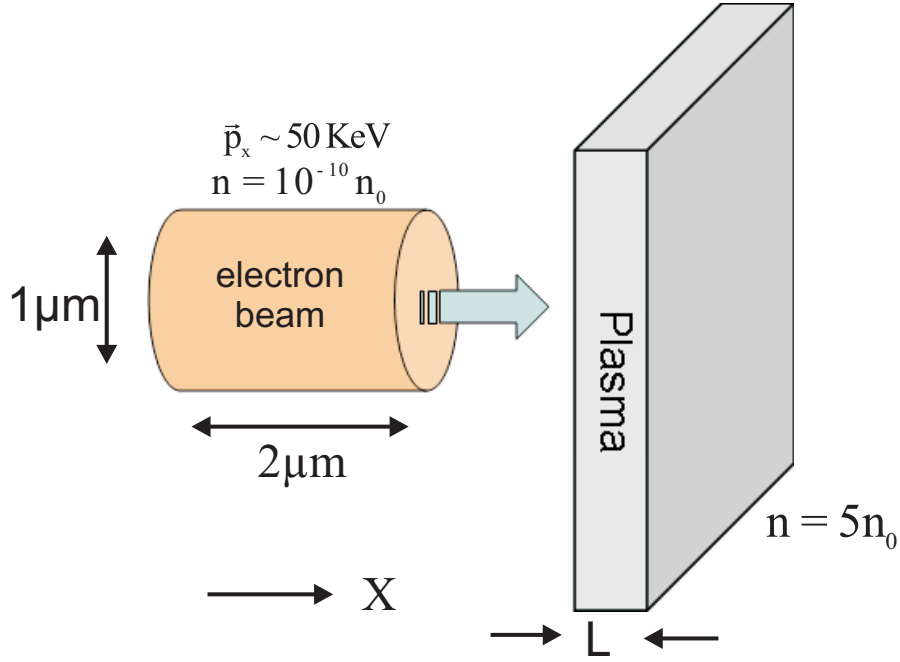


Figure 3.2: 3D schematic of the benchmarking simulation for collision of a hot electron beam electrons with ambient plasma ions for different thicknesses of a plasma slab.

On the other hand, if the interacting plasma slab thickness corresponds to λ_{free} , i.e., in case (c) of Fig. 3.4, the beams electrons encounter a minimum distance, which is enough to collide with ambient ions. That results in a recognizable amount of scattering of the beam electrons but a significant portion of the beam passes non-scattered. This observation, as well, matches considerably enough with the physical understanding.

To benchmark further, the feasibility of the VLPL collision module, we proceed to observe the effects of interaction lengths much larger than λ_{free} . In the following case (d), when the interaction length of the beam-plasma system is $3\lambda_{\text{free}}$, very reasonably, most of the beam electrons at least once get collided with the ambient plasma ions. As a result, the beam electrons virtually become entirely scattered after colliding with the ambient plasma ions. The simulation result, which shows the similar observation, has been depicted in Fig. 3.5(d).

Furthermore, we simulate the case (e), when the interaction length of the beam-plasma system is $10\lambda_{\text{free}}$, all the beam electrons must experience collision here, as they traverse enough length to face multiple collisions. Thus, after passing through the ambient plasma slab the beam gets extremely scattered, because the beam electrons flow some random path after colliding with the plasma ions. At this point, we can summarize that, the collision module of the code VLPL benchmarks well enough the collisional processes in relativistic laser-plasma interactions. The feasibility of the scheme has passed important tests successfully.

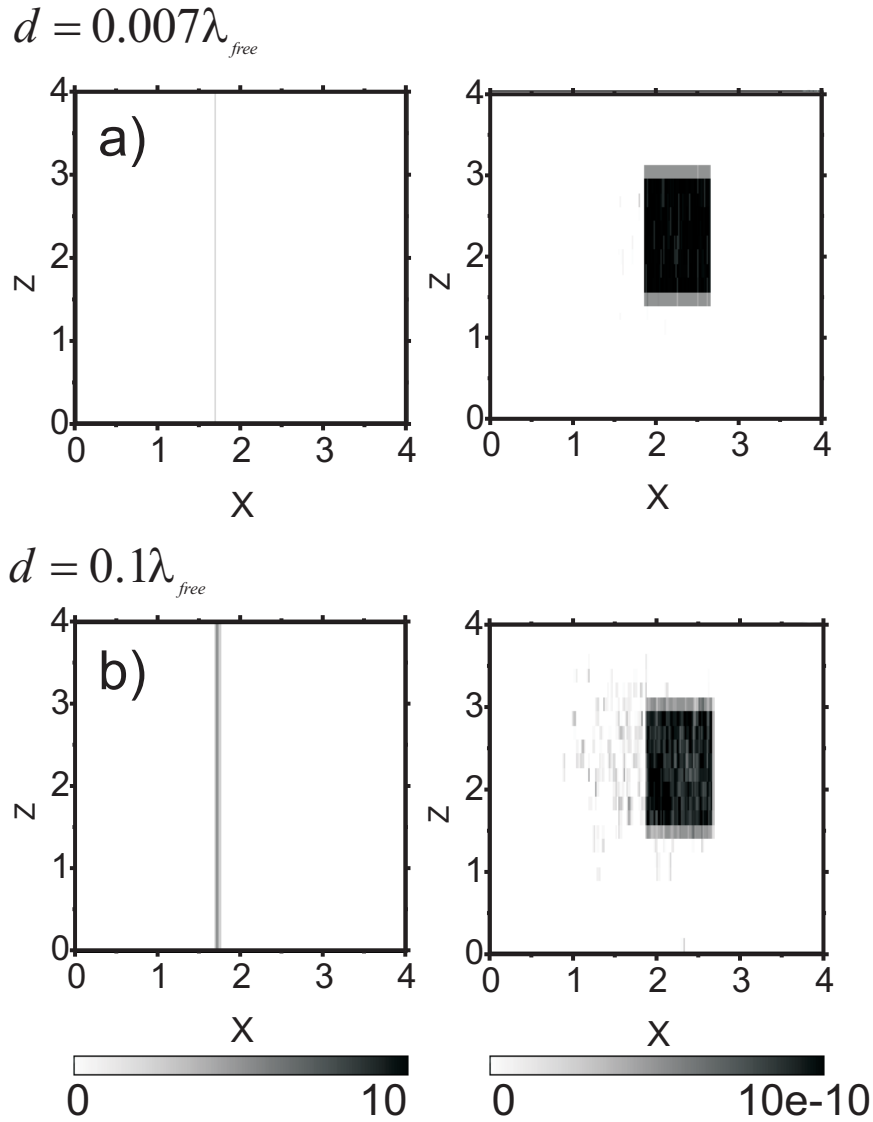


Figure 3.3: Scattering of an electron beam for different thickness of a plasma slab. (a) When the thickness of the slab is $d = 0.007\lambda_{free}$ there are no scattering of electrons. (b) For $d = 0.1\lambda_{free}$ just a little amount of scattering occurs.

3.4 Directed Acceleration of Electrons from Solid Surface

A more extensive use of our VLPL collisional algorithm has been undertaken by reproducing and explaining the results of an experiment done by Brandl *et. al.* [14] at ILPP, HHU, Düsseldorf. In this experiment electrons have been accelerated from solid target surfaces by a sub-10-fs laser pulses of 120 μJ energy which was focused to an intensity of $2 \times 10^{16} \text{ W/cm}^2$. The details of the simulation results and its comparison with the experimental findings have been discussed in 3.4.1.

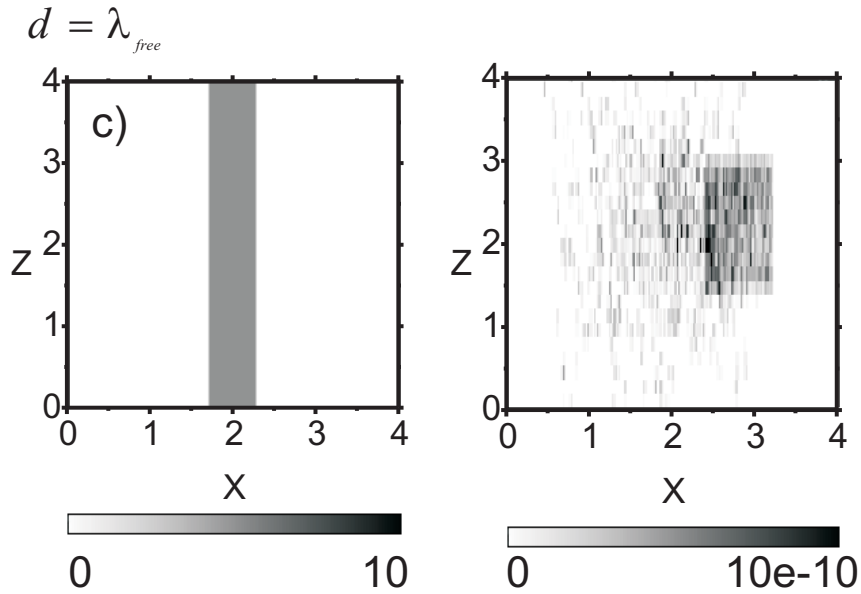


Figure 3.4: When (c) $d = 1.0\lambda_{\text{free}}$ a significant part of the beam passes unscattered whereas, a recognizable amount of beam electrons get scattered by the ions.

There have been many successful attempts where a relativistic ($a_0 > 1$) sub-ps laser pulse has been focused into an underdense gas to produce strongly collimated accelerated electron beams in the specular directions. These works observed quasi-monoenergetic spectra for accelerated electron beams up to the GeV scale [10, 12, 68, 84, 146, 147]. But focusing on a solid target instead of gas, typically produces less energy electrons in a very broad angular dispersion; showing a strong dependence on the physical properties of the expanding plasma produced on the solid target surface [148–150]. A different method has also been undertaken by Osterholz *et al.* [151], where a laser pulse with much lower pulse energies (≤ 1 mJ) but with sub-10-fs duration focused on a solid surface to produce a near solid density plasma and peak electron energy of ~ 100 eV. The current experiment shows that such laser pulses with only $120 \mu\text{J}$ of energy can also be used for directed electron acceleration from the solid target surfaces and that energies well above 100 keV can be obtained. This experiment is dominated by the primary interaction of the electromagnetic fields with free electrons together with collisions inside the solid, whereas the plasma plays no significant role. The simulation results shows a detailed perceptible of the electron energy spectrum and the angular divergence of the hot electron from the target surface. In addition, the excellent agreement with the experimental finding confirms the correctness of the VLPL collision module.

3.4.1 3D–PIC simulation of the experiment

A three-dimensional (3D) simulation of the experiment has been performed using Virtual Laser Plasma Lab (VLPL) [95], a fully relativistic, massively parallelized electromagnetic Particle-in-Cell (PIC) code. A p -polarized laser pulse of wavelength $\lambda = 0.82 \mu\text{m}$ with

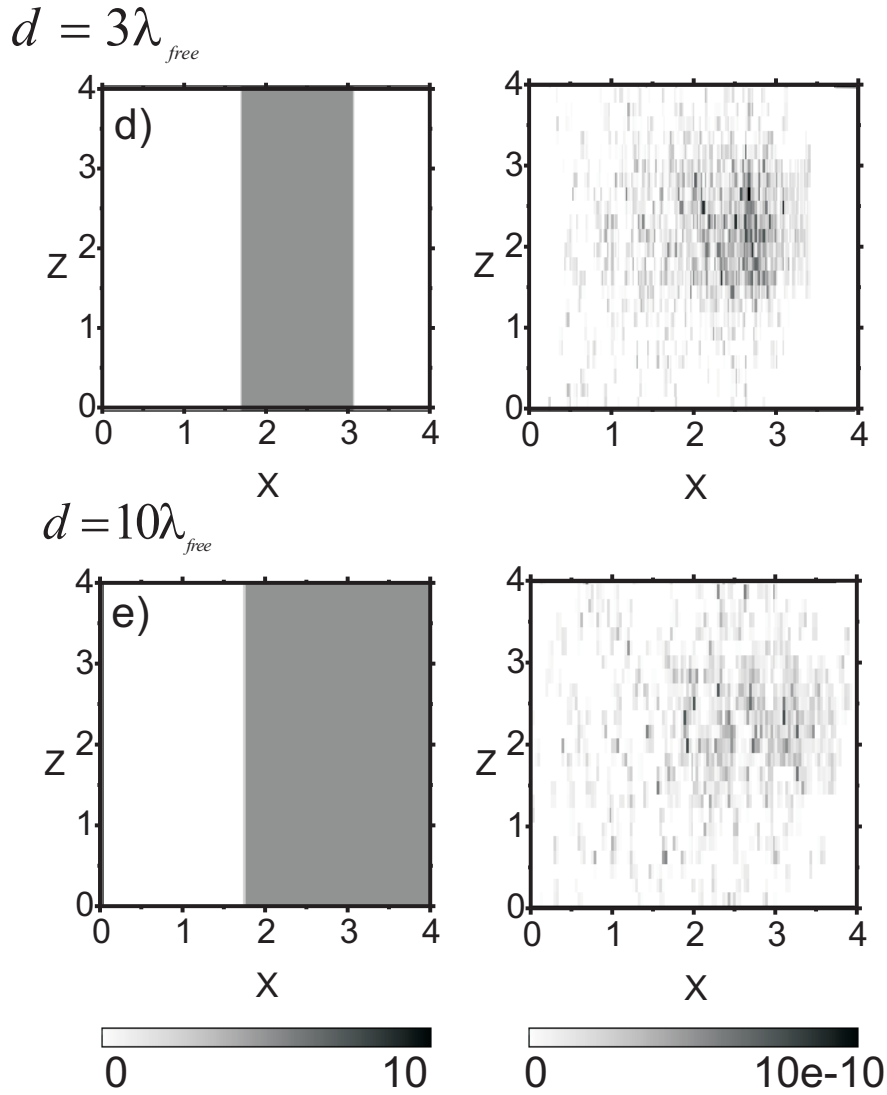


Figure 3.5: Scattering of an electron beam for different thickness of a plasma slab. (d) When the thickness of the slab is $d = 3\lambda_{\text{free}}$ almost all the beam electrons get dispersed by colliding with the plasma ions. (e) for $d = 10\lambda_{\text{free}}$, the scattering rate or probability is much higher and virtually every electron experiences collision.

$a_0 = 0.2$ is obliquely incident on an overdense plasma layer. The angle of incidence is 45° and the laser peak intensity is $I_0 = 5.5 \times 10^{16} \text{ W/cm}^2$. The plasma density rose sharply from 0 to $n = 50n_c$ within $0.1 \mu\text{m}$, here $n_c = m\omega^2/4\pi e^2$ is the critical density. The plasma layer is $1 \mu\text{m}$ thick. The simulation box size is $(X \times Y \times Z) = (3\lambda \times 10\lambda \times 1\lambda) \mu\text{m}^3$. The laser pulse profile was chosen to be Gaussian:

$$a = a_0 \exp(-r^2/R^2) \exp(-t^2/T^2) \cos(\omega t) \quad (3.8)$$

where the spot radius $R = 1.64 \mu\text{m}$, and $r^2 = x^2 + y^2$, the time duration was $T = 9 \text{ fs}$.

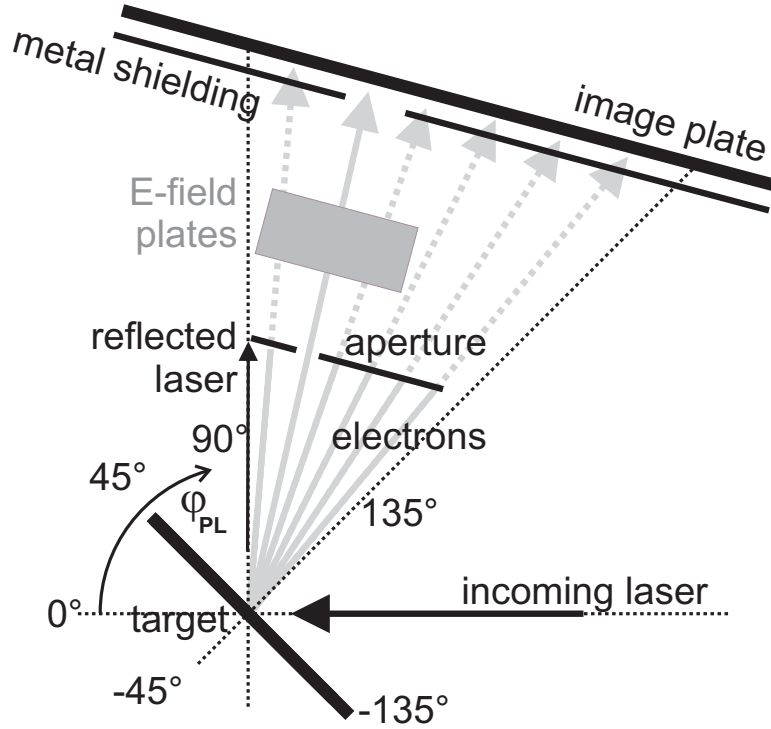


Figure 3.6: Experimental setup for spectral measurements. Used without aperture, E-field and shielding for 2D survey images. (Figure: Brandl et al. [14])

The entire simulation box is sampled with a mesh grid of $120 \times 100 \times 2$ cells. To resolve the angular distribution of electrons accurately, we used an extensively large number of electrons (as much as 1000 particles per cell for electrons). The boundary conditions for the fields and particles were periodic in the lateral directions.

The code VLPL has been equipped with electron-ion binary collisions. The velocity dependent differential scattering cross-section σ for electrons have been taken from [152] to obtain the scattering probability in each time-step inside the cells. In the present simulation σ corresponds to Aluminum plasma. The laser pulse train has been allowed to interact 15 laser cycles period and the electrons leaving the front surface of the target have been saved for diagnostics.

Fig. 3.6 shows the experimental setup for the spectral measurement. In this experiment, a p -polarized pulse hits the target under 45° incidence. Flat surface targets of different metals (Al, Ag, and Au) were used as targets for this experiment. Two different diagnostics has been performed: firstly, the angular electron distribution was recorded in the angular cone of (90° - 135°) and secondly, the energy spectra of the hot electrons leaving the target front surface in the same angular cone.

The first experimental result was that the hot electrons emitted from the interaction region of the target fly to distinct angular directions, as shown in Fig. 3.7. One or several confined spots on the image plate have been formed by these energetic electrons, typically around the horizontal laser plane and at angles between 100° and 130°. This particular pattern was reproducible from shot to shot and similar for all investigated

3.4. Directed Acceleration of Electrons from Solid Surface

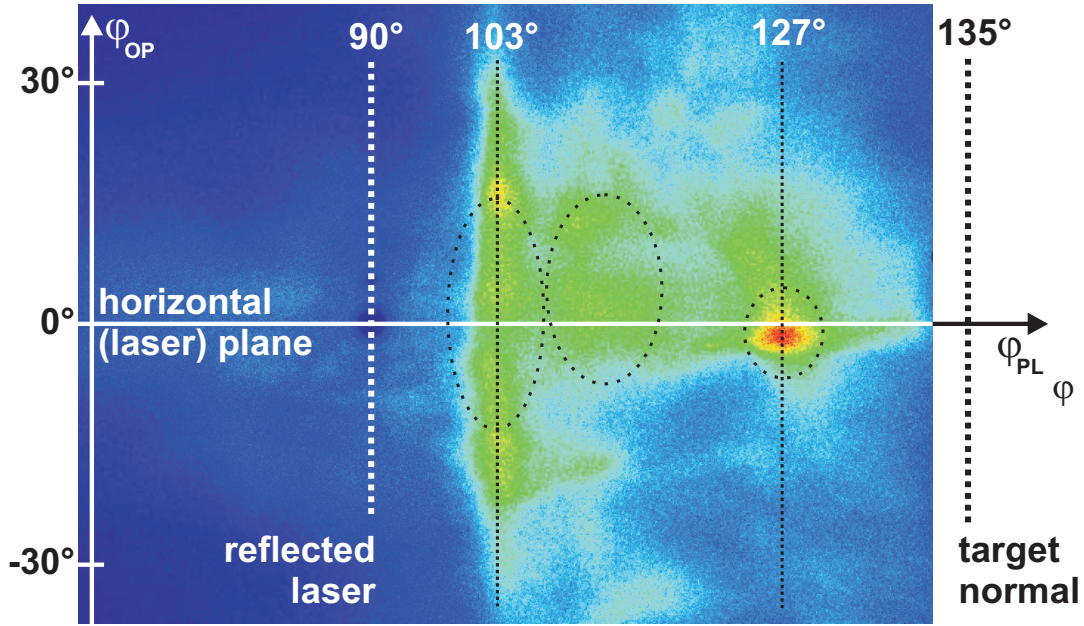


Figure 3.7: Typical 2D survey image of electrons detected with an IP for a single laser shot on an Al target. Emission is predominantly at distinct angles (highlighted regions) between target normal and the direction of the reflected laser. The colors range from blue for small to red for high electron signal. *Figure: Brandl et al. [14]*

metals. The simulation results for the angular distribution of the hot electrons flying out of the target front surface has been shown in Fig. 3.8, which compares the angular distribution of the hot electrons to the results when electron-ion collisions are switched off. The scattering angle of the hot electrons is counted from target normal. The hot electrons fly in a significantly broader angular cone in a collisional plasma and one can also observe several confinements of the energetic electrons in the cone of target normal and direction of the reflected laser. This is obviously a very remarkable agreement with the experimental results. On the other hand, obviously, collisionless plasma effects are insufficient to produce the experimental results, which proves that an interplay of the laser field electron acceleration and binary collisions in overdense plasma is needed to achieve the experimental observations.

The experimental electron energy spectra were also measured at such angles where strong emissions were found. Maximum energies above 150 keV were detected for all metal targets. This has been shown in Fig. 3.9. The highest energy attained by these electrons are much higher than the electrons can gain due to a purely ponderomotive acceleration. Hence, there has to be some other physical effect which plays an important role in accelerating the electrons to such high energies. This can better be understood with our PIC simulation results. The PIC simulation results for the electron energy spectrum are shown in Fig. 3.10, where the maximum kinetic energy obtained by the accelerated electrons is also above 150 keV, similar to the experiment. Once again, it has been noticed that, the collisionless plasma failed to reproduce the experimental

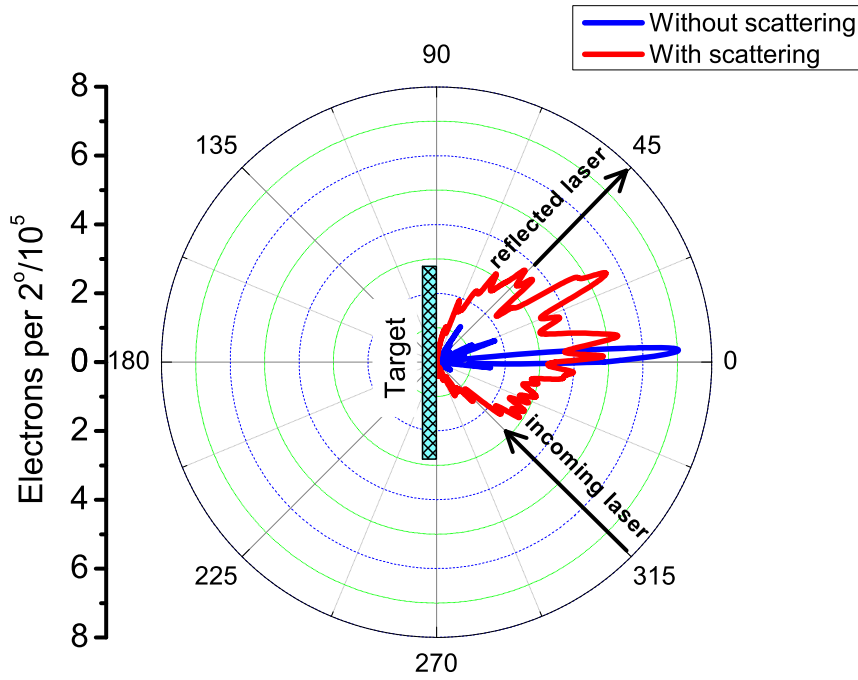


Figure 3.8: Angular distributions of the hot electrons obtained by PIC simulations with and without scattering. The experimental distribution of Fig. 3.7 can only be reproduced with scattering. 0° here corresponds to 135° in the experimental setup of Fig. 3.6

observations of spectrum. At this point one can conclude that the effects of plasma collisions in overdense plasma add up to the laser field ponderomotive acceleration of the electrons and steps up the maximum electron energy to significantly larger than $U_p = 4$ keV. This can be explained as, the electrons inside the target encounter several collisions and then get heated multiple times, which, in return, contributes to increase the electron kinetic energy. Hence, the unpredicted large peak in the electron kinetic energy is observed.

To get more insight into the energy distribution of the electrons confined into some regions as noticed in the experimental results of Fig. 3.7, we have studied the energy spectrum of each of these bunches at different angular cones in the collisional case. This has been shown in Fig. 3.11(I - VI). It is evident that most of the higher energy electrons fly in the range of $(15^\circ-35^\circ)$ and $(35^\circ-52^\circ)$ as depicted in Fig. 3.11(II) and (III). In all the other angular cones the electrons have much less energies. Referring to the Fig. 3.10, one can observe that the maximum energy of all the bulk accelerated electrons is over 150 keV and these higher energies are contributed by the electrons traveling other than along the specular direction. Moreover, the number of electrons in the region (II) and (III) is larger than the electrons flying on the other angular cones. Hence, the density of the confined electrons in the ranges (II) and (III) are much higher than others, which is also the experimental finding.

3.4. Directed Acceleration of Electrons from Solid Surface

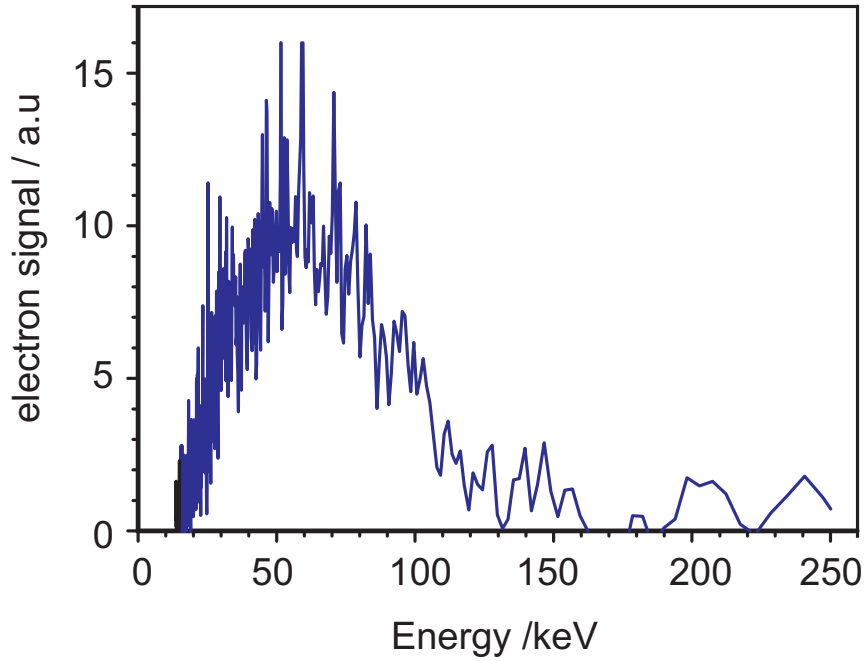


Figure 3.9: Experimental electron energy spectrum: Electron spectrum obtained close to the direction of the reflected laser for a single laser shot on a silver target. (Figure: Brandl et al. [14])

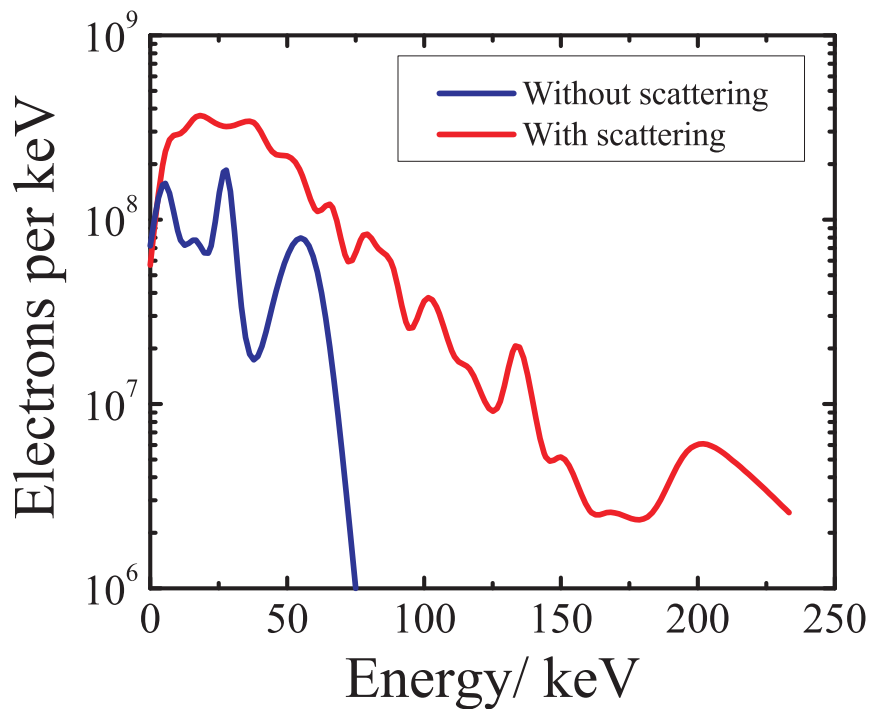


Figure 3.10: Energy spectrum from the 3D-PIC simulation: Electron energy spectra obtained by PIC simulations using collisional VLPL code with and without scattering. The experimental energies ≥ 70 keV can only be reproduced with scattering.

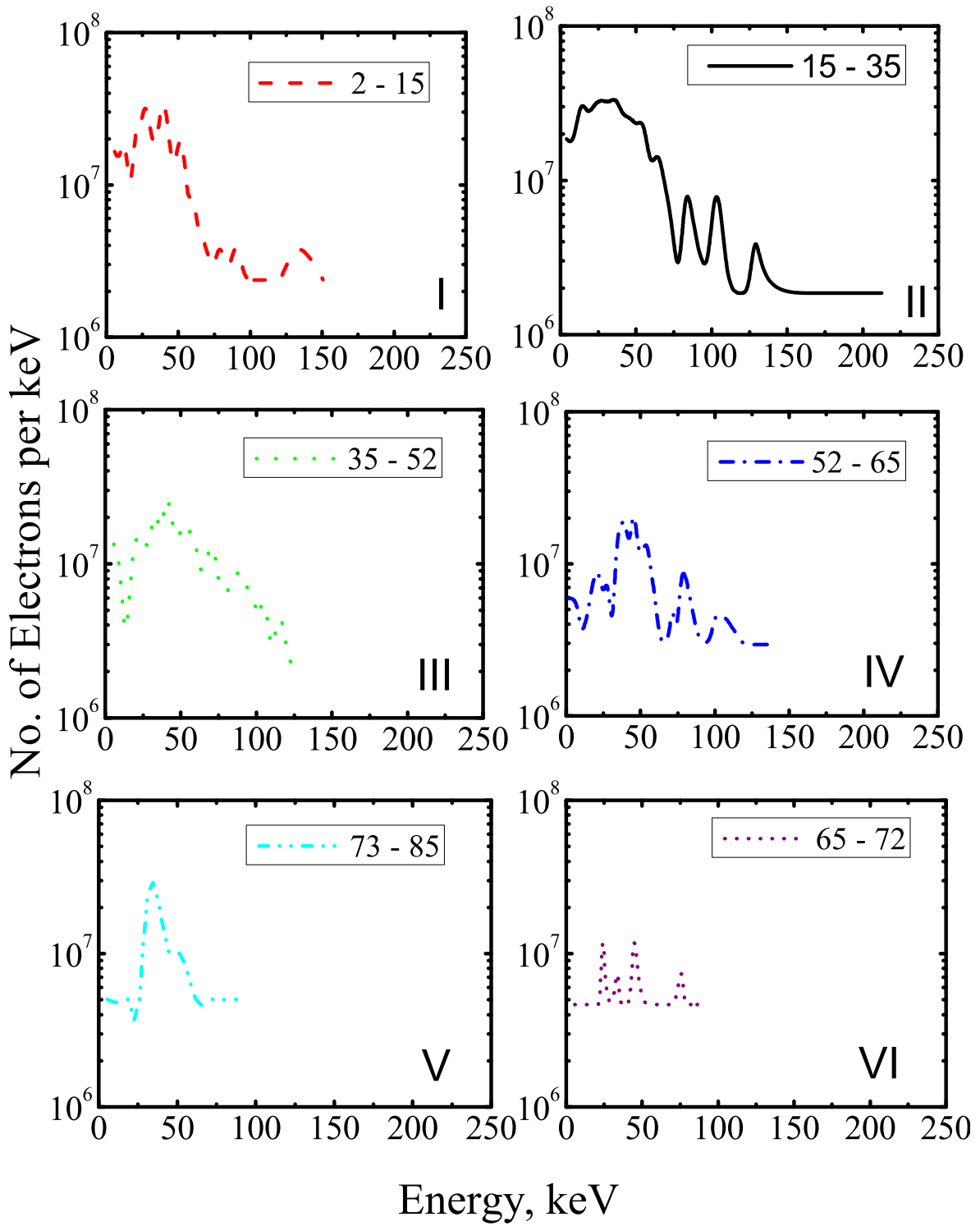


Figure 3.11: Energy spectra of the electrons in different angular ranges obtained by 3D-PIC simulations using scattering. The angular ranges are shown in the inset boxes. These angular ranges correspond to Fig. 3.8. The highest energy electrons fly in the angular cone of 15° to 35° .

3.5 Conclusion

In conclusion, a stochastic collisional algorithm has been implemented into the existing 3D-PIC code VLPL and this implementation has been successfully tested with a simple simulation of electron beam scattering in an overdense plasma. After this successful test, the experimental results of the directed acceleration of electrons from a solid target surface by sub-10-fs laser pulses has been reproduced and explained magnificently by the collisional VLPL code simulations. The directed electron ejection from solid surfaces was simulated using laser intensities in the range of 2×10^{16} W/cm² and pulse durations below 10 fs, i.e. only a few cycles of the electromagnetic field. In contrast to longer laser pulses, it turned out that plasma effects are of minor importance for the electron acceleration in this regime. The interaction is deterministic and governed by the interaction of the electromagnetic field with the single electrons, leading to distinct ejection angles. The unexpectedly high kinetic energies observed are explained by an interplay of acceleration in vacuum and scattering inside the solid target which leads to phase-delayed reemission into the field. In this way, the kinetic energies are boosted by accelerating single electron in subsequent cycles of one laser pulse. Another, more complex, simulation problem of collisional Weibel instability has also been performed and will be discussed in Chapter 5: Effects of Temperature and Collisions on the Weibel Instability.

4 Implicit PIC-Hydrodynamic Hybrid Simulation Code H-VLPL

4.1 Introduction: Motivation

Computer simulations are key tools in the study of laser-plasma interactions [91, 92]. Large full 3D parallel electromagnetic simulation codes like VLPL [95], OSIRIS [96], VORPAL [97], OOPIC [98], and others contributed remarkably in our understanding of the complex laser-plasma physics. Adding new physical processes in the codes, as well as doing large scale high-density plasma simulations are becoming more and more computationally expensive. As a result new algorithms and simulation techniques are being developed to cope with challenges of the laser-plasma physics.

One of the main reasons why the classical explicit Particle-in-Cell (PIC) methods are extremely computationally expensive is that they have to resolve the plasma frequency $\omega_p = \sqrt{4\pi n_e e^2 / m_e}$, which is the frequency of the plasma electrostatic oscillations. Therefore, they are limited to be applied to systems with lower plasma densities only.

On the contrary, there are increasing demands to simulate high-density plasmas, e.g., in the experiments where the laser pulse interacts with solid targets [54]. The solid state density plasmas densities vary over a range $100 - 1000 n_c$, where $n_c = m\omega^2 / 4\pi e^2$ is the critical plasma density. Here, m is the electron mass, $-e$ is its charge, and ω is the laser frequency. Other important applications include the Fast Ignition (FI) physics in the Inertial Confinement Fusion (ICF) studies [153]. The FI plasma has a density of the order of 1000 times compressed solid hydrogen, i.e., of the order of $10^5 n_c$. Hence, the applicability of the classical PIC codes in this density range is facing a big question. In this situation, one is forced to look for a more efficient numerical method to challenge those ultra-high densities. One of the possibilities is to include hydrodynamic description of the high-density plasma in the fully kinetic PIC code.

In last couple of years PIC-hydrodynamic hybrid techniques have emerged as an efficient solution to large scale ultra high-density plasma simulations, e.g., FI physics, solid state density plasma interactions, high charge and high energy ion production, etc. [154, 157, 158]. Most of these codes work in the Darwin approximation [159] and thus exclude the electromagnetic wave propagation completely. They also exclude electrostatic waves keeping the collisional magnetohydrodynamics (MHD) only. Further, implicit electrostatic particle-fluid hybrid plasma code has been developed by Rambo and Denavit [155], which has been used to study interpenetration and ion separation in colliding plasmas [156]. There is also the implicit electromagnetic PIC code LSP [160].

4. Implicit PIC-Hydrodynamic Hybrid Simulation Code H-VLPL

This code uses an implicit global scheme which leads to no such restrictions over time-step. The LSP code also employs a field solver based on an unconditionally Courant-stable algorithm [161] for electromagnetic calculations.

This chapter is solely devoted to the in-depth discussion of the physical model, numerical scheme and benchmarking of the newly developed PIC-Hydrodynamic hybrid code. This work has been performed in active collaboration with the colleagues from Applied Mathematics Institute, Heinrich-Heine-University, Düsseldorf.

The code Hybrid Virtual Laser Plasma Laboratory (H-VLPL) [55] is a hybrid code which unites a hydrodynamic model for overdense plasmas and the full kinetic description of hot low-density electrons and ions. The schematics in Fig. 4.1 illustrates the physical modelling of the H-VLPL code.

Hybrid Code for Relativistic Laser-Plasma

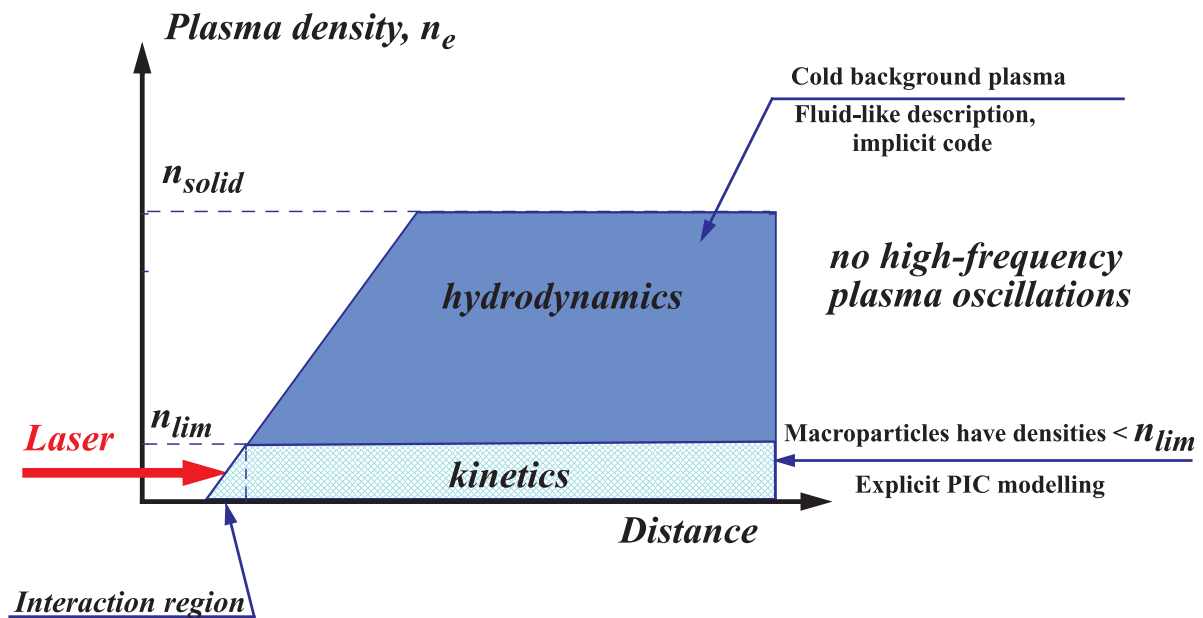


Figure 4.1: Schematics of the code H-VLPL. Low-density plasma is described kinetically using the explicit electromagnetic PIC technique. The cold overdense background plasma is described hydrodynamically. The full electromagnetic field solver is applied to the complete domain of simulations, also in the region of overdense plasma.

New matrix algorithms are developed to eradicate the time-step restrictions due to high plasma frequencies. Since the density of hot electrons is typically rather low, hybrid codes are expected to be more efficient than direct PIC codes. This allows us for simulations with physically relevant solid state densities. Although the code H-VLPL automatically reduces the highest numerical frequency to the stable range, the spatial description of the field distribution remains correct. Even when the grid step is much larger than the plasma skin depth, the algorithm gives the correct exponential decay of

4.2. The Hybrid Model

electromagnetic fields in overdense plasma layer (described in Section 4.5.4).

This chapter is arranged as follows. First, we describe the full hybrid method, in Section 4.2. Then, we write down the implicit numerical scheme and provide the computationally efficient matrix algorithm to solve the implicit set of equations, Section 4.3. In Section 4.4, we study the numerical dispersion relation for the new scheme and check its stability. Finally, we benchmark the new code H-VLPL extensively on a number of well-known physical examples in Section 4.5.

4.2 The Hybrid Model

We begin with writing down the master equations on the fields and particle momenta:

$$\frac{\partial \vec{E}}{\partial t} = c \nabla \times \vec{B} - 4\pi \sum_{\ell} \vec{J}_{\ell}, \quad \ell = e, i, h \quad (4.1a)$$

$$\frac{\partial \vec{B}}{\partial t} = -c \nabla \times \vec{E} \quad (4.1b)$$

$$\frac{d\vec{p}_h}{dt} = q_e \vec{E} - \nu m_e \vec{v}_h \quad (4.1c)$$

$$\frac{d\vec{p}_{\ell}}{dt} = q_{\ell} \left(\vec{E} + \frac{\vec{v}_{\ell}}{c} \times \vec{B} \right), \quad \ell = e, i \quad (4.1d)$$

where

$$\vec{J}_{\ell} = q_{\ell} n_{\ell} \vec{v}_{\ell}, \quad \vec{p}_{\ell} = m_{\ell} \gamma_{\ell} \vec{v}_{\ell}, \quad \gamma_{\ell} = \sqrt{1 + \frac{p_{\ell}^2}{(m_{\ell} c)^2}}, \quad \nu = \eta n_h.$$

The index $\ell = e, i, h$ refers to electrons, ions, and hybrid particles, respectively. \vec{E} and \vec{B} denote the electric and magnetic field vectors, \vec{J} denotes the current density, \vec{p} is the momentum and n is the number density of particles. The parameter ν denotes collision frequency that defines the cold plasma conductivity.

Eqs. (4.1a) – (4.1b) show that we use the unabridged Maxwell equations and thus include the full physics of electromagnetic waves. Eq. (4.1d) corresponds to the fully kinetic algorithm for the low-density electrons and ions.

It is essential here to explain the meaning of Eq. (4.1c). The “hybrid particles” are assumed to be compound quasineutral objects, i.e., the negative charge of electrons within the hybrid particles is fully compensated by the positive charge of the ions. The electrostatic force of the “hybrid ions” is so strong that the “hybrid electrons” cannot be separated. At present, in our scheme the hybrid particles do not move as a whole. At the same time, the electrons within the hybrid particle are allowed to have non-zero momenta \vec{p}_h and to generate currents $\vec{J}_h = -en_h \vec{v}_h$. Thus, the hybrid particles are purely current carriers for the present scheme. This kind of plasma description corresponds to the single fluid MHD model [57]. Because the “hybrid electrons” are

assumed to move slowly, $v_h \ll c$, and we are interested in their response to fast electric fields only, hence, we neglect the $\vec{v} \times \vec{B}/c$ term in the Lorentz force (4.1c). A further extension to this present scheme taking into account the hybrid particle dynamics as a whole will be presented elsewhere.

For modeling the kinetic part we use the standard Cloud-In-Cell (CIC) interpolation scheme. On the other hand, the hybrid particles are presently point like and are treated with Nearest Grid Point (NGP) interpolations. One has to mention here that, the kinetic part of the code exploits the energy conservative scheme, which has been benchmarked later in Section 4.5.2.

4.3 The Numerical Algorithm of H-VLPL

For simplicity, we rewrite the equations in dimensionless variables, $\tilde{t} = \omega_0 t$ and $\tilde{x} = k_0 x$, where ω_0 denotes the laser frequency and $k_0 = \omega_0/c$. The new set of variables are then

$$\tilde{E} = \frac{eE}{m_e c \omega_0}, \quad \tilde{B} = \frac{eB}{m_e c \omega_0}, \quad \tilde{p}_h = \frac{p_h}{m_e c}, \quad \tilde{p}_\ell = \frac{p_\ell}{m_\ell c}, \quad \ell = e, i,$$

and

$$\tilde{J}_\ell = \frac{J_\ell}{j_c}, \quad j_c = en_e c, \quad \tilde{\rho} = \frac{n}{n_c}, \quad \tilde{q}_\ell = \frac{q_\ell m_e}{e m_\ell}, \quad \tilde{v}_\ell = \frac{v_\ell}{c}, \quad \tilde{\nu} = \frac{\nu}{\omega_0}.$$

In Sections 4.3 and 4.4 we choose the ρ notation instead of the usual n for the number densities of particles to avoid a possible confusion with the time step number n .

In the following, we omit the tildes. Eq. (4.1) then reads

$$\frac{\partial \vec{E}}{\partial t} = \nabla \times \vec{B} - \sum_\ell \vec{J}_\ell, \quad \ell = e, i, h \quad (4.2a)$$

$$\frac{\partial \vec{B}}{\partial t} = -\nabla \times \vec{E} \quad (4.2b)$$

$$\frac{d\vec{p}_h}{dt} = -\vec{E} - \nu \vec{v}_h \quad (4.2c)$$

$$\frac{d\vec{p}_\ell}{dt} = q_\ell (\vec{E} + \vec{v}_\ell \times \vec{B}), \quad \ell = e, i. \quad (4.2d)$$

Suitable boundary conditions for the simulation of a laser-plasma interaction are inhomogeneous, time dependent Dirichlet boundary conditions for the incoming laser(s).

We consider the problem in one space dimension at the moment, i.e., all vectors are of the form

$$\vec{V} = [V_x(t, x), V_y(t, x), V_z(t, x)]^T, \quad x \in [0, L]$$

4.3. The Numerical Algorithm of H-VLPL

We thus have explicitly $B_x(t, x) = 0$ for the current system.

Following [91] we define the field quantities as

$$F_y^\pm = \frac{1}{2}(E_y \pm B_z), \quad F_z^\pm = \frac{1}{2}(E_z \pm B_y). \quad (4.3)$$

If we denote the sum of all currents, derived from the PIC scheme, with \vec{J} (4.2a)–(4.2c) are equivalent to

$$\frac{\partial F_y^\pm}{\partial t} = \mp \frac{\partial F_y^\pm}{\partial x} + \frac{1}{2}\rho_h v_{h,y} - \frac{1}{2}J_y \quad (4.4a)$$

$$\frac{\partial F_z^\pm}{\partial t} = \pm \frac{\partial F_z^\pm}{\partial x} + \frac{1}{2}\rho_h v_{h,z} - \frac{1}{2}J_z \quad (4.4b)$$

$$\frac{dp_{h,y}}{dt} = -(F_y^+ + F_y^-) - \eta\rho_h v_{h,y} \quad (4.4c)$$

$$\frac{dp_{h,z}}{dt} = -(F_z^+ + F_z^-) - \eta\rho_h v_{h,z}. \quad (4.4d)$$

The boundary conditions are given by $F_y^+(0) = F_z^-(0) = g(t)$ and $F_y^-(L) = F_z^+(L) = 0$.

For the numerical discretization we use an equidistant staggered grid in space and time with spatial step size $h = L/m$ for some positive integer m and temporal step size $\tau > 0$. The fields at grid point j and time $t_n = n\tau$ are denoted by F_j^n , $j = 0, \dots, m$, $n \geq 0$. The field equations are integrated along the vacuum characteristics ($x \mp t = \text{constant}$) which implies $h = \tau$. We discretize the fields E and B and the momenta p_h , p_e . The current \vec{J}_h and the velocity are computed via $\vec{J}_h = -\rho_h \vec{p}_h / \gamma_h = -\rho_h \vec{v}_h$. Fig. 4.2 shows the staggered grid and the location of the variables.

We suggest the following implicit finite difference scheme for solving (4.4):

$$\frac{(E_x)_j^{n+1} - (E_x)_j^n}{\tau} = (\rho_h v_{h,x})_j^{n+\frac{1}{2}} - (J_x)_j^{n+\frac{1}{2}} \quad (4.5a)$$

$$\frac{(p_{h,x})_j^{n+1} - (p_{h,x})_j^n}{\tau} = -\frac{(E_x)_j^{n+1} + (E_x)_j^n}{2} - \eta(\rho_h v_{h,x})_j^{n+1} \quad (4.5b)$$

$$\frac{(F_y^+)_{j+1}^{n+1} - (F_y^+)_{j+1}^n}{\tau} = -\frac{(F_y^+)_{j+1}^n - (F_y^+)_{j+1}^n}{h} + \frac{1}{2}(\rho_h v_{h,y})_{j+\frac{1}{2}}^{n+\frac{1}{2}} - \frac{1}{2}(J_y)_{j+\frac{1}{2}}^{n+\frac{1}{2}} \quad (4.5c)$$

$$\frac{(F_y^-)_{j+1}^{n+1} - (F_y^-)_{j+1}^n}{\tau} = \frac{(F_y^-)_{j+1}^n - (F_y^-)_{j+1}^n}{h} + \frac{1}{2}(\rho_h v_{h,y})_{j+\frac{1}{2}}^{n+\frac{1}{2}} - \frac{1}{2}(J_y)_{j+\frac{1}{2}}^{n+\frac{1}{2}} \quad (4.5d)$$

$$\frac{(p_{h,y})_j^{n+1} - (p_{h,y})_j^n}{\tau} = -\frac{(F_y^+)_{j+1}^{n+1} + (F_y^+)_{j+1}^n + (F_y^-)_{j+1}^{n+1} + (F_y^-)_{j+1}^n}{2} - \eta(\rho_h v_{h,y})_j^{n+1} \quad (4.5e)$$

$$\frac{(F_z^+)_{j+1}^{n+1} - (F_z^+)_{j+1}^n}{\tau} = \frac{(F_z^+)_{j+1}^n - (F_z^+)_{j+1}^n}{h} + \frac{1}{2}(\rho_h v_{h,z})_{j+\frac{1}{2}}^{n+\frac{1}{2}} - \frac{1}{2}(J_z)_{j+\frac{1}{2}}^{n+\frac{1}{2}} \quad (4.5f)$$

$$\frac{(F_z^-)_{j+1}^{n+1} - (F_z^-)_{j+1}^n}{\tau} = -\frac{(F_z^-)_{j+1}^n - (F_z^-)_{j+1}^n}{h} + \frac{1}{2}(\rho_h v_{h,z})_{j+\frac{1}{2}}^{n+\frac{1}{2}} - \frac{1}{2}(J_z)_{j+\frac{1}{2}}^{n+\frac{1}{2}} \quad (4.5g)$$

$$\frac{(p_{h,z})_j^{n+1} - (p_{h,z})_j^n}{\tau} = -\frac{(F_z^+)_{j+1}^{n+1} + (F_z^+)_{j+1}^n + (F_z^-)_{j+1}^{n+1} + (F_z^-)_{j+1}^n}{2} - \eta(\rho_h v_{h,z})_j^{n+1}, \quad (4.5h)$$

Within this scheme, we approximate

$$(\rho_h v_{h,x})_j^{n+\frac{1}{2}} = \frac{(\zeta_h)_j^n}{2} ((p_{h,x})_j^{n+1} + (p_{h,x})_j^n) \quad (4.6a)$$

$$\begin{aligned} (\rho_h v_{h,s})_{j+\frac{1}{2}}^{n+\frac{1}{2}} &= \frac{(\zeta_h)_j^n}{4} ((p_{h,s})_j^{n+1} + (p_{h,s})_j^n) \\ &\quad + \frac{(\zeta_h)_{j+1}^n}{4} ((p_{h,s})_{j+1}^{n+1} + (p_{h,s})_{j+1}^n), \quad s = y, z \end{aligned} \quad (4.6b)$$

$$(\rho_h v_{h,s})_j^{n+1} = (\zeta_h)_j^n (p_{h,s})_j^{n+1}, \quad s = x, y, z, \quad (4.6c)$$

where $\zeta_h = \rho_h/\gamma_h$. This leads to the following scheme for the x -component

$$\begin{aligned} (E_x)_j^{n+1} &= \frac{1}{(K^+)_j^n} \left((K^-)_j^n (E_x)_j^n + \frac{\tau(\zeta_h)_j^n (p_{h,x})_j^n}{2} \left(1 + \frac{1}{1 + \tau\eta(\zeta_h)_j^n} \right) \right. \\ &\quad \left. - \tau(J_x)_j^{n+\frac{1}{2}} \right) \end{aligned} \quad (4.7a)$$

$$(p_{h,x})_j^{n+1} = \frac{(p_{h,x})_j^n - \frac{\tau}{2} ((E_x)_j^{n+1} + (E_x)_j^n)}{1 + \tau\eta(\zeta_h)_j^n}, \quad (4.7b)$$

where

4.3. The Numerical Algorithm of H-VLPL

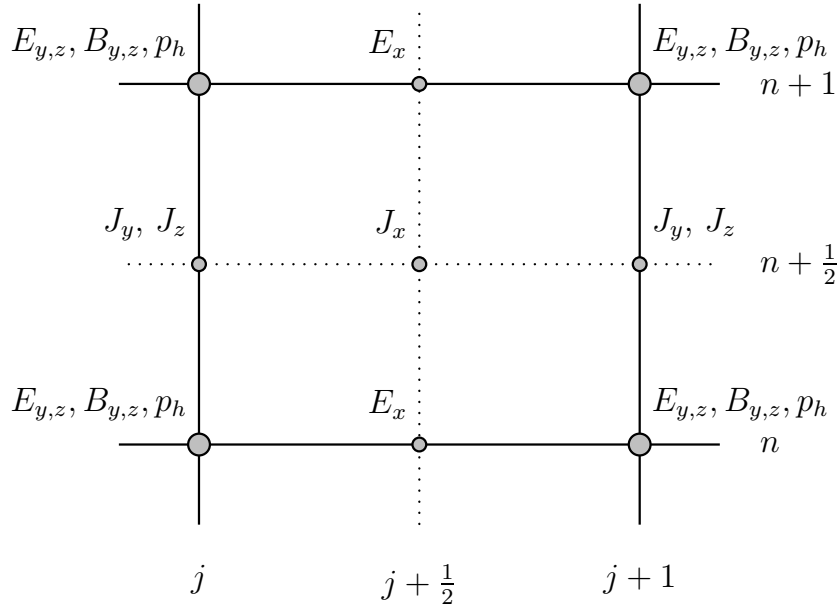


Figure 4.2: The staggered grid system and the location of the variables for the finite difference scheme (4.5). The transverse E and B field components and the hybrid momentum p_h are calculated on the local grid points, whereas, longitudinal field component E_x and the current J_x are calculated at half a grid. The transverse current components J_y and J_z are calculated over half a time-step on the grid points.

$$K^\pm = 1 \pm \frac{\tau^2 \zeta_h}{4(1 + \tau \eta \zeta_h)}.$$

However, for the y -component we obtain the implicit scheme

$$\begin{aligned} (F_y^+)_{j+1}^{n+1} &= \frac{\tau(\zeta_h)_j^n}{8}(p_{h,y})_j^{n+1} - \frac{\tau(\zeta_h)_{j+1}^n}{8}(p_{h,y})_{j+1}^{n+1} \\ &= (F_y^+)_j^n + \frac{\tau(\zeta_h)_j^n}{8}(p_{h,y})_j^n + \frac{\tau(\zeta_h)_{j+1}^n}{8}(p_{h,y})_{j+1}^n - \frac{\tau}{2}(J_y)_{j+\frac{1}{2}}^{n+\frac{1}{2}} \end{aligned} \quad (4.8a)$$

$$\begin{aligned} (F_y^-)_{j+1}^{n+1} &= \frac{\tau(\zeta_h)_j^n}{8}(p_{h,y})_j^{n+1} - \frac{\tau(\zeta_h)_{j+1}^n}{8}(p_{h,y})_{j+1}^{n+1} \\ &= (F_y^-)_{j+1}^n + \frac{\tau(\zeta_h)_j^n}{8}(p_{h,y})_j^n + \frac{\tau(\zeta_h)_{j+1}^n}{8}(p_{h,y})_{j+1}^n - \frac{\tau}{2}(J_y)_{j+\frac{1}{2}}^{n+\frac{1}{2}} \end{aligned} \quad (4.8b)$$

$$\begin{aligned} (1 + \tau \eta) & (\zeta_h)_j^n (p_{h,y})_j^{n+1} + \frac{\tau}{2}(F_y^+)_{j+1}^{n+1} + \frac{\tau}{2}(F_y^-)_{j+1}^{n+1} \\ &= (p_{h,y})_j^n - \frac{\tau}{2}(F_y^+)_j^n - \frac{\tau}{2}(F_y^-)_j^n. \end{aligned} \quad (4.8c)$$

Next we consider the efficient solution of the linear system for the y -component. For $Y = [(F_y^+)_{1, \dots, (F_y^+)_m, (F_y^-)_{0, \dots, (F_y^-)_{m-1}, (p_{h,y})_{0, \dots, (p_{h,y})_m}]^T$ we obtain

4. Implicit PIC-Hydrodynamic Hybrid Simulation Code H-VLPL

$$AY^{n+1} = BY^n + f(t), \quad (4.9)$$

where f contains the boundary conditions and the electron currents (from the PIC code), and

$$A = \left[\begin{array}{c|c} I_{2m} & D \\ \hline C & G \end{array} \right] \quad \text{and} \quad B = \left[\begin{array}{cc|c} S_m^T & 0 & -D \\ 0 & S_m & \\ \hline -C & & I_{m+1} \end{array} \right].$$

Here I_k denotes the $k \times k$ identity matrix and $G = \text{diag}(1 + \tau\eta(\zeta_h)_j^n) \in \mathbb{R}^{(m+1) \times (m+1)}$. S_k represents the $k \times k$ shift matrix with ones on the first upper diagonal and zeros elsewhere. $C \in \mathbb{R}^{(m+1) \times 2m}$ and $D \in \mathbb{R}^{2m \times (m+1)}$ are given by

$$C = \frac{\tau}{2} \left[\begin{array}{c|c} 0 & I_m \\ \hline I_m & 0 \end{array} \right], \quad D = -\frac{\tau}{8} \left[\begin{array}{c} \text{bidiag}((\zeta_h)_j^n, (\zeta_h)_{j+1}^n)_{j=0}^{m-1} \\ \text{bidiag}((\zeta_h)_j^n, (\zeta_h)_{j+1}^n)_{j=0}^{m-1} \end{array} \right],$$

where $\text{bidiag}(a_j, b_j)_{j=1, m}$ denotes an $m \times (m+1)$ bidiagonal matrix with a_j as the j th diagonal entry and b_j as the j th upper diagonal entry.

This large linear system can be solved efficiently by using block Gaussian elimination

$$A = \left[\begin{array}{c|c} I_{2m} & D \\ \hline C & G \end{array} \right] = \left[\begin{array}{c|c} I_{2m} & 0 \\ \hline C & I_{m+1} \end{array} \right] \left[\begin{array}{c|c} I_{2m} & D \\ \hline 0 & T \end{array} \right],$$

where $T = G - CD$ is the tridiagonal matrix containing the Schur complement [162] of A . Thus the solution of (4.9) can be reduced to solving a linear system with the tridiagonal matrix T of size $m+1$.

Finally, the scheme for the z -component is given by

$$\begin{aligned} (F_z^+)_{j+1}^{n+1} & - \frac{\tau(\zeta_h)_j^n}{8} (p_{h,z})_j^{n+1} - \frac{\tau(\zeta_h)_{j+1}^n}{8} (p_{h,z})_{j+1}^{n+1} \\ & = (F_z^+)_{j+1}^n + \frac{\tau(\zeta_h)_j^n}{8} (p_{h,z})_j^n + \frac{\tau(\zeta_h)_{j+1}^n}{8} (p_{h,z})_{j+1}^n - \frac{\tau}{2} (J_z)_{j+\frac{1}{2}}^{n+\frac{1}{2}} \end{aligned} \quad (4.10a)$$

$$\begin{aligned} (F_z^-)_{j+1}^{n+1} & - \frac{\tau(\zeta_h)_j^n}{8} (p_{h,z})_j^{n+1} - \frac{\tau(\zeta_h)_{j+1}^n}{8} (p_{h,z})_{j+1}^{n+1} \\ & = (F_z^-)_{j+1}^n + \frac{\tau(\zeta_h)_j^n}{8} (p_{h,z})_j^n + \frac{\tau(\zeta_h)_{j+1}^n}{8} (p_{h,z})_{j+1}^n - \frac{\tau}{2} (J_z)_{j+\frac{1}{2}}^{n+\frac{1}{2}} \end{aligned} \quad (4.10b)$$

$$\begin{aligned} (1 + \tau\eta) (\zeta_h)_j^n (p_{h,z})_j^{n+1} & + \frac{\tau}{2} (F_z^+)_{j+1}^{n+1} + \frac{\tau}{2} (F_z^-)_{j+1}^{n+1} \\ & = (p_{h,z})_j^n - \frac{\tau}{2} (F_z^+)_{j+1}^n - \frac{\tau}{2} (F_z^-)_{j+1}^n. \end{aligned} \quad (4.10c)$$

The resulting linear system is solved analogously to the one for the y -component.

4.4 Numerical Dispersion and Stability

In this section we will derive the dispersion relations for the hybrid scheme (4.5) applied to the dimensionless equations (4.2). In dimensionless variables the plasma frequency is given by

$$\tilde{\omega}_\ell = \omega_\ell/\omega_0 = \sqrt{\tilde{\rho}_\ell}, \quad \ell = e, h. \quad (4.11)$$

We again omit the tildes, set $\gamma_\ell = 1$ and $\rho_\ell = \text{const.}$ The explicit PIC scheme is stable for step sizes

$$\tau \leq \frac{2}{\omega_e} \quad (4.12)$$

Therefore it is prohibitive to use this scheme for high densities.

4.4.1 Dispersion relation for the x-component

Due to $B_x(t, x) = 0$ we have

$$\frac{\partial \vec{E}}{\partial t} = \rho_h \vec{p}_h + \rho_e \vec{p}_e \quad (4.13a)$$

$$\frac{d\vec{p}_h}{dt} = -\vec{E} - \nu \vec{v}_h \quad (4.13b)$$

$$\frac{d\vec{p}_e}{dt} = -\vec{E} \quad (4.13c)$$

to obtain the dispersion relation for the x -component.

The finite difference scheme of (4.13) is given by

$$\frac{(E_x)_j^{n+1} - (E_x)_j^n}{\tau} = \rho_h \frac{(p_{h,x})_j^{n+1} + (p_{h,x})_j^n}{2} + \rho_e (p_{e,x})_j^{n+\frac{1}{2}} \quad (4.14a)$$

$$\frac{(p_{h,x})_j^{n+1} - (p_{h,x})_j^n}{\tau} = -\frac{(E_x)_j^{n+1} + (E_x)_j^n}{2} - \eta \rho_h (p_{h,x})_j^{n+1} \quad (4.14b)$$

$$\frac{(p_{e,x})_j^{n+\frac{1}{2}} - (p_{e,x})_j^{n-\frac{1}{2}}}{\tau} = -(E_x)_j^n. \quad (4.14c)$$

Substituting plane waves one gets

$$(E_x)_j^n = E_0 e^{i(\omega n \tau - k j h)}, \quad (4.15a)$$

$$(p_{h,x})_j^n = (p_h)_0 e^{i(\omega n \tau - k j h)}, \quad (4.15b)$$

$$(p_{e,x})_j^n = (p_e)_0 e^{i(\omega n \tau - k j h)} \quad (4.15c)$$

into (4.14) and using (4.11) leads to

$$iE_0 \sin \frac{\omega\tau}{2} = \frac{\tau\omega_h^2}{2}(p_h)_0 \cos \frac{\omega\tau}{2} + \frac{\tau\omega_e^2}{2}(p_e)_0, \quad (4.16a)$$

$$i(p_h)_0 \sin \frac{\omega\tau}{2} = -\frac{\tau}{2}E_0 \cos \frac{\omega\tau}{2} - \frac{\tau\eta\omega_h^2}{2}(p_h)_0 e^{i\frac{\omega\tau}{2}}, \quad (4.16b)$$

$$2i(p_e)_0 \sin \frac{\omega\tau}{2} = -\tau E_0. \quad (4.16c)$$

Solving (4.16b) for $(p_h)_0$, (4.16c) for $(p_e)_0$ and inserting into (4.16a) yields

$$\sin^2 \frac{\omega\tau}{2} = \left(\frac{\tau\omega_h}{2}\right)^2 \frac{\cos^2 \frac{\omega\tau}{2} \sin \frac{\omega\tau}{2}}{\sin \frac{\omega\tau}{2} - i\frac{\tau\eta\omega_h^2}{2}e^{i\frac{\omega\tau}{2}}} + \left(\frac{\tau\omega_e}{2}\right)^2 \quad (4.17)$$

and for $\eta = 0$ we obtain

$$\omega = \frac{2}{\tau} \arccos \sqrt{\frac{1 - \left(\frac{\tau\omega_e}{2}\right)^2}{1 + \left(\frac{\tau\omega_h}{2}\right)^2}}. \quad (4.18)$$

The numerical dispersion relation (4.18) shows that the scheme is unconditionally stable for $\tau \leq 2/\omega_e$, i.e., independent of ω_h . This step size restriction is due to the explicit PIC code. Note that in our hybrid model we have $\omega_e \ll \omega_h$, so this restriction is not severe.

For $\eta \neq 0$, the stability analysis is more involved since we have complex coefficients in the relation (4.18). In general, this leads to complex valued solutions ω . Therefore, we verified numerically, that the scheme is stable for $\tau \in (0, 2/\omega_e)$ and $\eta \in [0, 1]$.

4.4.2 Dispersion relation for the y- and the z-component

For the y -component we have

$$\frac{\partial F_y^+}{\partial t} = -\frac{\partial}{\partial x} F_y^+ + \frac{1}{2}\rho_h p_{h,y} - \frac{1}{2}J_y \quad (4.19a)$$

$$\frac{\partial F_y^-}{\partial t} = \frac{\partial}{\partial x} F_y^- + \frac{1}{2}\rho_h p_{h,y} - \frac{1}{2}J_y \quad (4.19b)$$

$$\frac{dp_{h,y}}{dt} = -(F_y^+ + F_y^-) - \eta\rho_h p_{h,y} \quad (4.19c)$$

$$\frac{dp_{e,y}}{dt} = -E_y \quad (4.19d)$$

The finite difference scheme then reads

4.4. Numerical Dispersion and Stability

$$(F_y^+)_{j+1}^{n+1} - (F_y^+)_{j+1}^n = -(F_y^+)_{j+1}^n + (F_y^+)_{j+1}^n + \frac{\tau}{2}\rho_h(p_{h,y})_{j+\frac{1}{2}}^{n+\frac{1}{2}} - \frac{\tau}{2}(J_y)_{j+\frac{1}{2}}^{n+\frac{1}{2}} \quad (4.20a)$$

$$(F_y^-)_{j+1}^{n+1} - (F_y^-)_{j+1}^n = (F_y^-)_{j+1}^n - (F_y^-)_{j+1}^n + \frac{\tau}{2}\rho_h(p_{h,y})_{j+\frac{1}{2}}^{n+\frac{1}{2}} - \frac{\tau}{2}(J_y)_{j+\frac{1}{2}}^{n+\frac{1}{2}} \quad (4.20b)$$

$$(p_{h,y})_j^{n+1} - (p_{h,y})_j^n = -\frac{\tau}{2}\left((F_y^+)_{j+1}^{n+1} + (F_y^+)_{j+1}^n + (F_y^-)_{j+1}^{n+1} + (F_y^-)_{j+1}^n\right) - \tau\eta\rho_h(p_{h,y})_j^{n+1} \quad (4.20c)$$

$$(p_{e,y})_j^{n+\frac{1}{2}} - (p_{e,y})_j^{n-\frac{1}{2}} = -\tau(E_y)_j^n. \quad (4.20d)$$

For the dispersion relation, we rewrite (4.20) in terms of the original fields E and B :

$$(E_y)_{j+1}^{n+1} - (E_y)_j^n = -(B_z)_{j+1}^{n+1} + (B_z)_j^n + \tau\omega_h^2 \frac{(p_{h,y})_j^{n+1} + (p_{h,y})_j^n + (p_{h,y})_{j+1}^{n+1} + (p_{h,y})_{j+1}^n}{4} + \tau\omega_e^2 \frac{(p_{e,y})_j^{n+\frac{1}{2}} + (p_{e,y})_{j+1}^{n+\frac{1}{2}}}{2} \quad (4.21a)$$

$$(E_y)_j^{n+1} - (E_y)_{j+1}^n = (B_z)_j^{n+1} - (B_z)_{j+1}^n + \tau\omega_h^2 \frac{(p_{h,y})_j^{n+1} + (p_{h,y})_j^n + (p_{h,y})_{j+1}^{n+1} + (p_{h,y})_{j+1}^n}{4} + \tau\omega_e^2 \frac{(p_{e,y})_j^{n+\frac{1}{2}} + (p_{e,y})_{j+1}^{n+\frac{1}{2}}}{2} \quad (4.21b)$$

$$-\tau \frac{(E_y)_j^{n+1} + (E_y)_j^n}{2} = (1 + \tau\eta\omega_h^2)(p_{h,y})_j^{n+1} - (p_{h,y})_j^n \quad (4.21c)$$

$$-\tau(E_y)_j^n = (p_{e,y})_j^{n+\frac{1}{2}} - (p_{e,y})_j^{n-\frac{1}{2}}. \quad (4.21d)$$

Adding and subtracting (4.21a) and (4.21b) yields

$$(E_y)_{j+1}^{n+1} + (E_y)_j^{n+1} - (E_y)_j^n - (E_y)_{j+1}^n = (B_z)_j^{n+1} + (B_z)_j^n - (B_z)_{j+1}^{n+1} - (B_z)_{j+1}^n + \tau\omega_h^2 \frac{(p_{h,y})_j^{n+1} + (p_{h,y})_j^n + (p_{h,y})_{j+1}^{n+1} + (p_{h,y})_{j+1}^n}{2} + \tau\omega_e^2 \left((p_{e,y})_j^{n+\frac{1}{2}} + (p_{e,y})_{j+1}^{n+\frac{1}{2}} \right) \quad (4.22a)$$

$$(E_y)_{j+1}^{n+1} + (E_y)_{j+1}^n - (E_y)_j^{n+1} - (E_y)_j^n = (B_z)_j^{n+1} + (B_z)_j^n - (B_z)_{j+1}^{n+1} - (B_z)_{j+1}^n. \quad (4.22b)$$

Analogously to (4.15) we substitute plane waves, which gives

$$\begin{aligned}
 iE_0 \sin \frac{\omega\tau}{2} \cos \frac{k\tau}{2} &= -iB_0 \cos \frac{\omega\tau}{2} \sin \frac{k\tau}{2} + (p_h)_0 \frac{\tau\omega_h^2}{2} \cos \frac{\omega\tau}{2} \cos \frac{k\tau}{2} \\
 &+ \frac{\tau\omega_e^2}{2} \cos \frac{k\tau}{2} (p_e)_0
 \end{aligned} \tag{4.23a}$$

$$iE_0 \sin \frac{k\tau}{2} \cos \frac{\omega\tau}{2} = -iB_0 \sin \frac{\omega\tau}{2} \cos \frac{k\tau}{2} \tag{4.23b}$$

$$-\tau E_0 \cos \frac{\omega\tau}{2} = (p_h)_0 \left(2i \sin \frac{\omega\tau}{2} + \tau\eta\omega_h^2 e^{i\frac{\omega\tau}{2}} \right) \tag{4.23c}$$

$$2i(p_e)_0 \sin \frac{\omega\tau}{2} = -\tau E_0. \tag{4.23d}$$

Solving (4.23b) for B_0 , (4.23c) for $(p_h)_0$, (4.23d) for $(p_e)_0$ and inserting into (4.23a) yields

$$\sin^2 \frac{\omega\tau}{2} \cos^2 \frac{k\tau}{2} = \cos^2 \frac{\omega\tau}{2} \sin^2 \frac{k\tau}{2} + \left(\frac{\tau\omega_h}{2} \right)^2 \frac{\cos^2 \frac{\omega\tau}{2} \cos^2 \frac{k\tau}{2} \sin \frac{\omega\tau}{2}}{\sin \frac{\omega\tau}{2} - i\frac{\tau\eta\omega_h^2}{2} e^{i\frac{\omega\tau}{2}}} + \left(\frac{\tau\omega_e}{2} \right)^2 \cos^2 \frac{k\tau}{2},$$

from which we obtain

$$\cos^2 \frac{\omega\tau}{2} \left(1 + \left(\frac{\tau\omega_h}{2} \right)^2 \frac{\cos^2 \frac{k\tau}{2} \sin \frac{\omega\tau}{2}}{\sin \frac{\omega\tau}{2} - i\frac{\tau\eta\omega_h^2}{2} e^{i\frac{\omega\tau}{2}}} \right) = \cos^2 \frac{k\tau}{2} \left(1 - \left(\frac{\tau\omega_e}{2} \right)^2 \right). \tag{4.24}$$

For $\cos^2 \frac{k\tau}{2} = 1$, this is the same dispersion relation as for the x -component. Again, we solved the relation numerically and verified stability for $\tau \in (0, 2/\omega_e)$, and $\cos^2 \frac{k\tau}{2} \in [0, 1]$.

For $\eta = 0$, the dispersion relation reads

$$\cos^2 \frac{\omega\tau}{2} = \frac{\cos^2 \frac{k\tau}{2} (1 - (\frac{\tau\omega_e}{2})^2)}{1 + (\frac{\tau\omega_h}{2})^2 \cos^2 \frac{k\tau}{2}} =: \xi^2 \tag{4.25}$$

and we obtain

$$\omega = \frac{2}{\tau} \arccos \xi.$$

This shows that the scheme is unconditionally stable for $\tau \leq 2/\omega_e$.

In Fig. 4.3 analytical plots for the real and imaginary parts of $k(\omega)$ are presented for $\eta = 0$, $\omega_e = 0$, $\omega_h = 31.6$, $\tau = 0.05$ and $\omega \in [0, \frac{\pi}{2\tau}]$.

Analogously, one can obtain the same relation for the z -component.

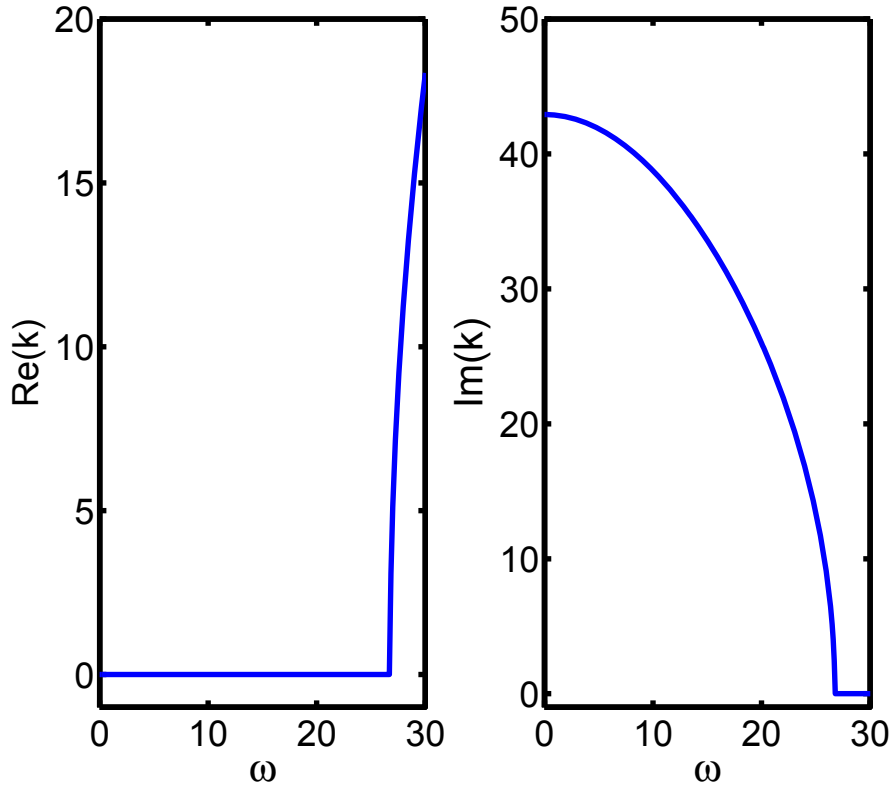


Figure 4.3: Plot of the dispersion relation for real (left) and imaginary (right) part of $k(\omega)$ with $\eta = 0$, $\omega_e = 0$, $\omega_h = 31.6$, $\tau = 0.05$ and $\omega \in [0, \frac{\pi}{2\tau}]$. The simulation results for the same case with $\omega_h = 31.6$ will be discussed in Section 4.5.4 and the corresponding Fig. 4.10 therein.

4.5 Benchmarking with Physical Processes

The numerical scheme described in the previous Sections 4.3 is implemented into the code H-VLPL. This section describes the key benchmark tests to evaluate accuracy and applicability of that scheme. First, we check the reflection, transmission and refraction of a laser pulse at hybrid plasma slabs of different densities. Second, we verify the validity of the energy conservation principle in the present algorithm. Third, we check the very well-known process of Target Normal Sheath Acceleration (TNSA) [35, 36]. Fourth, we benchmark plasma skin fields at very high hybrid densities when the spatial grid cell size is much larger than the plasma skin length (δ_s). Lastly, we check absorption of a circularly polarized Gaussian laser pulse over a long distance propagation in an underdense hybrid plasmas. Wherever possible, we compare the numerical results with the existing analytic solutions to establish the impeccability of H-VLPL.

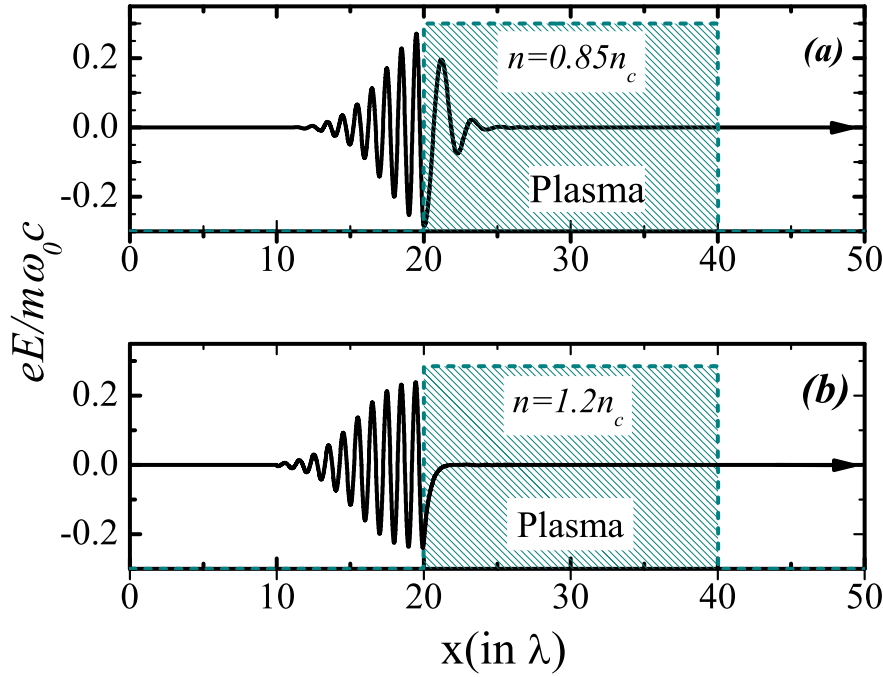


Figure 4.4: (a) Refraction of the incident laser pulse through the underdense ($n = 0.85n_c$) plasma (hybrid model) target. (b) Reflection through overdense ($n = 1.2n_c$) plasma (hybrid model) target.

4.5.1 Reflection and refraction of incident pulse

The first and the simplest test one can think of is the full reflection of the incident laser pulse from the surface of overdense plasma, as well as, transmission and reflection of the same when the plasma is underdense. In Fig. 4.4(a) a 30 fs Gaussian laser pulse propagates in the positive X direction towards an underdense ($n = 0.85n_c$) plasma slab. Here n_c is the critical plasma density for the laser wavelength $\lambda = 0.82\mu\text{m}$. At a time $T > 0$ a part of the incident laser pulse transmits through the plasma and a significant reflection also occurs. On the contrary, in Fig. 4.4(b) when a similar pulse is incident on an overdense plasma surface of density $n = 1.2n_c$ one observes a full reflection from the surface. It is essential to be mentioned here that in both the cases the plasma slabs have been treated with our new hybrid method, i.e., all the plasma particles in this particular simulation were “hybrid particles”, as described in Section 4.2.

4.5.2 Energy conservation

Another important point one would like to verify here, is the validity of the conservation of the total energy (E_{tot}) in the scheme. For this purpose, a test parameter sets with a very trivial laser pulse and plasma systems have been considered. It is important to note here that we treat the plasma with the hybrid algorithm as well as with the kinetic algorithm. The analytical equation for the total energy of the whole system can be

4.5. Benchmarking with Physical Processes

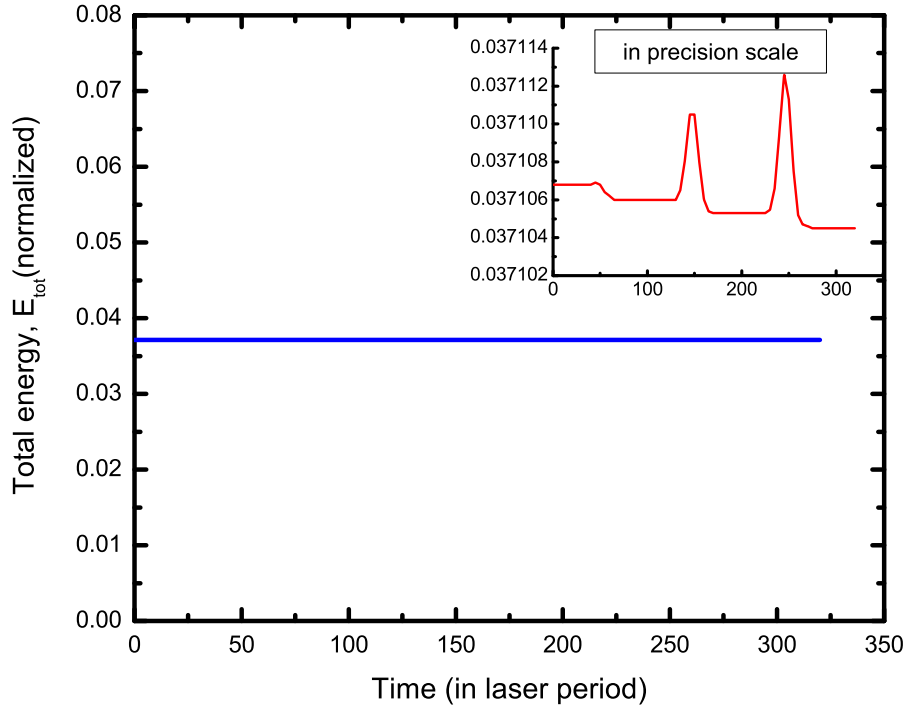


Figure 4.5: Total energy conservation in H-VLPL code. The total energy of the whole laser-plasma system has been plotted against laser period. The inset figure is drawn in precision scale of 10^{-6} for total energy E_{tot} with the same data set.

written as

$$E_{tot} = \sum_{\ell} m_{\ell} c^2 (\gamma - 1) + \frac{1}{8\pi} \int_V (E^2 + B^2) dV \quad (4.26)$$

where, m_{ℓ} are the masses of all sort of particles and $\gamma = \sqrt{1 + (p/m_{\ell}c)^2}$ is the relativistic γ factor. The fields are integrated over the whole simulation domain. One can summarize as $E_{tot} = E_{EM} + E_{part}$, where, E_{EM} and E_{part} are total electro-magnetic (EM) and particles' energy. The total particles' energy can be estimated as:

$$E_{part} = n_e (\gamma_e - 1) m_e c^2 + n_i (\gamma_i - 1) m_i c^2 + n_h (\gamma_h - 1) m_h c^2 \quad , \quad (4.27)$$

where, e , i and h represent electrons, ions and hybrids, respectively. Fig. 4.5 shows the total energy of the whole laser-plasma system in a closed boundary against time, measured in units of laser periods. The total energy E_{tot} remains constant nearly up to single precision round off error as it is seen in the inset in Fig. 4.5 over a significantly large time range. Hence, one can conclude that the total energy in this hybrid scheme is conserved as that of a conventional PIC scheme.

4.5.3 Acceleration of ions from a target back surface (TNSA)

Fig. 4.6 shows the physical model of the generation of ultra-intense energetic protons from laser-solid interactions, first described by Wilks *et al.* [35]. In the present case, the process has been examined with the new hybrid code H-VLPL. A 10 fs Gauss pulse propagating along the positive x - direction targeted to a $3.3 \mu\text{m}$ thin slab of plasma considered to be of three components: electrons, ions (protons with $m_i/m_e = 1836$) as well as hybrid particles. The density of the target increases to $2n_c$ over a ramp of $\sim 2 \mu\text{m}$. This is to model a good amount of preplasma essentially present in the real experiments. In the back surface, there is a thin layer of protons around 1/10th of a micron, where the density has been ramped from $2n_c$ to 0. In reality one can think of a sub-micron sized hydrogen layer pre-formed over the back surface of the target. The dense part of the target was modeled using the hybrid particles with the density $n_h = 1000n_c$ that would correspond to the solid density. The laser pulse used here has dimensionless amplitude $a_0 = eE/m\omega_0c = 2.0$, which corresponds to intensity of $5.5 \times 10^{18} \text{ Wcm}^{-2}$.

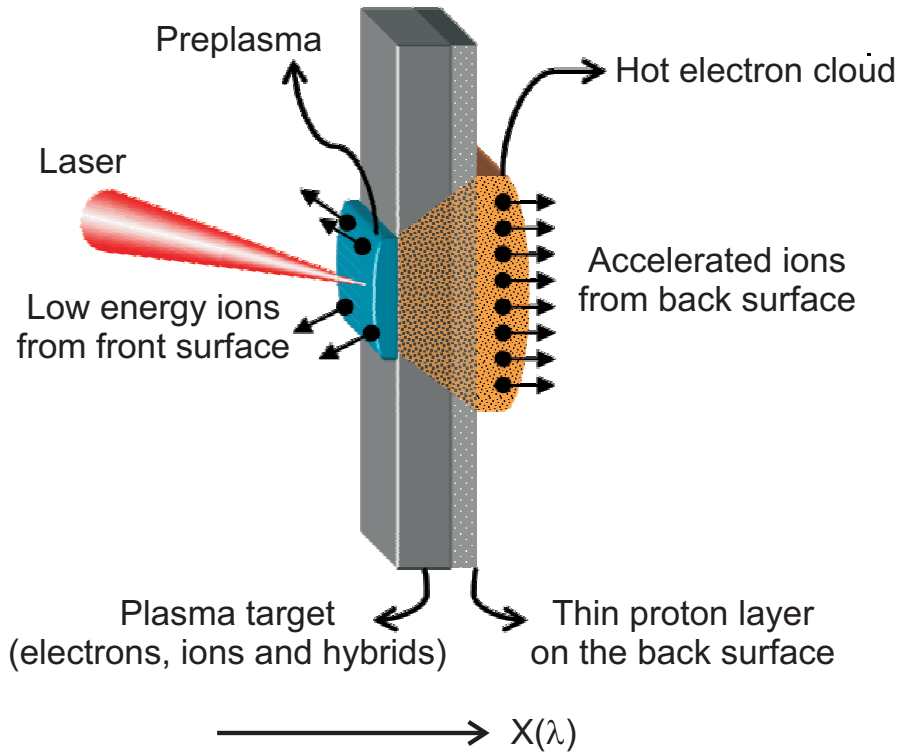


Figure 4.6: Physical model of the ion acceleration mechanism for a short and ultra-intense pulse interacting with thin target (TNSA).

The ultra-short laser pulse interacting with the target generates, in the blow off plasma region, a huge cloud of hot electrons, which propagates through the target and ionizes

4.5. Benchmarking with Physical Processes

the thin proton layer on the backward surface of the target. These generated protons are then knocked out of the surface by the electrostatic field of the hot electron cloud. Eventually, the ions are accelerated to high energies. In Fig. 4.7 the energy spectrum of the accelerated ions from the rear surface is graphed with the solid line. The maximum energy reached by these ions is around ~ 1 MeV, which is pretty remarkable energy with the intensity of laser used here.

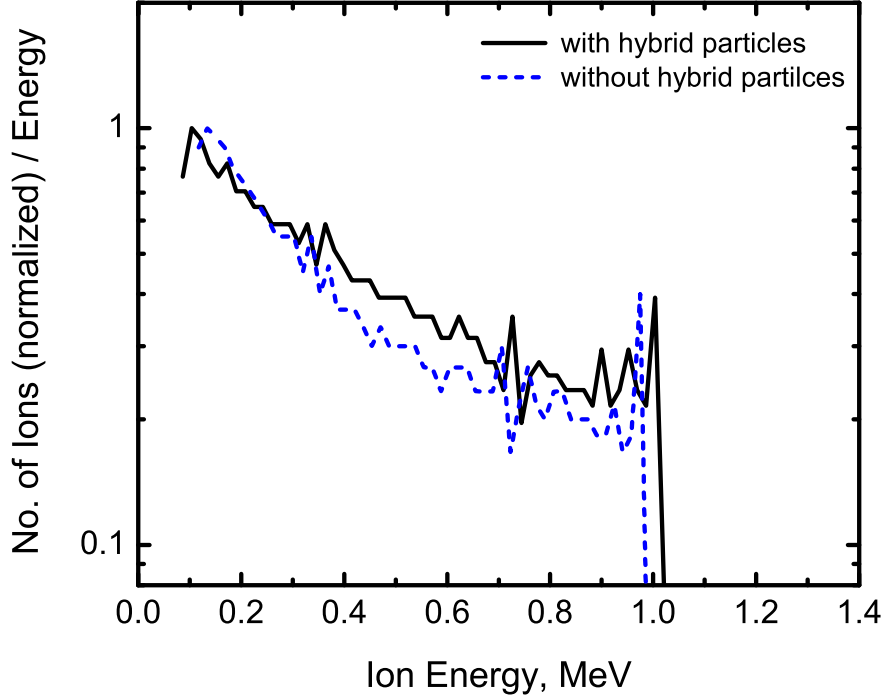


Figure 4.7: Energy spectrum of the accelerated ions from the rear surface of the target (solid line) as shown in Fig. 4.6 at a later time $T = \omega_0 t / 2\pi = 150$. Ions' kinetic energy is in MeV scale. The maximum kinetic energy of the ions is ~ 1 MeV. The broken line reproduces the similar ion spectrum in fully kinetic environment where no hybrid particles are present, at the same reference time.

At this point it is worthy to verify the kinetic nature of the code using a purely kinetic simulation i.e. without hybrid particles. The simulation with the same physical parameters has been performed without the hybrid particles and similar ion energy spectrum has been obtained with hybrid particles. This is compared with the hybrid scheme in Fig. 4.7.

Thus, one can be sure that the hybrid code can be used for computationally efficient studies of very high density plasmas, e.g., how to produce mono-energetic ion beams manipulating the thickness of the target as well as the hydrogen layer on the rear surface [163]. To get more insight into the mechanism of acceleration of ions, one can consider looking into the phase space of the hot electron cloud in Fig. 4.8.

The phase space of the hot electrons in Fig. 4.8 at an earlier time $T = \omega_0 t / 2\pi = 100$ (i. e. time in laser period) clearly shows that the cloud of hot electrons circulates inside

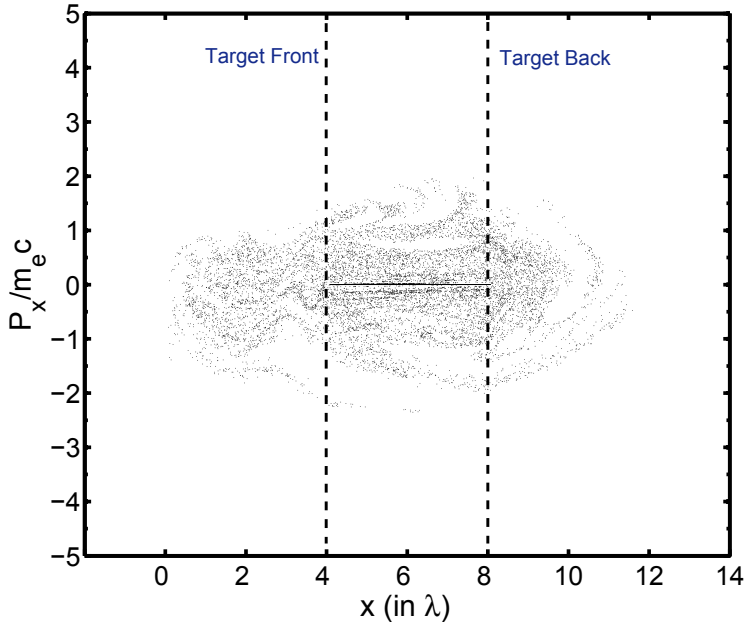


Figure 4.8: Phase space diagram of the hot electron cloud at an earlier time $T = \omega_0 t / 2\pi = 100$. Electron momenta are normalized to $m_e c$ and x axis in units of λ . The broken lines represent the plasma target front and back surfaces as that of the schematic of Fig. 4.6.

the target and pulls out the ions by significantly heating them in recursion. To get a good amount of acceleration, H-VLPL allows to take as much as 200 particles per cell for such kind of simulations. It is also anticipated to get little amount of low energy ions from the front surface, but compared to that from the rear surface they are colder.

It is proved that most of the accelerations of the ions from the rear surface occur in a short distance. This can also be verified with H-VLPL from the pattern of the accelerating fields of the back surface shown in Fig. 4.9. In this case this accelerating length is $\sim 4\mu m$ and this matches well with experimental and numerical findings observed so far.

At the end one can summarize as, the new hybrid approach of the code H-VLPL benchmarks efficiently well in detail the physics of generation of energetic ions from the target back surface.

4.5.4 Scaling of the skin fields

To proceed further in benchmarking H-VLPL one can scale the fields at the skin depth (E_s) to the reflected (or incident) fields (E_i). For the present case we choose a range of highly overdense plasmas of densities $n = 10, 100$ and $1000n_c$ with sharp boundaries. The incident laser is a circularly polarized Gaussian pulse of the dimensionless amplitude $a_0 = 0.2$. Its duration is 10fs. These parameters are chosen to avoid relativistic non-

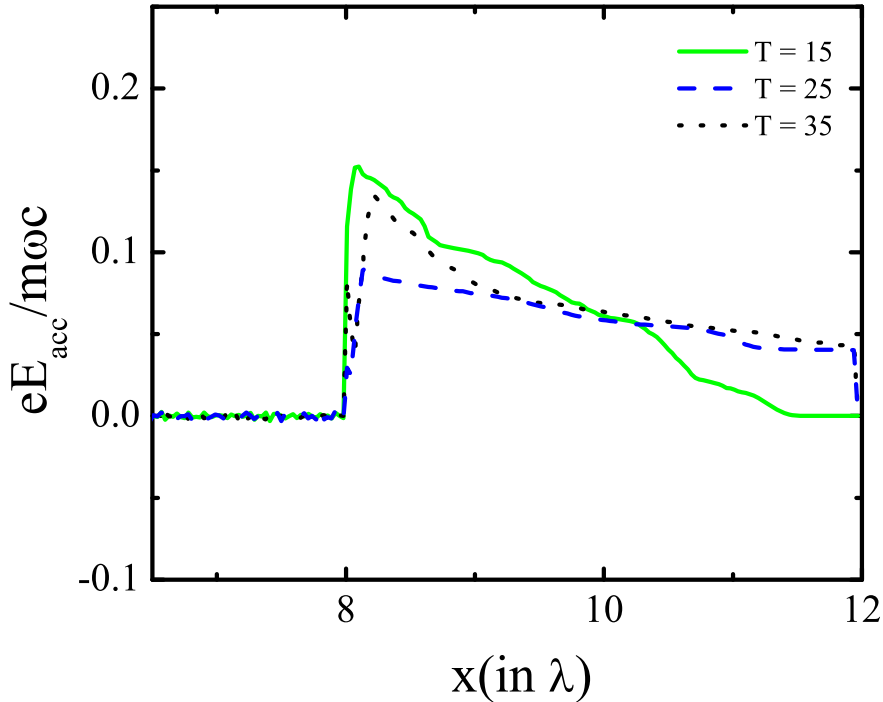


Figure 4.9: The accelerating electric fields, at three different earlier times $T = \omega_0 t / 2\pi = 15, 25$ and 35.

linearities occurring during the interactions.

To benchmark the code we record the laser field at the plasma surface. According to the linear theory, the field E_s at the surface of a highly overdense plasma, $n_e \gg n_c$, relates to the field of the incident laser E_i as

$$\frac{E_s^2}{E_i^2} = \frac{4n_c}{n_e} \quad (4.28)$$

where we have neglected the absorption.

Fig. 4.10(a) shows the squared ratio of the field, E_s^2/E_i^2 as a function of the normalized plasma density $n = n_e/n_c$. The numerical results obtained from the H-VLPL code matches well with the analytical result (4.28).

On the other hand, we know that the laser fields must decay exponentially in the overdense plasma layer. Analytically, the electromagnetic field intensity decays as

$$\ln I = -\frac{2x}{\delta_s}, \quad (4.29)$$

where $\delta_s = c/\omega_p$ is the skin depth. We have measured the field decay in the H-VLPL simulations and plotted them in Fig. 4.10(b). One gets excellent agreement with the analytical expressions for the skin length even for the highest densities.

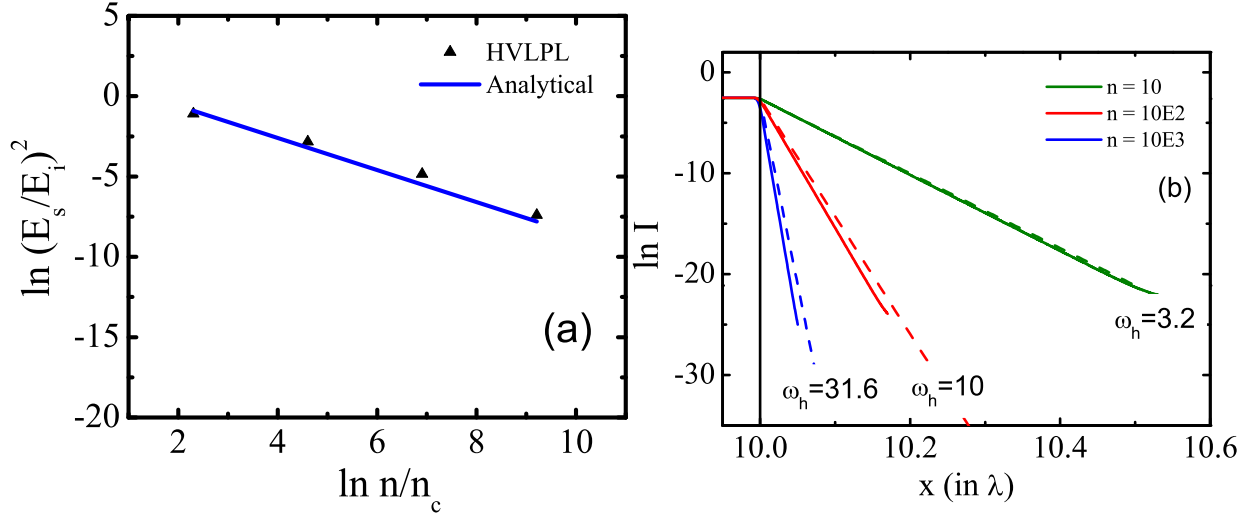


Figure 4.10: Scaling of the skin fields using H-VLPL. (a) Logarithm of skin fields plotted for four different hybrid densities. The fields are normalized as $eE/m\omega_0c$ and density to n_c . The solid line shows the analytical results for the same. (b) Logarithm of skin field intensities for three different hybrid densities. The analytically calculated values of ω_p are also provided for each density for comparison. The dashed lines show the analytical results for the corresponding densities. The dispersion relation for $\omega_h = 31.6$ has been discussed in Fig. 4.3.

For the density $n_e = 1000n_c$, one finds the skin length $\delta_s/\lambda = 0.005$. It is worth mentioning that this simulation has been done with the grid cell size $h_x/\lambda = 0.05$, i.e., the grid step was much larger than the skin length, $h_x = 10\delta_s$. Yet, the field decay in plasma is accurately described.

4.5.5 Collisional absorption

We have introduced the effects of collisional absorption into the implicit hybrid scheme of H-VLPL. This makes the code versatile enough to handle extremely high density warm plasmas where electron-ion binary collisions cannot be neglected. However, to test the accuracy of the collisional scheme we have chosen laser pulse absorption as it propagates in underdense plasma. This is because there is a known analytic solution for the laser dynamics to compare with.

Fig. 4.11 shows the change in laser amplitude as it propagates through a collisional underdense plasma of density $n = 0.04n_c$. The laser pulse is chosen to be weakly relativistic, $a_0 = 0.2$, and relatively long Gaussian pulse of 50fs duration. The longer duration is selected to avoid dispersion effects. The collisional frequency ν_{ei} (described as η in Section 4.2) is 0.5. We calculated the logarithmic field amplitudes at various propagation lengths, x from H-VLPL and compare the results with the analytical solution

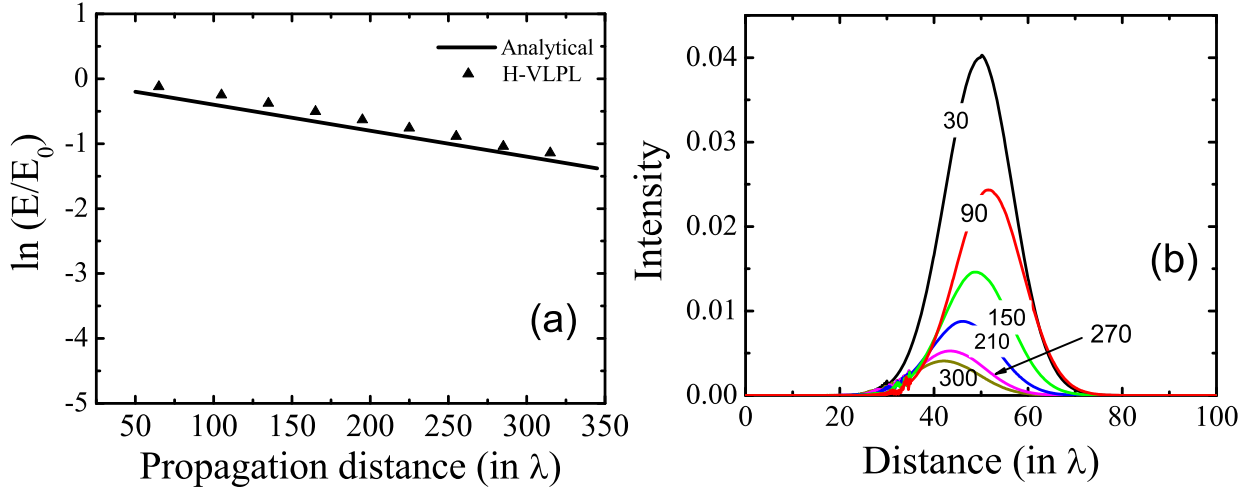


Figure 4.11: Benchmarking of collisional absorption using H-VLPL: (a) Logarithm damping of laser amplitude E/E_0 along the propagation direction and comparison with the analytical results (b) Damping of incident laser intensity over time; all the times are in scale of laser periods.

$$\ln\left(\frac{E}{E_0}\right) = \text{Re}[-i\omega t + ikx - \Delta x], \quad (4.30)$$

where,

$$\Delta \approx \frac{1}{2} \frac{\omega_p^2(\nu_{ei}/\omega)}{(\omega^2 - \omega_p^2)^{1/2}}$$

is the collisional absorption rate. The simulation results gives an exponentially decreasing laser field E/E_0 inside the bulk plasma as it propagates along. These results are shown in Fig. 4.11(a). Also, the gradually decreasing peak intensity over laser propagation time (in laser period) in Fig. 4.11(b) confirms the effect of collisional absorption in agreement with the analytic solution (4.30).

4.6 Conclusions and Outlook

In conclusion, we have presented a new one-dimensional full electromagnetic implicit hybrid algorithm that allows to simulate laser-plasma interactions at arbitrary plasma densities via automatic reduction of the highest plasma frequencies down to numerically stable range. In this case full kinetic particle-in-cell (PIC) and hydrodynamic model have been combined in the single hybrid plasma code. It avoids the limitation on the time step present in explicit PIC codes. The numerical scheme is analyzed, its dispersion

4. Implicit PIC-Hydrodynamic Hybrid Simulation Code H-VLPL

relation is derived, and a numerically efficient matrix algorithm for solving the implicit system of equations is presented.

The scheme is tested on a series of physically important examples. It is shown that the spatial field structure in the highly overdense plasma is well described by the code H-VLPL even when the grid step size is much larger than the plasma skin length.

In addition to this, we must mention here that one can extend this scheme considering the hybrid ion momenta dynamics according to:

$$\frac{d\vec{p}_h^{ion}}{dt} = -\frac{q_e}{m_i} \frac{\vec{v}_h}{c} \times \vec{B}, \quad (4.31)$$

i.e., the ponderomotive or magnetic force will act directly on the hybrid ions. Yet, we leave this to a further extension of the H-VLPL code. At present, the hybrid particles are purely current carriers. Moreover, the presented scheme is one-dimensional. The next step will be to generalize this hybrid algorithm to the full three-dimensional geometry.

5 Effects of Temperature and Collisions on the Weibel Instability

5.1 Introduction

The fast ignition fusion (FI) is a promising route towards the laser driven fusion. In the FI scheme, a laser-generated relativistic electron beam with a few MeV per electron energy must propagate through over-dense plasma to heat a hot spot in the core of a pre-compressed fusion fuel target [48]. The current carried by these MeV electrons inside the plasma is much higher than the Alfvén current limit $I = (mc^3/e)\gamma = 17\gamma \text{ kA}$, where m is the electron mass, e is the electronic charge, and γ is the Lorentz factor of the beam. Clearly, the transportation of this electron beam is not possible unless it is compensated by a return plasma current, thus maintaining the global charge neutrality. However, this configuration is unstable and the current beam is susceptible to the Weibel and the two-stream instabilities. The Weibel instability [49] is particularly responsible for the generation of very strong magnetic fields ($\sim 100 \text{ MG}$). It is one of the leading instabilities under relativistic conditions not only in laser plasma interaction [105], but also in the Universe [75]. It has been a subject of research for a long time [106–119]. Yoon *et al.* [112] have developed a kinetic formalism of the Weibel instability in the context of charged particle beam transport in accelerator physics. Recently various theoretical models, both kinetic and hydrodynamic ones, have been developed to study this instability in linear regime [113–115]. Honda *et al.* [116] have studied the collective stopping of the beam and ion heating in the context of FI. Three-dimensional simulations of resistive beam filamentation corresponding to the full scale FI configuration have been performed by Honrubia *et al.* [117]. Three-dimensional magnetic structures generated due to the Weibel instability in a collisionless plasma have also been reported [118]. Recently, the evidence of Weibel-like dynamics and the resultant filamentation of electron beams have been reported experimentally [108–110].

In this chapter, we will discuss about the 2D and 3D Particle-in-Cell (PIC) simulations of a relativistic electron beam transport in overdense plasmas in two geometrical planes, transverse to the beam propagation direction and in the plane containing the propagating beam (longitudinal geometry). We study the effects of the background plasma collisions and beam temperature on the beam transportation separately as well as collectively. These two different geometries are chosen because in transverse geometry the coupling of the Weibel instability (WI) with the two-stream instability (TSI) does

5. Effects of Temperature and Collisions on the Weibel Instability

not occur whereas, the longitudinal geometry is appropriate to study the coupling of WI and TSI. In the case of transverse geometry we are able to separate the effects of temperature and collisions and study them individually and collectively. On the other hand, in longitudinal geometry additionally the effects of collisions and beam temperature are studied. The beam transportation in these simulation geometries has been studied in four different cases (collisionless, collisional, thermal and collisional) thus highlighting the influence of these physical processes precisely and distinctly. The simulation results show that the Weibel instability can not be suppressed by thermal effects only, if small collisions are present in the background plasma. Moreover, in the coupled Weibel–two-stream instability, collisional effects initiate the generation of longitudinal magnetic field, which is suppressed in collisionless case. An analytical model has also been developed, which is used to compare the growth rates in the linear stage of the instability in the transverse geometry. We have performed further full 3D simulations which also include the coupling of these instabilities. These will be presented here briefly.

5.2 Different Simulation Geometries

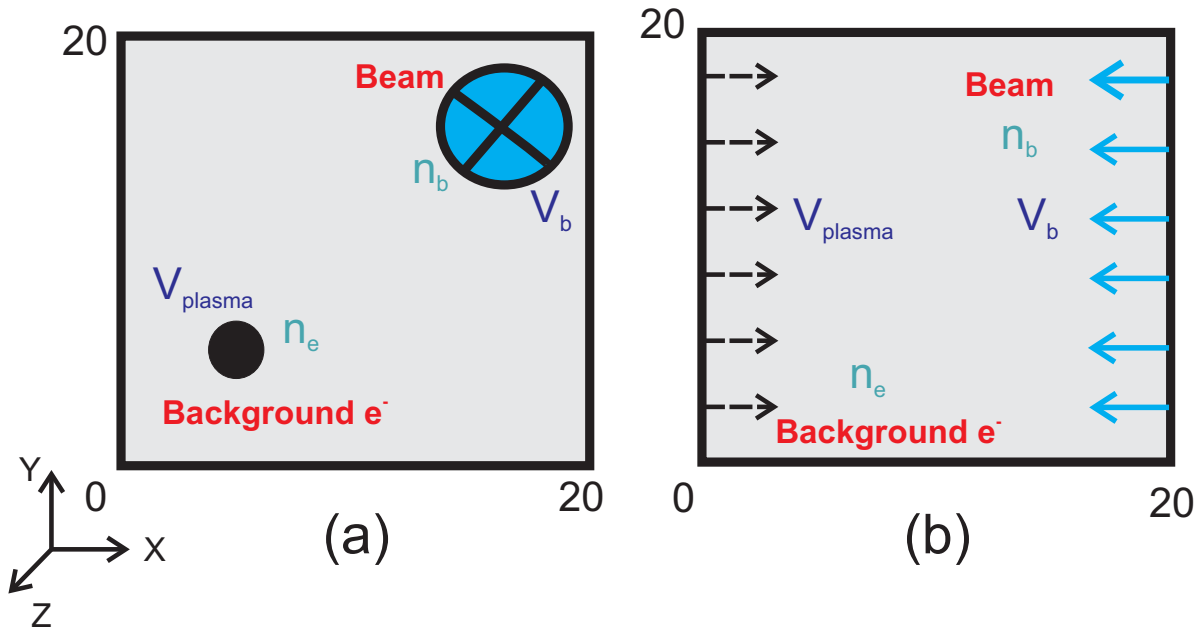


Figure 5.1: Schematic of the geometries of the 2D-Simulation Model. The axes dimensions are in units of skin depth λ_s (a) Transverse simulation geometry : the relativistic beam is propagating along the negative Z -direction and the plane of simulation is transverse to the beam propagation. (b) Longitudinal simulation geometry : the relativistic beam is propagating along negative X -direction and the simulation plane contains the propagating beam. The beam plasma density ratio is $n_b/n_p = 9$.

Figure. 5.1 shows the schematics of the two 2D simulation geometries. A 3D simulation geometry has also been shown in Fig.5.2. In Fig. 5.1(a) the electron beam propagates

5.2. Different Simulation Geometries

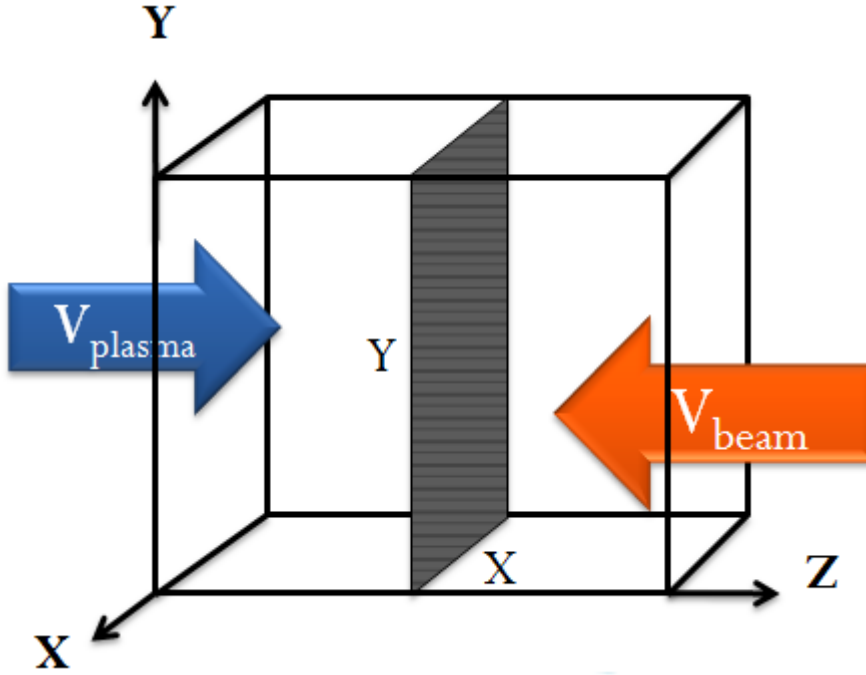


Figure 5.2: Schematic of the geometry of the 3D-Simulation Model. The axes dimensions are in units of skin depth $\lambda_s = c/\omega_{pe}$. The relativistic beam is propagating along the negative Z -direction whereas the plasma electrons have velocities along positive X direction. The beam plasma density ratio is $n_b/n_p = 9$. The intersecting plane demonstrates how the 2D transverse geometry has been constructed in the (X, Y) simulation domain.

in the negative Z -direction with the relativistic velocity $v_{(b,z)} \gg v_{(b,x)}, v_{(b,y)}$. The bulk cold background plasma is represented only by ambient plasma electrons, while the plasma ions are considered as a fixed charge-neutralizing background with the density $n_0 = n_b + n_p$. In Fig. 5.1(a), \mathbf{v}_b is into the plane and return plasma current is out of the plane. The plasma electrons are moving opposite to the beam electrons with the velocity \mathbf{v}_p . In Fig. 5.1(b) the electron beam propagates along the negative X -direction with relativistic velocity $v_{(b,x)} \gg v_{(b,y)}, v_{(b,z)}$ i.e. the plane of simulation is containing the propagating beam. In this geometry the beam velocity \mathbf{v}_b is along negative X -direction and return plasma current is directed the positive X -axis. Similar to Fig. 5.1(a), the plasma electrons are moving opposite to the beam electrons with the velocity \mathbf{v}_p , where $\mathbf{v}_p \ll \mathbf{v}_b$. The beam density is much smaller than the background plasma electron density, i.e. $n_b \gg n_p$, which is a usual situation in the FI scheme. It may be noted here that the ambient plasma ions are considered to be fixed neutralizing background with density $n_0 = n_b + n_p$. In case of the full 3D geometry in Fig.5.2 the simulation domain is three dimensional (X, Y, Z) and the electron beam propagates along the negative z -axis. Similar to the 2D geometries the plasma electrons have a velocity opposite to the beam velocity. All the other parameters are same as in the 2D simulation models. The spatial dimensions of the simulation domain L is large in comparison with the

electron skin depth *i.e.* $L \gg \lambda_s$, where $\lambda_s = c/\omega_{pe}$, where c and ω_{pe} are the velocity of light in vacuum and electron plasma frequency respectively. The quasi-neutrality is maintained overall as the field evolutions due to the Weibel instability occurs on a time scale slower than the plasma electron frequency $\Delta t \gg 1/\omega_{pe}$. The collisional processes are simulated with a newly implemented collision module in the relativistic PIC code Virtual Laser Plasma Laboratory (VLPL) [95].

5.3 Details of the PIC Simulation Parameters

The simulation plane, which is transverse to the plane of propagation of the e -beam or containing the propagating beam, is of dimensions, $X \times Y = (20 \lambda_s \times 20 \lambda_s)$ sampled with a mesh of 160×160 cells. All simulations are performed with 64 particles per cell and with a grid size much smaller than the skin depth $\delta x = \delta y = 0.02 \lambda_s$. The density ratio between the beam and plasma electrons is $n_p/n_b = 9$, whereas the beam and the background plasma electrons have velocities $v_b = 0.9 c$ and $v_p = 0.1 c$. The evolution of the bulk Weibel E and B fields are measured in every diagnostic step summed over all the particles (N_p) as

$$\int_S E_{\text{weibel}}^2 dx dy = \sum_{N_p} \left(\frac{e\varepsilon}{m_e c \omega_{pe}} \right)^2 N_x N_y, \quad (5.1)$$

where, N_x and N_y are the number of x and y cells and $e\varepsilon/m_e c \omega_{pe}$ represents the field normalization. We will discuss in 5.4.3 about the measurement of fields in full 3D simulations. The electron beam has a temperature of $T_b \approx 70$ keV and the ambient plasma collision frequency is $\nu_{ei}/\omega_{pe} = 0.15$ used for these simulations. In all simulations, always the background plasma is cold while beam electrons do not face any collisions. It might be worthwhile to note here that the background electron ion collisions are purely binary collisions implemented with a widely used stochastic collision algorithm.

5.4 Simulation Results

5.4.1 Transverse geometry

In Fig. 5.3, the snapshots of transverse E and B fields, and the structure of the beam filaments are shown at the time, $T = 20(2\pi/\omega_{pe})$ for four different cases, (a) cold electron beam and collisionless background plasma, (b) cold electron beam and collisional plasma (c) hot electron beam and collisionless plasma and (d) hot electron beam and collisional background plasma. The beam density filamentation is shown in the last column in each panel. To get more insight into the field evolution and filament merging process a set of figures Fig. 5.4, 5.5 and 5.6 for four different simulation cases in the transverse geometry has been produced here. Every figure shows snapshots of the growing of the Weibel \mathbf{E} and \mathbf{B} and merging of the filaments chronologically. This gives a clear understanding of the whole scenario. Now we proceed with the explanation of the

5.4. Simulation Results

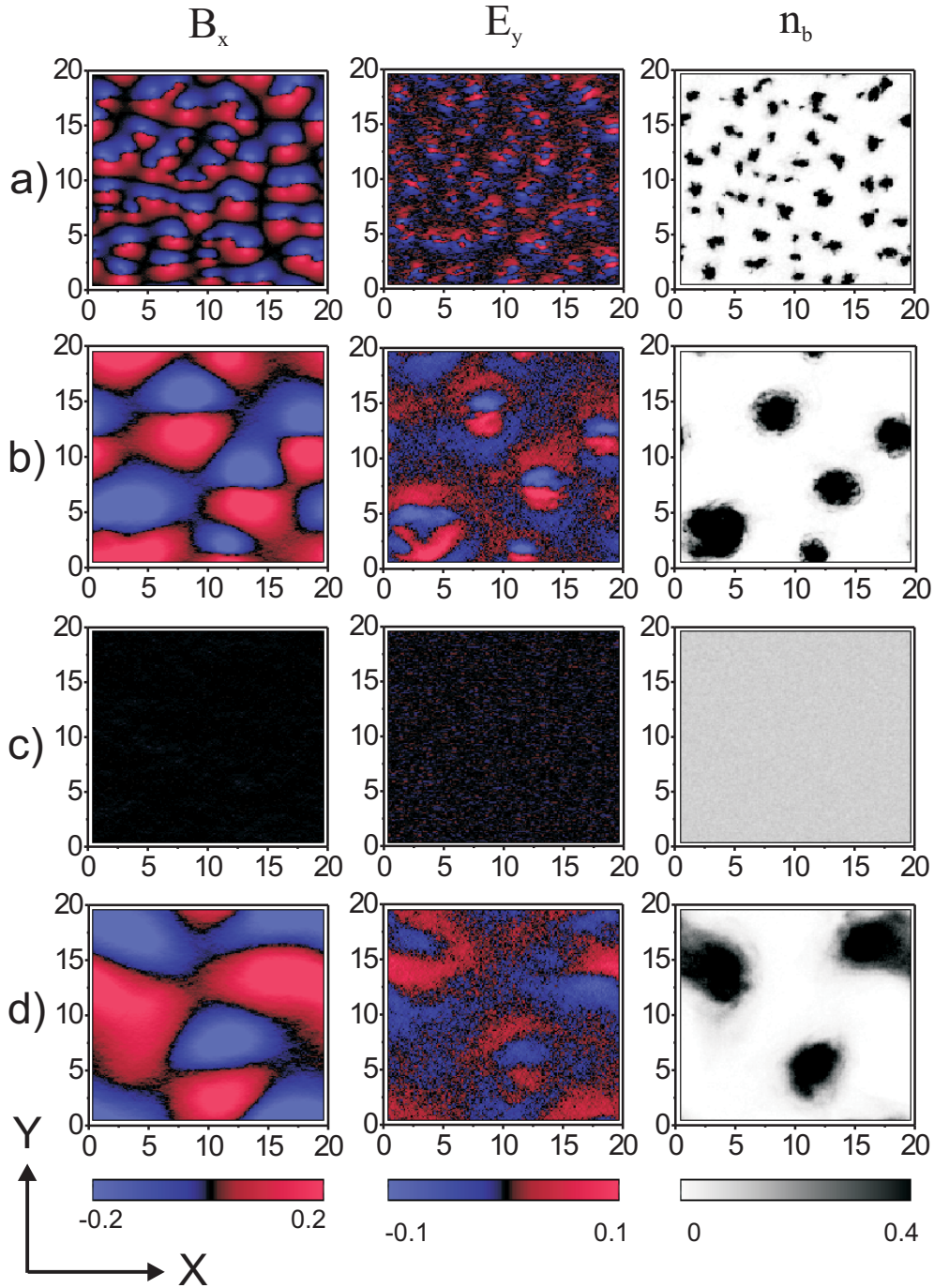


Figure 5.3: Snapshots of the the evolution of transverse electromagnetic Weibel fields (E_y and B_x) and beam filament densities (n_b) in transverse geometry during the nonlinear stage at a time $T = 20(2\pi/\omega_{pe})$ for comparing four different simulation cases: (a) Cold electron beam in a collisionless background plasma, (b) cold e -beam in a collisional background plasma and (c) hot electron beam in a collisionless background plasma and (d) hot electron beam in a collisional background plasma. The time is in units of $2\pi/\omega_{pe}$ and the \mathbf{E} and \mathbf{B} fields are normalized as $eE/m_e c \omega_{pe}$ and $eB/m_e c \omega_{pe}$.

5. Effects of Temperature and Collisions on the Weibel Instability

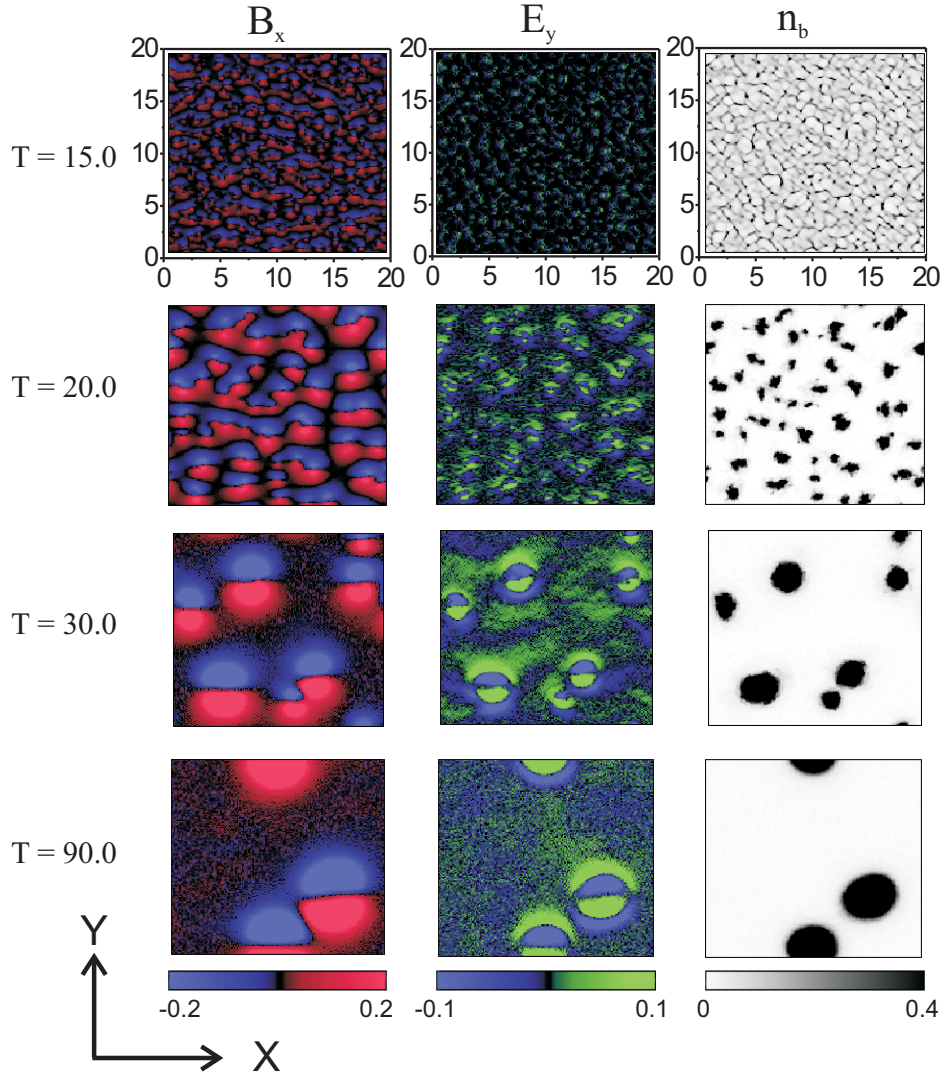


Figure 5.4: Snapshots of the temporal evolution of transverse electromagnetic Weibel fields (E_y and B_x) and beam filaments in transverse geometry in the simulation case (a) i.e. cold electron beam in a collisionless background plasma. The time scale and the \mathbf{E} and \mathbf{B} fields are normalized as explained in Fig. 5.3.

Fig. 5.3 once again. In the collisionless case (a), the filaments are small, comparable with the background plasma electron skin depth. In the collisional case (b), the filament size is bigger. This can be explained as a collisional diffusion of plasma electrons across the self-generated magnetic fields. Further, collisions in the system tend to reduce anisotropy there by reducing the available free energy responsible for the growth of the instability. Hence, we may expect a lower build up of field energies than in the previous case in the presence of collisions, which is also seen in the simulation results. In the third panel of the figure, simulation case (c), the electron beam is hot with the transverse temperature $T_b \sim 70$ keV, and the background plasma electrons are collisionless. Here we see no filament formation. The temperature of the electron beam stabilizes the

5.4. Simulation Results

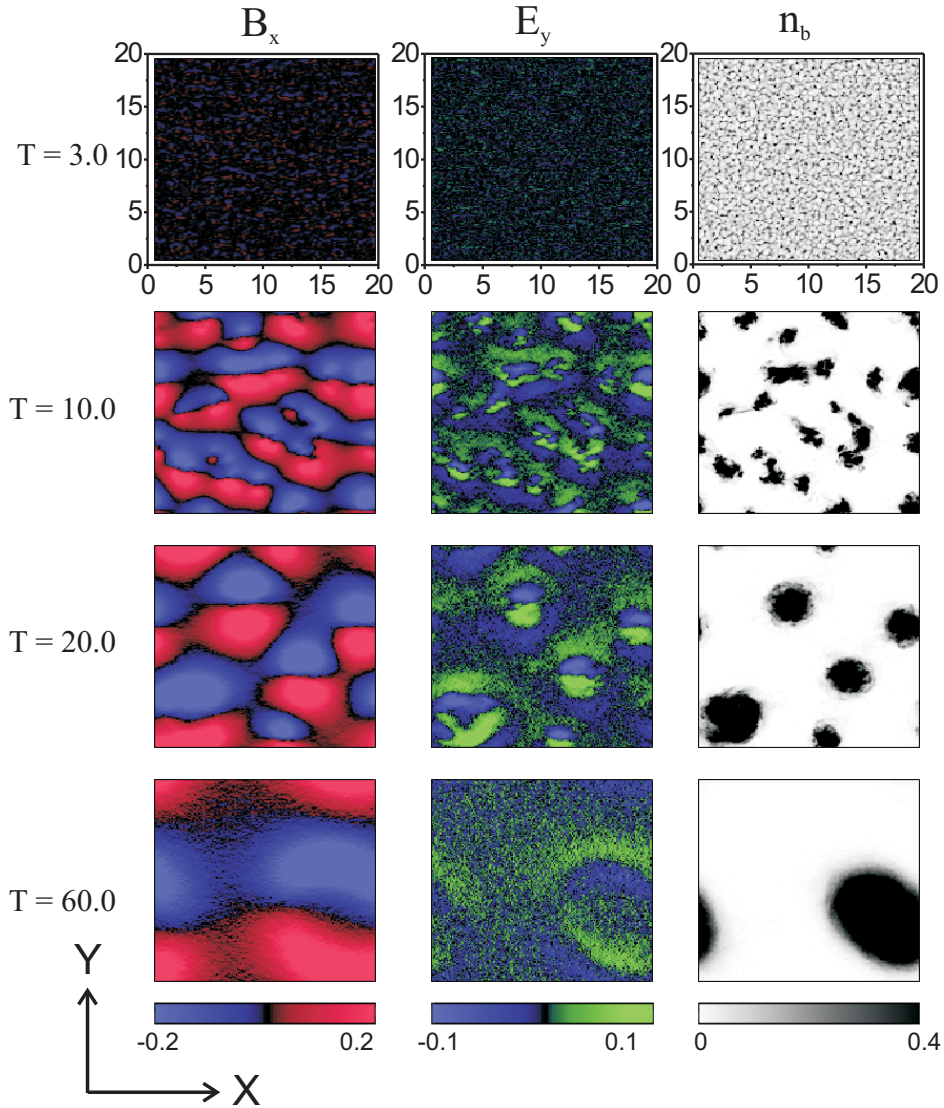


Figure 5.5: Snapshots of temporal evolution of transverse electromagnetic Weibel fields (E_y and B_x) and beam filaments in transverse geometry in the simulation case (b) i.e. cold e -beam in a collisional background plasma. The time scale and the \mathbf{E} and \mathbf{B} fields are normalized as explained in Fig. 5.3.

Weibel instability. Physically the thermal pressure of the electron beam prevails over the magnetic pressure in this case. Hence, the magnetic field pinching which actually drives the instability does not occur resulting in the suppression of the Weibel instability. We wish to state here that in the longitudinal geometry (explained in 5.4.2) and the full 3D geometry, the configuration would still be unstable due to coupling with the electrostatic two-stream instability, which may be considered as a source of “effective collisionality” in plasmas. The last panel of the figure depicts the filament formation in the simulation case (d), where the electron beam is hot and the plasma is collisional. One remarkable result is that although the beam temperature is the same as in the

5. Effects of Temperature and Collisions on the Weibel Instability

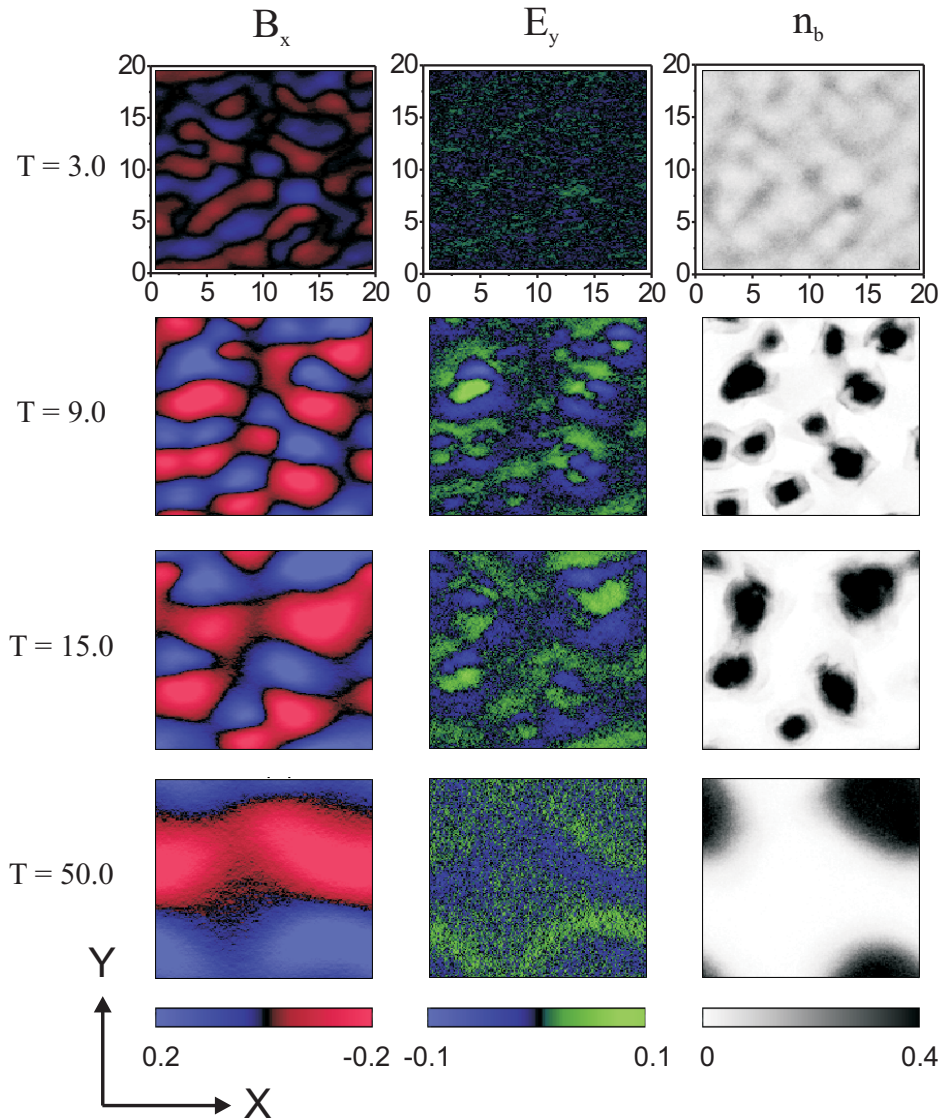


Figure 5.6: Snapshots of temporal evolution of transverse electromagnetic Weibel fields (E_y and B_x) and beam filaments in transverse geometry in the simulation case (d) i.e. hot electron beam in a collisional background plasma. The time scale and the \mathbf{E} and \mathbf{B} fields are normalized as explained in Fig. 5.3.

stable collisionless case (c), the background plasma collisions revive back the instability. The role played by the collisions here is somewhat paradoxical as one might expect that the collective effects of both collisions and temperature must kill the instability. Yet, quite opposite is the case. This paradox could be explained on the basis of instability caused by collisions in plasmas carrying negative energy waves. This is discussed later in this chapter. The message of our work is that the complete suppression of the Weibel instability in the context of FI of Inertial Confinement Fusion targets can be difficult as even small collisions in the background plasma tend to revive the instability.

Fig.5.7 shows the evolution of electric and magnetic field energies in the four cases

5.4. Simulation Results

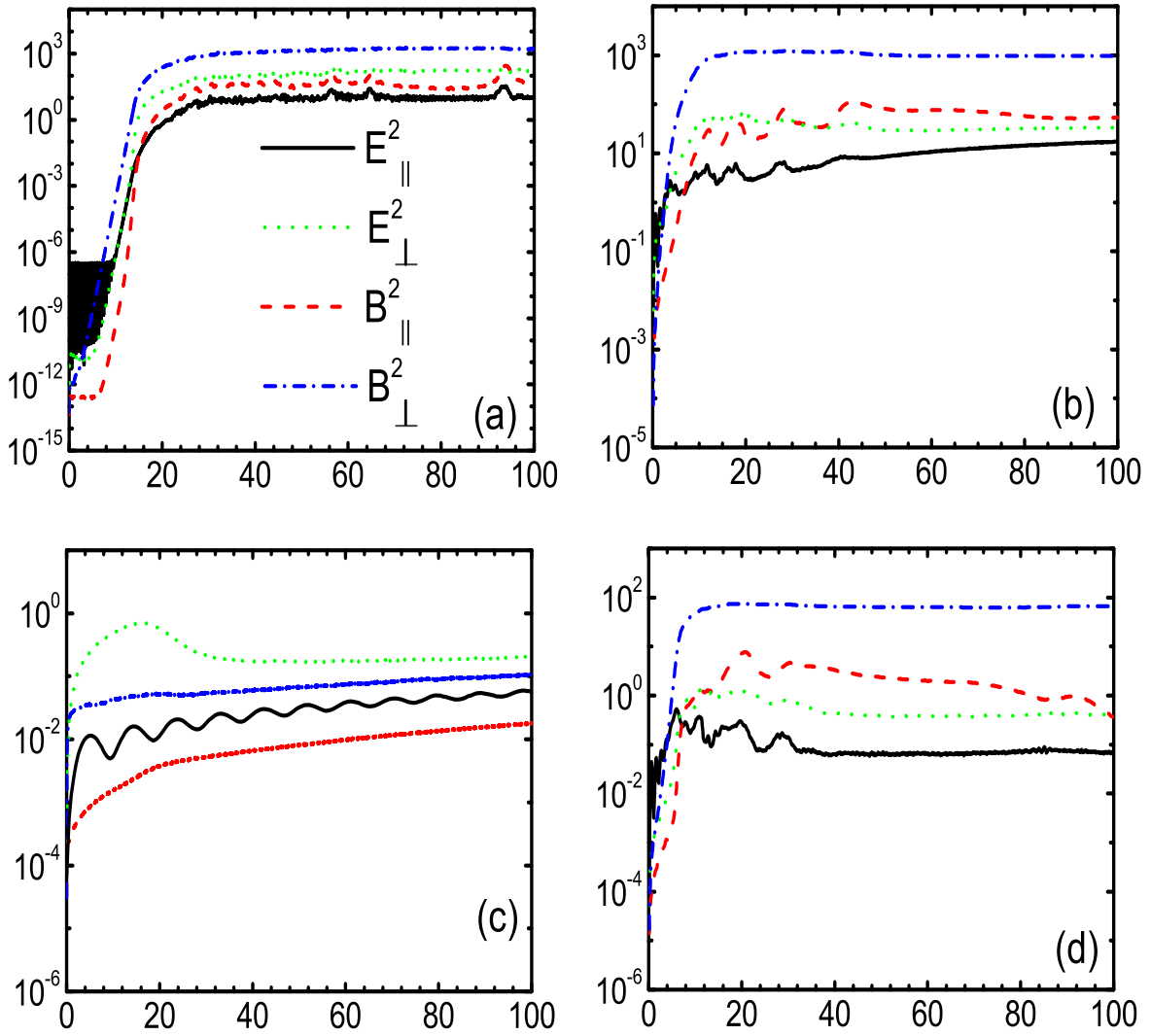


Figure 5.7: Time evolution of the transverse and longitudinal Weibel \mathbf{E} and \mathbf{B} field energies (E_{\perp}^2 , $B_{\perp}^2, E_{\parallel}^2, B_{\parallel}^2$) for the transverse geometry for four different simulation cases as described in the previous Fig. 5.3. The horizontal axes represents the time in units of $(2\pi/\omega_{pe})$ and the vertical axes represents the field energies, normalized as described in Eq. (5.1).

corresponding to the simulations in Fig.5.3. The energy axes in Fig.5.7 use logarithmic scales. We see a stage of linear instability, where the field energies build up exponentially in time. It is followed by a nonlinear saturation. The linear instability stage is present in the simulations (a), (b) and (d). The simulation (c), where the electron beam had high temperature and the background plasma was collisionless, shows no linear instability and no significant build up of the magnetic field energy. This is in compliance with the results of Fig.5.3. After the linear stage of the instability, filaments start merging into each other due to the magnetic attraction and the field energies saturate. Some small fluctuations around the saturated field energies can be seen. A magnified look into these

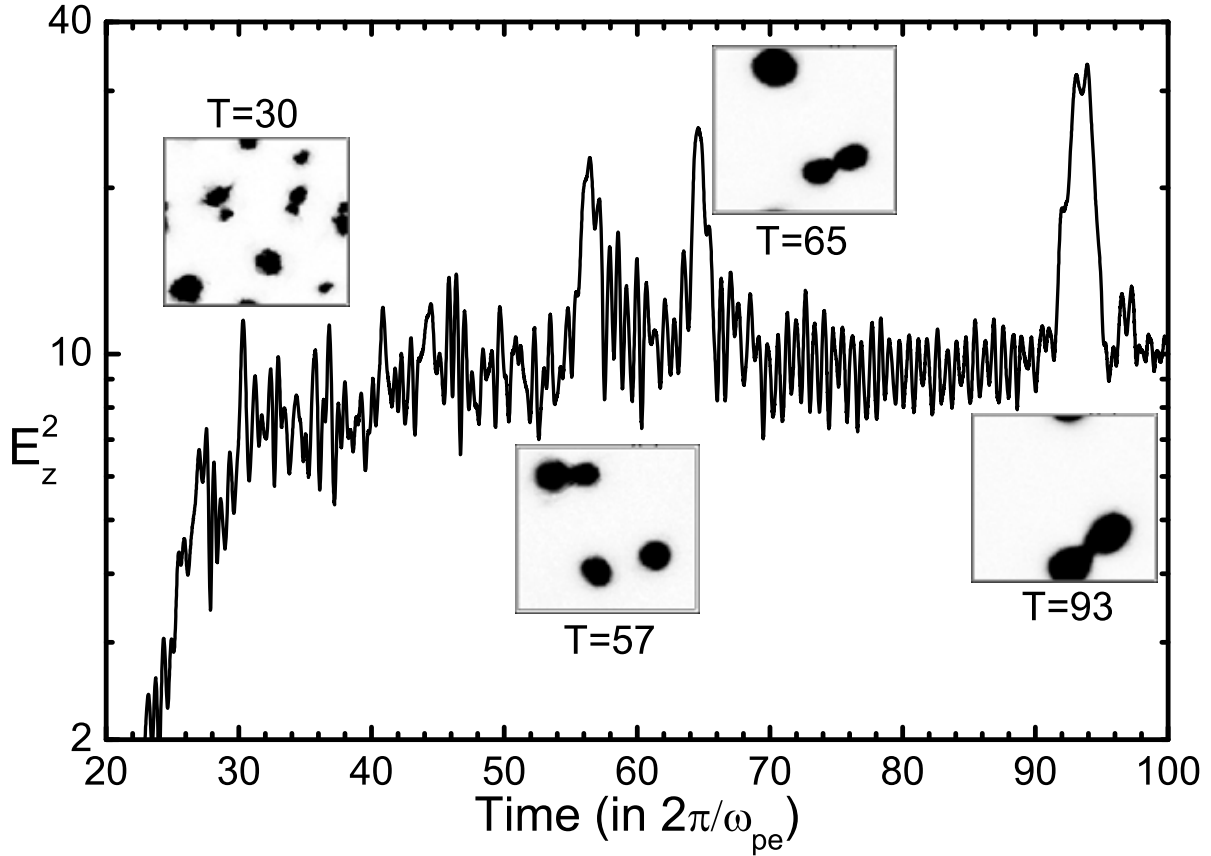


Figure 5.8: Fluctuations in the longitudinal electric field E_{\parallel}^2 corresponding to collective merging over time of the Weibel filaments in the saturation regime. The figures inset shows the merging of the filaments corresponding to the fluctuation at that time.

fluctuations in the longitudinal field E_{\parallel}^2 corresponding to the the collective merging of the Weibel filaments in the saturation regime is shown in Fig. 5.8. We observe a surge in the E_z field whenever the filaments merge together. The merging of bigger filaments produces very large fluctuation in the filed. These fluctuations occur due to the collective merging of the filaments as also discussed Honda *et al.* [116].

5.4.2 Longitudinal geometry

Snapshots of transverse E and B fields, and the structure of the beam filaments for longitudinal geometry are shown in Fig. 5.9 for all the four different cases as we studied in case of transverse geometry in 5.4.1. The beam density filamentation is shown in the extreme right column in each panel. The filament pattern differs significantly in this case due to the presence of coupled instabilities. The filamentation process constructs pipe like structures and the beam electrons get diffused when the fields get saturated. In the collisionless case (a), filamentation occurs at a slower rate and the fields reach saturation at larger times than the other three cases. Hence, the snapshots for the case

5.4. Simulation Results

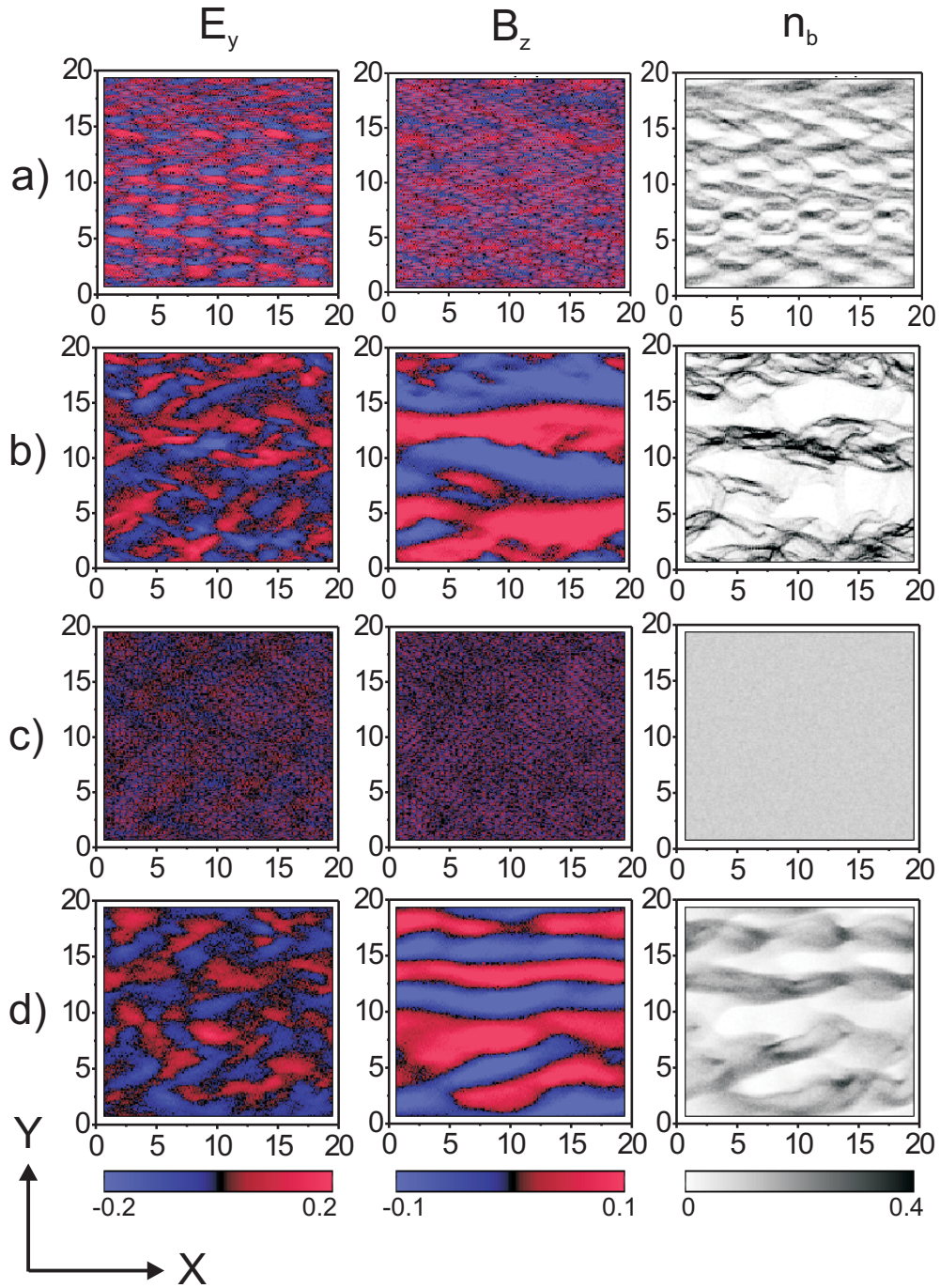


Figure 5.9: Snapshots of the the evolution of transverse electromagnetic Weibel fields (E_y and B_z) and beam filament densities (n_b) in longitudinal geometry during the nonlinear regime for four different simulation cases as described in Fig. 5.3 for transverse geometry. The top most panel i.e. in case (a), is taken at a time $T = 15(2\pi/\omega_p)$ and the other three at $T = 8(2\pi/\omega_p)$. The time scale and the \mathbf{E} and \mathbf{B} fields are normalized as explained in Fig. 5.3.

5. Effects of Temperature and Collisions on the Weibel Instability

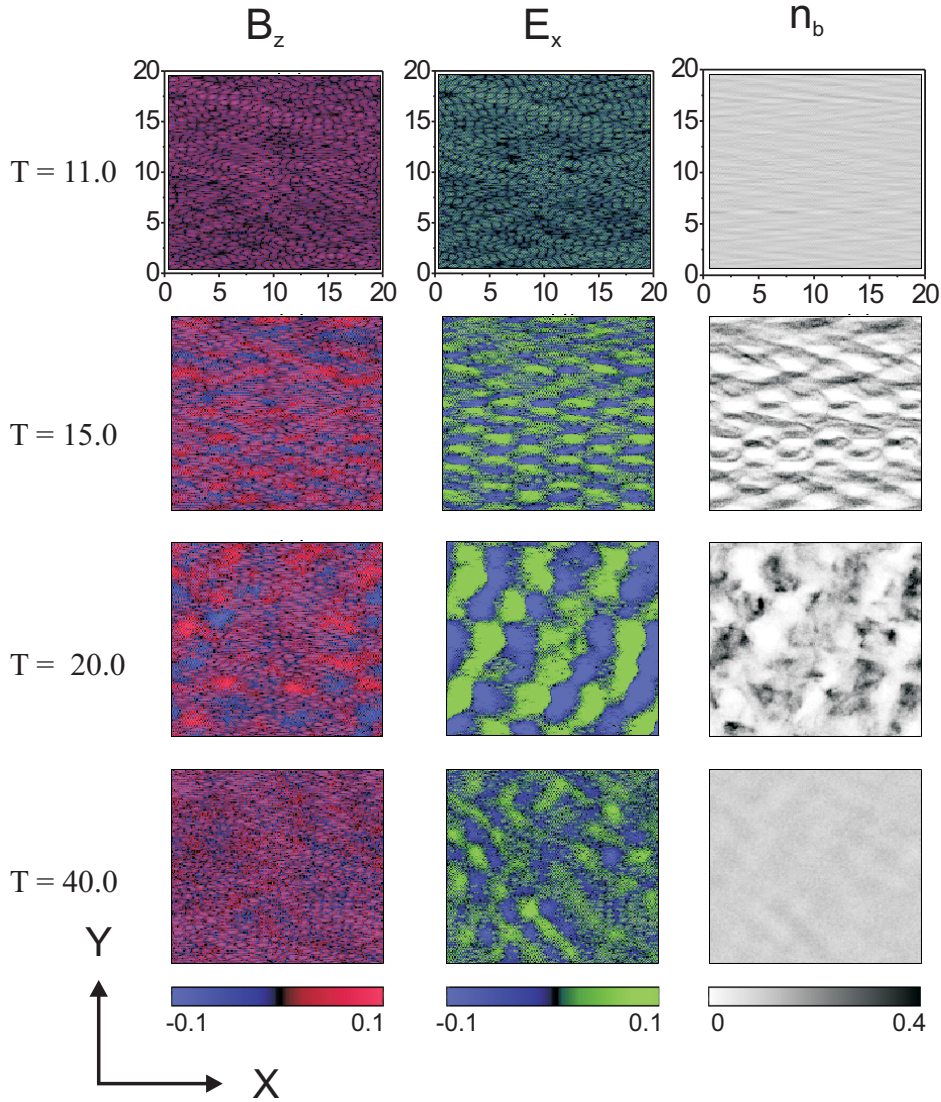


Figure 5.10: Snapshots of the temporal evolution of transverse electromagnetic Weibel fields (E_y and B_x) and beam filaments in longitudinal geometry in the simulation case (a) i.e. cold electron beam in a collisionless background plasma. The time scale and the \mathbf{E} and \mathbf{B} fields are normalized as explained in the Fig. 5.3.

(a) are taken at $T = 15(2\pi/\omega_{pe})$ and the snapshots in the next three panels are at $T = 8(2\pi/\omega_{pe})$. For a deeper understanding of the temporal evolution of the fields and the filament merging process a set of figures Fig. 5.10, 5.11 and 5.12 for four different simulation cases in the longitudinal geometry has been presented here. Each of these figures shows snapshots of the chronological growing of the Weibel \mathbf{E} and \mathbf{B} and merging of the filaments. The filaments in the collisionless case (a), similar to the transverse case, are tiny and comparable to the background plasma electron skin depth. On the contrary, in the collisional case (b), the filament size is bigger and the extent of electron diffusion is broader. A probable cause of this is the collisional diffusion of plasma electrons

5.4. Simulation Results

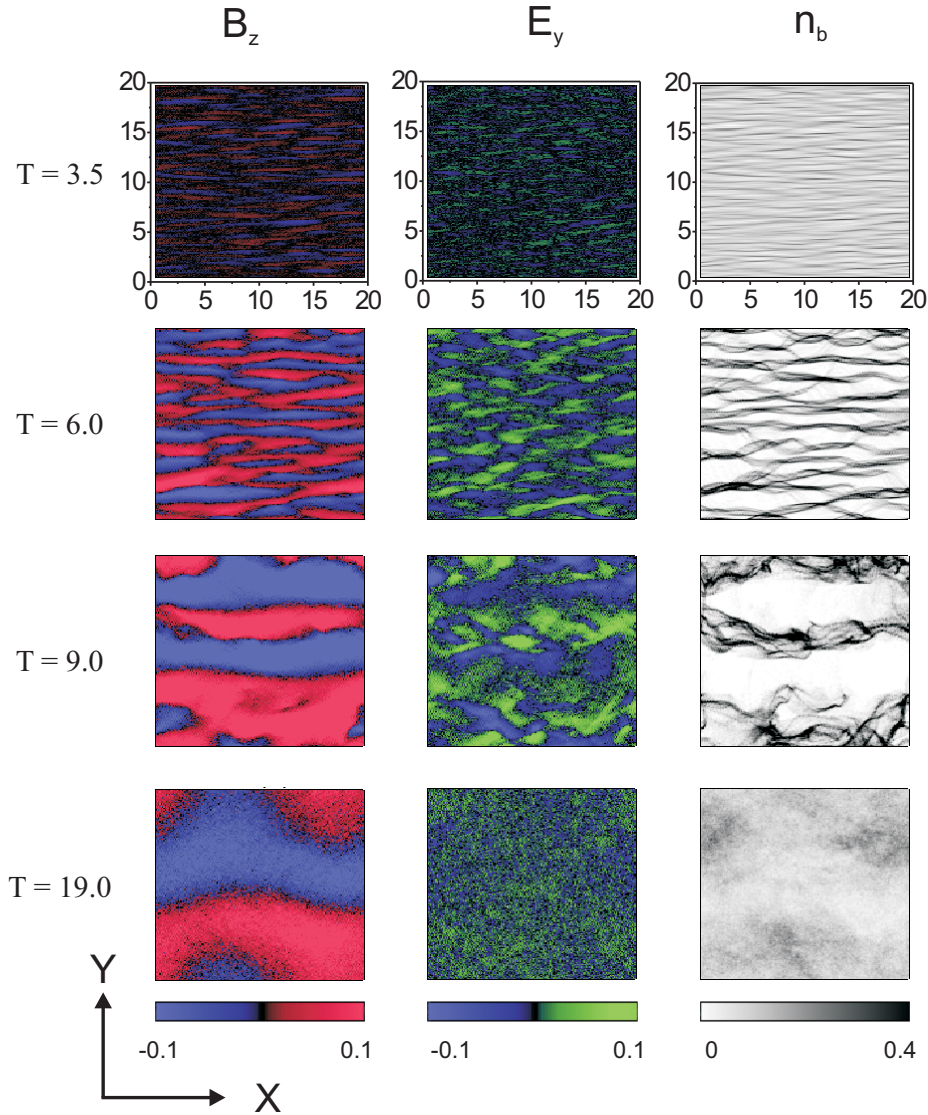


Figure 5.11: Snapshots of the temporal evolution of transverse electromagnetic Weibel fields (E_y and B_x) and beam filaments in longitudinal geometry in the simulation case (b) i.e. cold electron beam in a collisional background plasma. The time scale and the \mathbf{E} and \mathbf{B} fields are normalized as explained in the Fig. 5.3.

across the self-generated magnetic fields due to the coupled instabilities. One expects a lower build up of the field energies than the previous case in presence of collisions in, which is also seen from the simulation results here. The third panel of Fig. 5.9 shows the simulation case (c), and one does not see any filament formation similar to the transverse geometry case. Although, the Weibel instability, which is largely responsible for filament formation in relativistic conditions, gets suppressed but the two-stream instability still remains present and contributes to the build up of field energies in the system. The last panel of the figure depicts the filament formation in the simulation case (d), where the electron beam is hot and the background plasma is collisional. Evidently, the background

5. Effects of Temperature and Collisions on the Weibel Instability

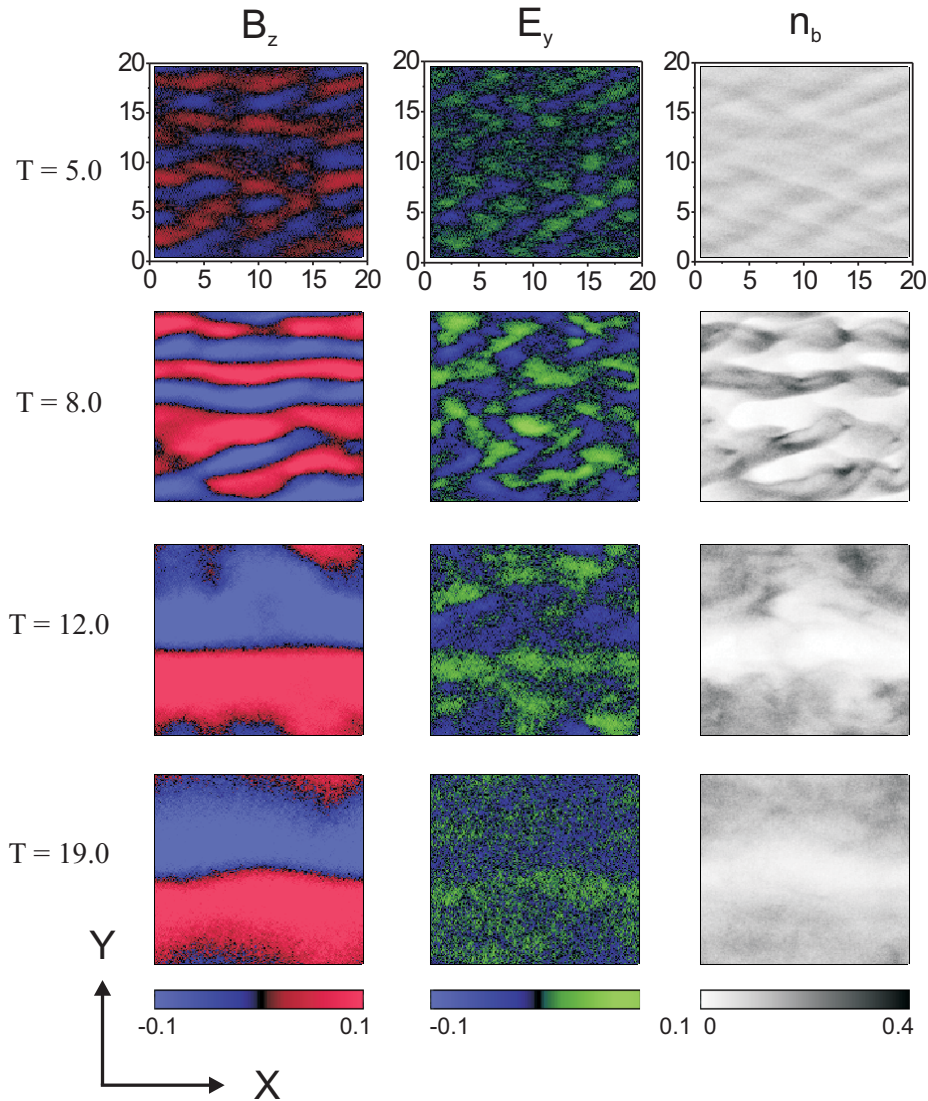


Figure 5.12: Snapshots of the temporal evolution of transverse electromagnetic Weibel fields (E_y and B_x) and beam filaments in longitudinal geometry in the simulation case (d) i.e. hot electron beam in a collisional background plasma. The time scale and the \mathbf{E} and \mathbf{B} fields are normalized as explained in the Fig. 5.3.

plasma collisions revive back the coupled instabilities, although the electron beam is hot with the same temperature as in case (c). One may also note here that, the collective effect of collisions and temperature don't suppress the Weibel instability as also observed in transverse case. Once again at this point the main implication of these simulation results is that the complete suppression of the coupled Weibel–two-stream instability in the context of FI scheme of the Inertial Confinement Fusion targets can be difficult whilst small collisions in the background plasma tend to revive back the instabilities.

Fig.5.13 shows the evolution of the transverse and longitudinal electric and magnetic field energies for the four cases in the longitudinal geometry. The vertical axes in Fig.5.13

5.4. Simulation Results

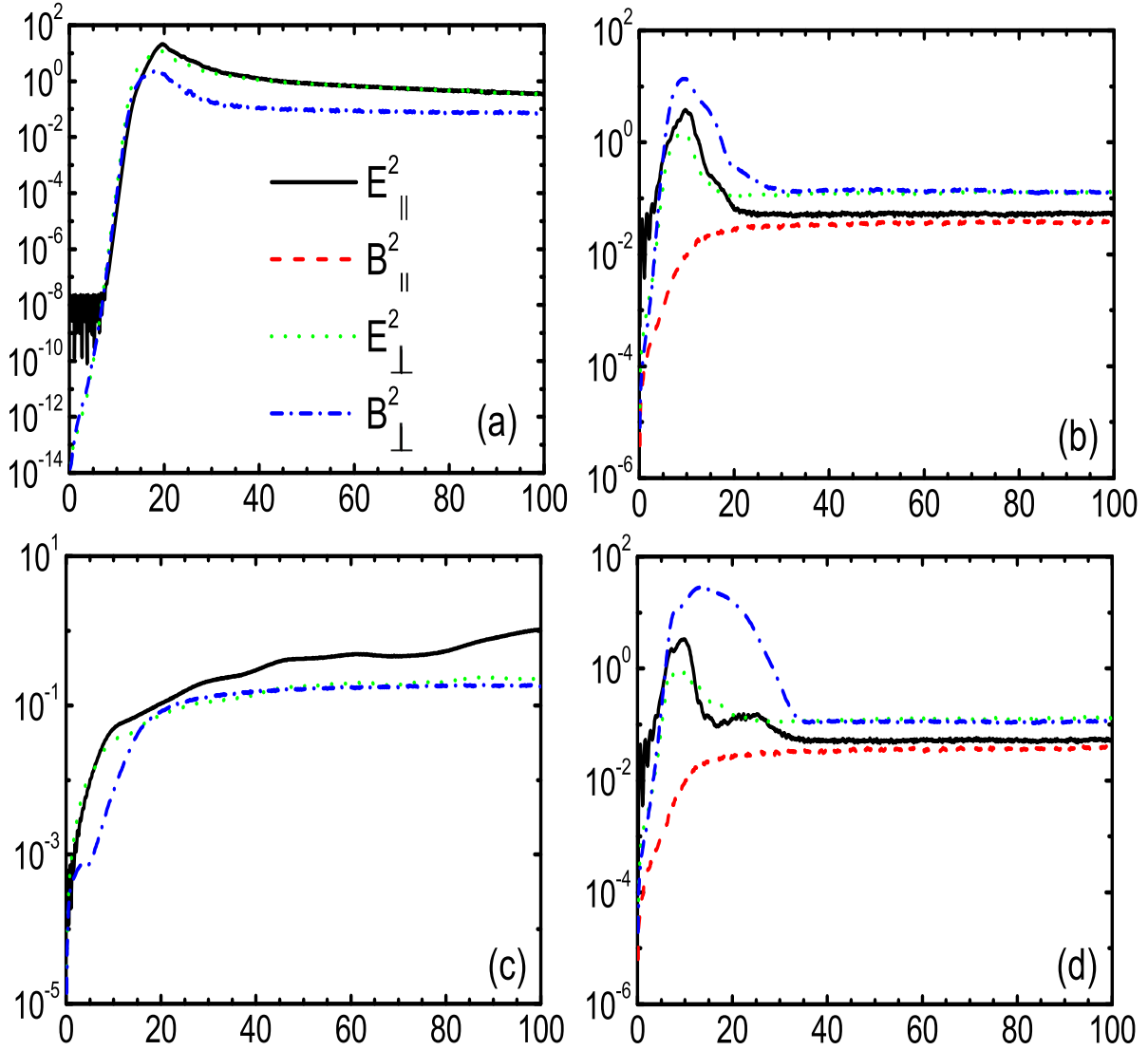


Figure 5.13: Time evolution of the transverse and longitudinal Weibel \mathbf{E} and \mathbf{B} field energies (E_{\perp}^2 , B_{\perp}^2 , E_{\parallel}^2 , B_{\parallel}^2) of longitudinal geometry for four different simulation cases as described in the previous Fig. 5.3. The horizontal axes represents the time in $(2\pi/\omega_{pe})$ and the vertical axes represents the field energies, normalized as described in Eq. (5.1).

represents the normalized field energies in logarithmic scale whereas the horizontal axes are for time scaled in $2\pi/\omega_{pe}$. Likewise the transverse geometry, here also one notices a stage of linear instability, where the field energies build up exponentially in time, and then it is followed by a nonlinear saturation. Unlike the transverse geometry the linear instability stage is present in all the simulations (a), (b), (c) and (d). A very small growth of the fields is noticed in the simulation (c), where the electron beam has high temperature and the background plasma was collisionless. This small growth rate results from the unsuppressed two-stream instability. Nevertheless the field energies saturate rapidly and don't grow to higher magnitudes as in the other three cases. This

5. Effects of Temperature and Collisions on the Weibel Instability

is in conformation with the field snapshots of Fig. 5.3. Afterwards, in the nonlinear stage of the instability, the filaments merge rapidly with each other due to the magnetic attraction and the field energies saturate. We also see strong diffusion of the beam electrons during the merging process in the nonlinear stage. The simultaneous merging and diffusion continue until the beam electrons get totally diffused in the beam plasma system. In the cases (b) and (d) this diffusion prevails more widely and the saturation of the field occur much earlier than the collisionless case. The drops in the fields E_{\parallel} , E_{\perp} and B_{\perp} in (d) and (d) can be explained due the dominance of collisional diffusion of the beam electrons over merging of the filament structures. Moreover, a growth of the longitudinal magnetic field B_{\parallel} also occurs due to collisions in the system.

5.4.3 Full 3D simulations

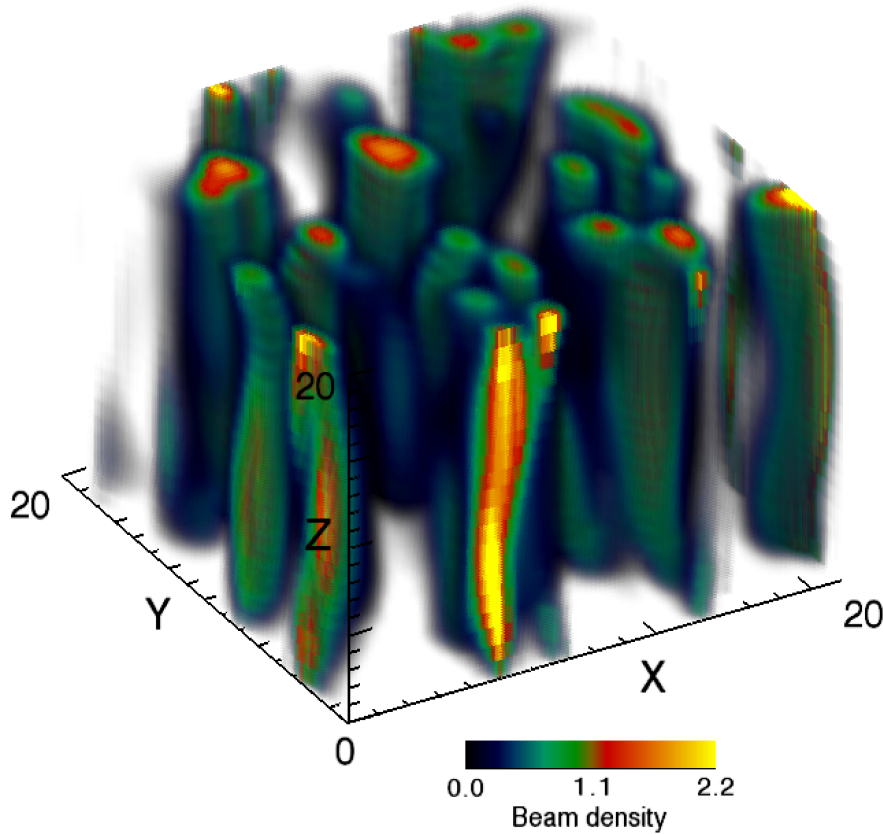


Figure 5.14: Full 3D simulation results in cold electron beam and collisionless background plasma i.e. case (a). Structure of the beam filaments at a time $T = 20(2\pi/\omega_{pe})$. The filaments have high density in the central core surrounded by a low density electron cloud.

In addition to the 2D geometries, we also have performed full 3D simulations corre-

5.5. Analytical Model

sponding to the model in Fig. 5.2 to fully understand the structure of the filaments and fields in real three dimensions. In case of 3D simulations the simulation box dimensions are $X \times Y \times Z = (20\lambda_s \times 20\lambda_s \times 20\lambda_s)$. The 3D simulation domain is sampled with a mesh of $160 \times 80 \times 20$ cells. The evolution of the bulk Weibel E and B fields are measured in every diagnostic steps summed over all the particles (N_p) as

$$\int_S E_{3d}^2 dx dy dz = \sum_{N_p} \left(\frac{e\varepsilon}{m_e c \omega_{pe}} \right)^2 N_x N_y N_z, \quad (5.2)$$

where, N_x , N_y and N_z are the number of x , y and z cells and $e\varepsilon/m_e c \omega_{pe}$ represents the field normalization. All other simulation initial parameters remain same as the 2D simulations. Fig. 5.14 shows the structure of the beam filaments at nonlinear regime in time $T = 20(2\pi/\omega_{pe})$. A plot of the transverse magnetic field B_x has been shown in Fig. 5.15. The contour lines on the bottom surface in this figure shows that each of the filaments is surrounded by strong magnetic fields.

In fact, full 3D simulations for all the other three cases i.e. (b), (c) and (d) have been performed to understand the effect of collisions on coupled Weibel–two-stream instabilities, which are always present in 3D geometry. But, at this point we restrict ourselves to the 3D simulation of the cold beam and collisionless case. A further study with all the other cases is currently being undertaken as an extension to this work.

5.5 Analytical Model

An analytical model based on the linearization of the Maxwell-fluid system of equations has been developed for the Weibel instability corresponding to the transverse geometry.

We start with the normalized Maxwell-fluid system of equations

$$\nabla \times \mathbf{E} = -\frac{\partial \mathbf{B}}{\partial t} \quad (5.3a)$$

$$\nabla \times \mathbf{B} = \frac{\partial \mathbf{E}}{\partial t} + \sum_a \mathbf{J}_a \quad (5.3b)$$

$$\nabla \cdot \mathbf{E} = 1 - \sum_a n_a, \quad \frac{\partial n_a}{\partial t} - \nabla \cdot \mathbf{J}_a = 0 \quad (5.3c)$$

$$\frac{\partial \mathbf{p}_a}{\partial t} + (\mathbf{v}_a \cdot \nabla \mathbf{p}_a) = -(\mathbf{E} + \mathbf{v}_a \times \mathbf{B}) - \nu_{ei} \mathbf{p}_a - \frac{\nabla P_a}{n_{0,a}}, \quad a = p, b, \quad (5.3d)$$

where the subscripts p and b refer to the background plasma and the beam respectively. All quantities are normalized by the velocity of light, initial plasma density, and plasma frequency.

Taking a 1D perturbation of the form $F(y, t) = f \exp(-i\omega t + ik_y y)$, we linearize these equations and obtain the dispersion relation

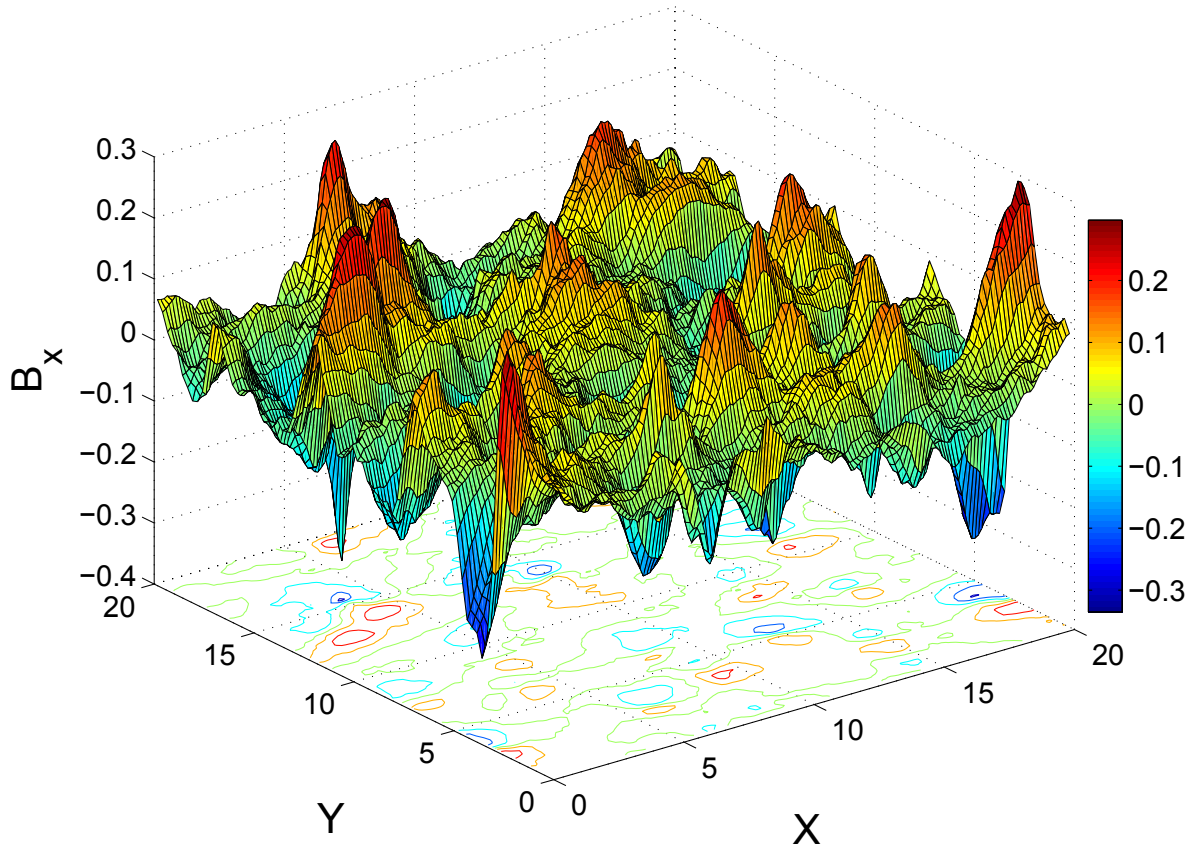


Figure 5.15: Full 3D simulation results. The transverse magnetic fields B_x at the same time. The contour lines on the bottom surface represents a 2D projections. \mathbf{B} fields are normalized as explained in the Fig. 5.3

$$\begin{aligned}
 & \left[\omega^2 (\omega_{th}^2 - \Omega_{b1}^2) \omega_{ec}^2 - \omega_{th}^2 \Omega_p^2 \omega''^2 \right] \left[\omega_{ec}^2 \omega_{th}^2 (k_y^2 - \omega^2) + \right. \\
 & \quad \left. \Omega_p^2 \omega_{th}^2 (\omega''^2 + k_y''^2 v_b^2) + \omega_{ec}^2 (\Omega_{b1}^2 k_y^2 + \omega_{th}^2 \Omega_{b2}^2) \right] + \\
 & \quad k_y^2 \left[\Omega_p^2 \omega_{th}^2 v_p \omega (1 - i \tilde{\nu}_{ei}) + \Omega_{b1}^2 \omega_{ec}^2 v_2 \omega \right]^2 = 0,
 \end{aligned} \tag{5.4}$$

where

$$\begin{aligned}
 \Omega_p^2 &= n_p / \omega_{ec}^2, \quad \Omega_{b1}^2 = n_b / (\omega_{th}^2 \gamma_b), \quad \Omega_{b2}^2 = n_b / \gamma_b^3, \\
 \omega_{ec}^2 &= (1 + \tilde{\nu}_{ei}^2) \omega^2, \quad \omega_{th}^2 = (\omega^2 - 3v_{th}^2 k_y^2), \\
 \omega''^2(k_y''^2) &= (1 - \tilde{\nu}_{ei}) \omega^2(k_y^2), \quad \tilde{\nu}_{ei} = \nu_{ei} / \omega, \\
 \gamma_b &= (1 - v_b^2)^{-1/2},
 \end{aligned}$$

5.5. Analytical Model

n_p , v_p , and n_b , v_b are the density and the velocity of background plasma and electron beam respectively. In deriving this formula we have taken the background plasma as a cold non-relativistic collisional fluid while the electron beam is a relativistic, hot and collisionless fluid.

We now study this dispersion relation in different limits by setting the appropriate values of collision frequency and the beam temperature. In cold collisionless and collisional cases ($\tilde{\nu}_{ei} = 0, v_{th} = 0, \tilde{\nu}_{ei} \neq 0, v_{th} = 0$), we recover the same dispersion relations as in Refs.[113, 114]. Similarly we also recover the dispersion relation for the hot collisionless case ($\tilde{\nu}_{ei} = 0, v_{th} \neq 0$) [114]. The growth rates of the Weibel instability for these cases are shown in Fig.5.16. We see that in the cold collisionless case (subplot (a)), the most unstable modes in the system have characteristic scale length less than the electron skin depth, λ_s . This results in small scale filament formation. The simulation result Fig.5.3(a) confirms the small scale filamentation of the cold beam propagating in collisionless plasma.

The influence of collisions in the case of a cold beam is not straightforward. It is seen from Fig.5.16(b) that the most unstable modes with wavelengths around the plasma skin depth are weakly influenced by the small collision rate. Their growth rate decreases only slowly with increase in the collision frequency in agreement with the results of Ref.[114]. At the same time, the growth rate of modes with larger wavelengths grows with collisions. This leads to formation of larger filaments as seen in the simulation Fig.5.3(b). The third subplot (c) of the Fig.5.16 shows the hot collisionless case. Evidently, increase in beam temperature results in the disappearance of the filamentation of the beam. Physically, it can be attributed to the Debye screening. For a beam temperature $v_{th} = 0.4$, the Weibel instability is completely suppressed in sync with the simulation results. The case of hot electron beam and cold collisional background plasma is fairly complicated for analytical studies due to the higher order (10^{th} order) of the dispersion relation. So we further simplify the dispersion relation (5.4) to give a simpler dispersion relation in this case. As is the case in our simulations, we assume $n_p \gg n_b$, $v_b \gg v_p$ and simplify the dispersion by keeping the lowest order terms in the Eq. (5.4) and write the dispersion relation in a diffusion-like approximation as

$$\omega^2 \approx 3v_{th}^2 k_y^2 - \frac{n_b k_y^2 v_b^2}{\gamma_b (k_y^2 + n_p/\beta)}, \quad (5.5)$$

where $\beta = (1 + \tilde{\nu}_{ei})$. This dispersion relation is analogous to the one derived by Molvig [164]. The roles of the magnetic field which stabilizes the Weibel instability in Molvig's model is replaced here by the beam temperature which does the same thing as the magnetic field. A plot of the instability growth is shown in the Fig.5.16(d) for several values of $\tilde{\nu}_{ei}$ at the beam temperature $T_b = 70$ keV ($v_{th} = 0.4$). The important result is that even small rate of collisions revives the instability and its growth rate increases with collision frequency for small collision rates. For higher collision frequencies, $\tilde{\nu}_{ei} \gg \omega_p$, the growth will decrease again. Hence collisions play a different role here. Although the role of collisions in reviving the Weibel instability is mathematically apparent from Eq.(5.5), it could be understood physically in terms of the unstable neg-

5. Effects of Temperature and Collisions on the Weibel Instability

ative energy waves. It is well known that collisions can sometime drive wave oscillations unstable in a plasma [165, 166]. The passage of the beam in the plasma actually excites waves with phase velocity slower than the beam velocity. These can be termed as negative energy waves as they carry negative energy densities with them. Dissipations act in a different way on these waves and may drive them unstable. This is also known as the dissipative instability [167]. When the negative energy waves are driven unstable, the wave oscillations in plasma are also driven unstable to minimize the total energy of a beam plasma system, which is always positive.

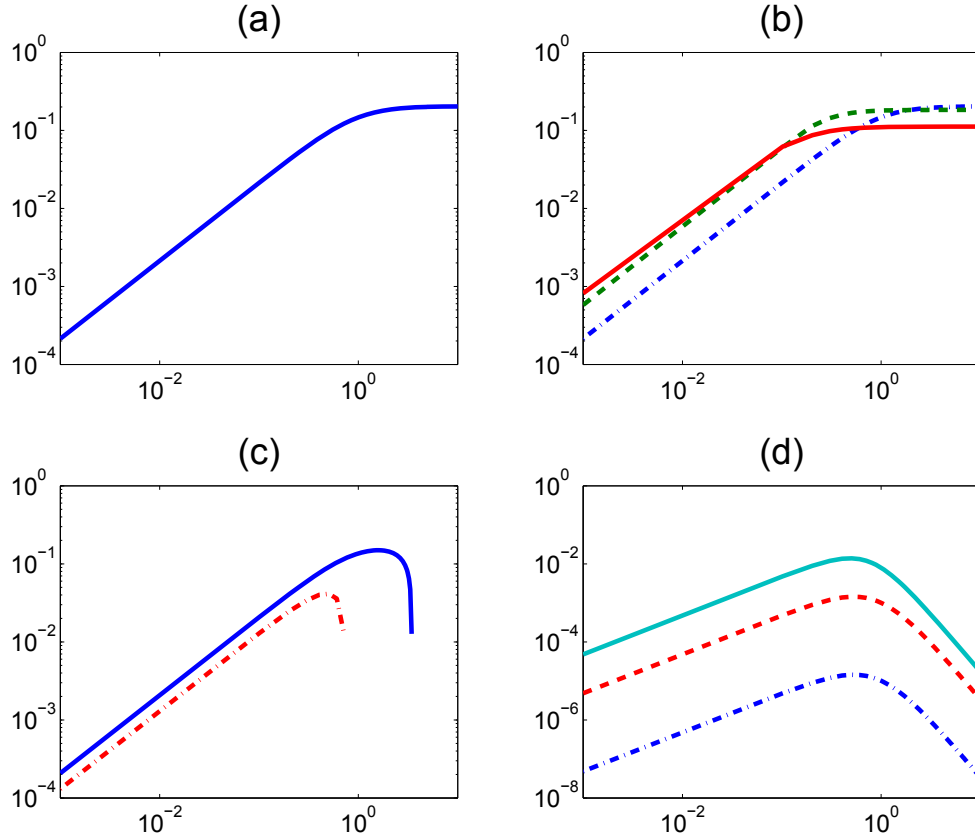


Figure 5.16: The growth rates calculated from the dispersion relations Eq.(5.4) for the four cases (a) cold collisionless case (b) cold collisional plasma (dash-dot line, $\tilde{\nu}_{ei} = 0.1$, dash line, $\tilde{\nu}_{ei} = 1$, solid line, $\tilde{\nu}_{ei} = 100$) (c) hot electron beam and collisionless background plasma (solid line, $v_{th} = 0.05$, dash-dot line, $v_{th} = 0.15$) (d) hot electron beam and collisional background plasma (dash-dot line, $\tilde{\nu}_{ei} = 0.001$, dash line, $\tilde{\nu}_{ei} = 0.1$, solid line, $\tilde{\nu}_{ei} = 1$). In all subplots, the vertical axis represents the normalized growth rate, Γ , and the horizontal axis represents the normalized wave vector, k_y . The last subplot (d) corresponds to the Eq.(5.5). The other parameters for beam and plasma are same as in the simulation.

Finally, comparisons of analytical and simulation growth rate of the linear Weibel

5.5. Analytical Model

instability for the transverse geometry in various cases is shown in the Table 5.1, which highlights a good agreement between the simulation and the theory.

Cases	Γ		k_y^{-1} (in c/ω_{pe})	
	Numerical	Analytical	Numerical	Analytical
(a)	0.19	0.20	0.70	0.50
(b)	0.18	0.20	0.50	0.50
(c)	$\approx 10^{-4}$	No Growth	-	-
(d)	0.12	0.025	3.00	2.50

Table 5.1: Comparison of linear growth rates (Γ) and scale lengths of filaments formation (k_y^{-1}) for transverse geometry for both numerical simulations and analytical calculation. The rows (a), (b), (c) and (d) represent the same cases as in the Fig. 5.3.

The analytical theory for the longitudinal geometry is still under development. The comparison of the simulation results for the longitudinal geometry case will be reported elsewhere later. Here we proceed to tabulate briefly the linear growth rates (Γ) in Table.5.2 for the four different cases as the transverse geometry.

Cases	Γ (Numerical)	k_y^{-1} (Numerical) (in c/ω_{pe})
(a)	0.161	≈ 0.50
(b)	0.115	≈ 0.75
(c)	0.025	≈ 0.00
(d)	0.117	≈ 4.16

Table 5.2: Linear growth rates (Γ) for longitudinal geometry for numerical simulations. The rows (a), (b), (c) and (d) represent the same cases as in the Fig. 5.3.

The linear growth rates for the longitudinal geometry i.e. coupled Weibel–two-stream instability, show that due to collisions the growth rates increase and the temperature cannot kill the instabilities fully. This is a consequence of the structure of fields and filaments in Fig. 5.9. Moreover, it is evident that simultaneous effects of beam temperature and plasma collisions have the similar effects like the transverse geometry. The scale lengths for filament formation for the longitudinal geometry also proves that collisions increase the size of filaments. Additionally, temperature and collision simultaneously increases these scale lengths drastically. These observations can be explained with an interplay between electrostatic waves and collisions. The electrostatic waves produced by the two-stream instability could act potentially as a boost to the effective collisions. These electrostatic waves, as a ponderomotive force, replaces the electron-ion collision in the case (b). Hence, the instability cannot be suppressed even with a high beam temperature. Because the frequency spectrum of these electrostatic waves is very narrow, almost at the ambient plasma frequency, the resulting ponderomotive force is static, i.e. very similar to electron-ion collisions. On the other hand, the spatial spectrum of these waves (in k_x and k_y) is rather broad. Again, exactly as it is the case with the electron-ion

collisions. So, one can conclude that the addition of the two-stream instability in case of longitudinal geometry destabilizes the otherwise suppressed Weibel instability.

5.6 Conclusion

In summary, we have carried out detailed 2D simulations with two different geometries on the Weibel instability and coupled Weibel–two-stream instabilities of an electron beam in two-dimensional geometry, in a parameter regime which is relevant to the FI scheme. Additionally, a set of full 3D simulations have also been performed to understand the system more realistically. We have studied the effects of various factors such as electron beam temperature and collisions in the return plasma current separately as well as collectively. The finite temperature of the electron beam tends to suppress the Weibel instability but the coupled two-stream instability remains unsuppressed. However, collisions in the return plasma current plays a paradoxical role and revive back the Weibel instability. This paradoxical role of collisions is attributed to the instability of negative energy waves which can be present in such type of beam plasma systems. Thus it seems that the Weibel and two-stream instabilities are difficult to suppress and will play a dominant role to in the Fast Ignition scheme.

6 Conclusion

In conclusion, we summarize all the principal results of the works presented in this thesis. First of all, the mechanism of electron acceleration in vacuum with radially polarized ultra-intense ultra-short laser beam has been studied. It is shown that single-cycle laser pulses efficiently accelerate a single attosecond electron bunch to GeV energies. When multi-cycle laser pulses are used, one has to employ ionization of high- Z materials to inject electrons in the accelerating phase at the laser pulse maximum. In this case, a train of highly collimated attosecond electron bunches with a quasi-monoenergetic spectra is produced. Moreover, it is shown that the radially polarized laser pulses are superior to the Gaussian pulse, both in maximum energy gain and in the quality of the produced electron beams. Additionally, hot electron and x-ray production from high-contrast laser irradiated polystyrene-spheres have been studied. A sphere-size scan of the x-ray yield and observation of a peak in both the x-ray production and temperature at a sphere diameter of $0.26 \mu\text{m}$, indicates that these results are consistent with Mie enhancements of the laser field at the sphere surface and multipass stochastic heating of the hot electrons in the oscillating laser field. The PIC simulation results have matched well with the experimental findings [41].

Secondly, electron acceleration from solid target surfaces by a sub-10-fs laser pulses of focused intensity $\sim 10^{16} \text{ W/cm}^2$ has been successfully studied. It has been demonstrated, that these electrons have a very narrow angular distribution and their observed energies are much higher than expected from the usual ponderomotive acceleration. It is shown that this boost in electron energies is not due to collective plasma effects, but comes mainly from the laser field due to a repeated acceleration in the vacuum after scattering in the solid.

Thirdly, we presented a new one-dimensional fully electromagnetic relativistic hybrid plasma model. The fully kinetic particle-in-cell (PIC) and hydrodynamic model have been combined in the single hybrid plasma code H-VLPL (hybrid virtual laser plasma laboratory). The semi-implicit algorithm allows us to simulate plasmas of arbitrary densities via automatic reduction of the highest plasma frequencies down to the numerically stable range. At the same time, the model keeps the correct spatial scales like the plasma skin depth. The new mathematical method allows to overcome the typical time step restrictions of explicit PIC codes. This hybrid code will be very efficient in studying ultra-high intensity laser-solid interaction experiments and the Fast Ignition (FI) scheme of Inertial Confinement Fusion (ICF).

Lastly, transport of a relativistic electron beam in Fast Ignition (FI) plasma has been studied to understand the effects of background plasma collisions and beam temperature on coupled instabilities. The roles of collisions and beam temperature has been investigated separately as well as collectively during the linear and nonlinear stages of

6. Conclusion

the instabilities. We have showed that collisions in the return plasma current plays a paradoxical role and revive back the Weibel and two-stream instabilities. Hence, in summary to this work, the Weibel and two-stream instabilities are difficult to suppress and they play the dominant role in the FI scheme.

A Particle-in-cell (PIC) Simulation Codes

The laser-plasma interaction physics is now-a-days concentrated mainly in the ultra-relativistic regime of short laser pulses, where the dynamics of the electrons as well as ions are heavily non-linear. This is obvious that, the relativistic gamma factor of these particles are much larger, $\gamma \gg 1$ and the analytical models are not always very efficient and straightforward. Hence, numerical simulations, using particle-in-cell (PIC) [91, 92, 168, 169] or other technique are extremely essential. As a matter of fact, in past decade PIC methods emerged to be very successful, reliable and versatile tool for kinetic plasma simulations. Here, we briefly present the basics of PIC simulation added by a discussion on the code VLPL [95], used for all the simulations presented in this thesis.

In reality PIC codes are very analogous to the actual plasma, which in reality, is an ensemble of many electrons and ions, interacting with each other by the self-consistently generated fields [11]. The code efficiently models the real plasma with a difference that the number of numerical particles, called ‘macroparticles’ in PIC methods, may be significantly smaller [11] than real number of particles. Each numerical macroparticle, or more technically the Finite Phase Fluid Elements (FPFE), of the PIC methods represents a certain assembly or cloud of many real particles. The PIC method allows the statistical representation of general distribution function in phase space [99]. A ‘macroparticle’ occupy a finite volume in phase space and represents the velocity of the real electrons or ions. Further, the charge-to-mass ration of these numerical particles are same as real electrons or ions. The fundamental equations of the PIC methods, in most of the cases, contain the full non-linear effects, and other collective effects can very well be incorporated self-consistently via the source terms [99]. Moreover, addition of relativistic effects is also a very significant feature of PIC methods. In short, PIC codes, utilize very fundamental equations including all the basic physics.

A.1 The Basic Equations

Let us now consider the master equations for the relativistic electromagnetic kinetic simulation. The Maxwell’s equations for field in CGS units are

$$\text{rot } \mathbf{B} = \frac{1}{c} \frac{\partial \mathbf{E}}{\partial t} + \frac{4\pi}{c} \mathbf{J} \quad (\text{A.1a})$$

$$\text{rot } \mathbf{E} = -\frac{1}{c} \frac{\partial \mathbf{B}}{\partial t} \quad (\text{A.1b})$$

$$\text{div } \mathbf{E} = 4\pi\rho \quad (\text{A.1c})$$

$$\text{div } \mathbf{B} = 0 \quad (\text{A.1d})$$

where c is the speed of light in vacuum and ρ is the local charge density, and for the motion of the particles, both electrons and ions,

$$\begin{aligned} \frac{d\mathbf{p}}{dt} &= e\mathbf{E} + \frac{e}{c} (\mathbf{v} \times \mathbf{B}) \\ \frac{d\mathbf{x}}{dt} &= \frac{\mathbf{p}}{\gamma m} \end{aligned} \quad (\text{A.2})$$

The \mathbf{E} and \mathbf{B} fields evolve through the first two time-dependent Maxwells' equations A.1a and A.1b with the source term in the form of current density \mathbf{J} , which is produced due to the self-consistent motion of the system of particles. Now, one can argue that, the third equation of Eq. A.1, i.e., Eq.A.1c is satisfied automatically during the evolution of the system, if the charge density always satisfies the continuity equation

$$\frac{\partial \rho}{\partial t} + \nabla \cdot \mathbf{J} = 0 . \quad (\text{A.3})$$

Moreover, as we do not have any magnetic charges, fourth field equation Eq. A.1d also remains valid taking the symmetric considerations. Therefore, from the four field equations in Eq. A.1, we can reduce the system of equations to only the first two very significant equations Eq. A.1a and A.1b considering the Eq. A.1c and A.1d as merely the initial conditions. This approximation is very feasible, as well as fruitful. The numerical particles' motion is calculated according to the equations of motion A.2. The charge density at each grid point (see [91]) in the PIC domain is determined by assigning particles to the grid according to their positions and the weighting scheme. The scheme of a PIC computational cycle is shown on Figure A.1. A detailed discussion can be found in [91, 92].

Lately, there has been several modifications, to this simple PIC algorithm. A discussion on this can be found on Chapter. 1 and Chapter 4 of this thesis. A number of physical processes, such as binary collisions, ionizations, etc., can be incorporated to PIC methods efficiently. A particle-in-cell method merged with Monte Carlo collision (MCC) calculations was described in [133]. For a detailed discussion on the implementation of collision and ionization modules we refer to the Chapter. 2 and Chapter 3, respectively, of this thesis.

A.2. The Code VLPL

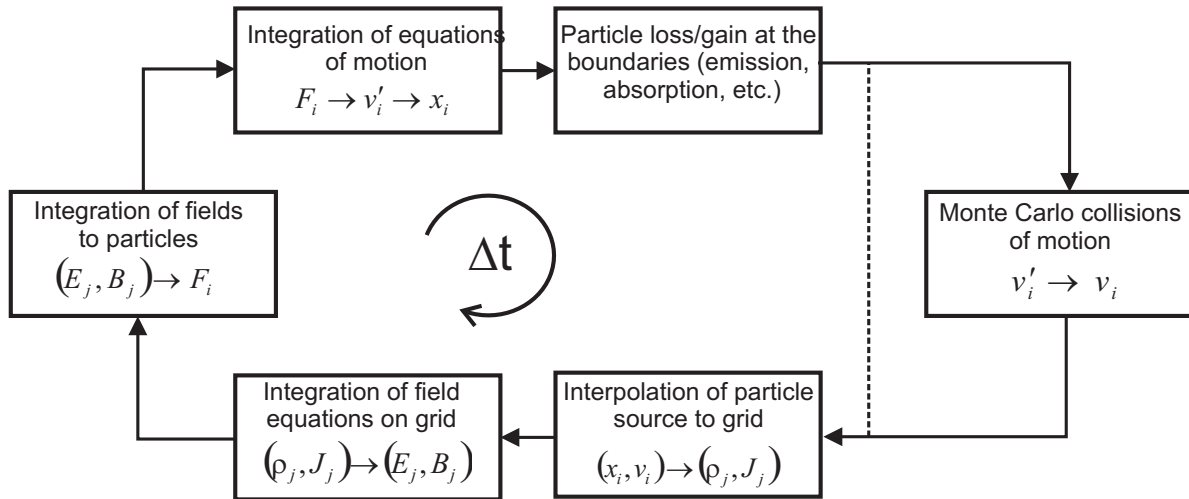


Figure A.1: Flow schematic for the PIC scheme with a Monte Carlo Collision (MCC) module in one single time-step (Figure adopted from [99]).

Plasma or neutral gas
(Barrier Suppression
Ionization)

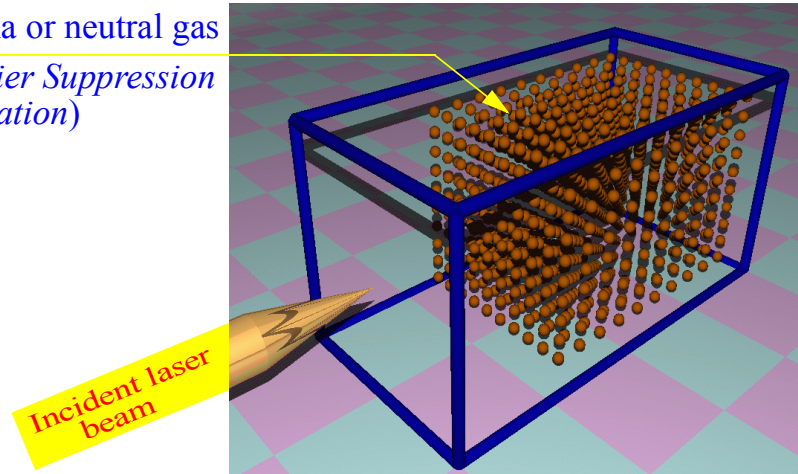


Figure A.2: The usual simulation geometry of the VLPL

A.2 The Code VLPL

All the kinetic simulations discussed in this thesis have been performed with the three dimensional relativistic PIC (3D-PIC) code Virtual Laser Plasma Laboratory (VLPL) [95], initially created by Pukhov *et al.* VLPL is a relativistic energy conservative fully electromagnetic particle-in-cell (PIC) code and runs on massively parallel processors (MPP) exploiting Message Passing Interface (MPI) and domain decomposition methods. VLPL is written in C++ following the object-oriented technology. Presently, 1D (1D3V) and 3D (3D3V) versions of the code are maintained. The code has also been equipped with ADK tunneling ionization (Chapter. 2) and binary collision (Chapter. 3) modules by

A. Particle-in-cell (PIC) Simulation Codes

the author of this thesis. These implementations allow us to study the effects of ionization, collisions and collisional ionizations in a vast range of laser plasma-interaction physics. PIC simulations performed with this code have been able to successfully reproduce the real experiments. Moreover, the basic interface of the newly developed implicit PIC-hydrodynamic hybrid simulation code HVLPL [55] is adopted from the VLPL code. The usual simulation geometry and the class structure of the code VLPL have been shown in Fig. A.2 and Fig. A.3, respectively. Lastly, most of the simulations presented in this thesis have been performed with the parallel Dual-Core IBM Linux cluster ‘NOVAGIGA’ of 70 Xeon-Processors, and some of the simulations demonstrated in Chapter. 5 have been done in the Dell Dual-Core Linux cluster ‘LONESTAR’ of the Texas Advanced Computing Center, USA [170].

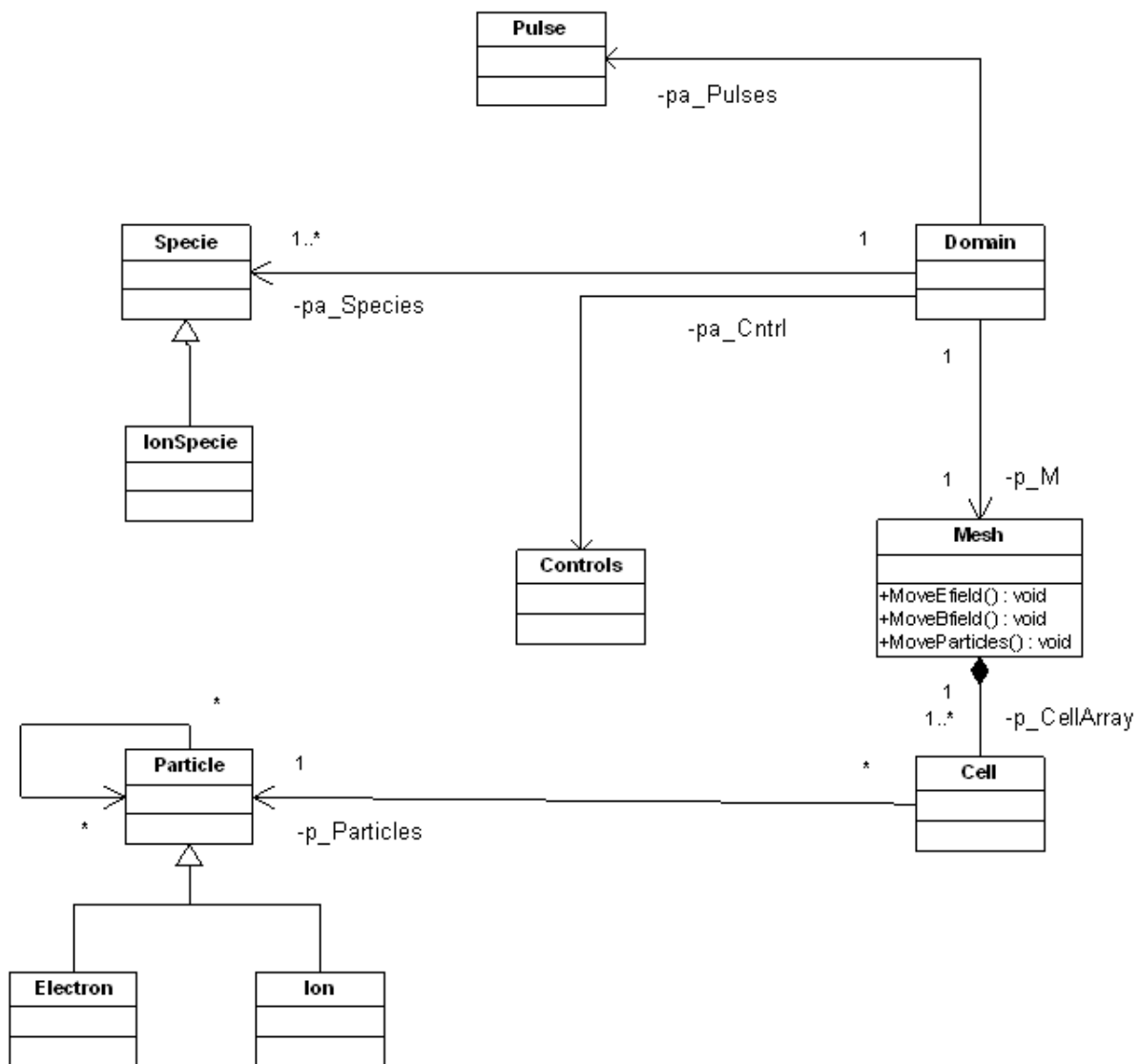


Figure A.3: UML Class and interface description of the 3D PIC code VLPL.

References

- [1] D. Strickland and G. Mourou, *Compression of amplified chirped optical pulses*, Opt. Commun. **56**, 219 (1985).
- [2] S.-W. Bahk, P. Rousseau, T. Planchon, V. Chvykov, G. Kalintchenko, A. Maksimchuk, G. Mourou, V. Yanovsky, *Characterization of focal field formed by a large numerical aperture paraboloidal mirror and generation of ultra-high intensity (10^{22} W/cm²)*, Appl. Phys. B. **80**, 823 (2005).
V. Yanovsky, V. Chvykov, G. Kalinchenko, P. Rousseau, T. Planchon, T. Matsuoka, A. Maksimchuk, J. Nees, G. Cheriaux, G. Mourou, and K. Krushelnick, *Ultra-high intensity- 300-TW laser at 0.1 Hz repetition rate*, Optics Express **16**, 2109 (2008).
- [3] F. Krausz *et al*, *PW Field Synthesizer: PFS*, MPQ project study (2005).
- [4] A. Feuerbach, A. Fernandez, A. Apolonski, T. Fuji, F. Krausz, *Chirped-pulse oscillators for the generation of high-energy femtosecond laser pulses*, Laser Part. Beams **23(2)**, 113-116 (2005).
- [5] ELI – Extreme Light Infrastructure Project; E. Gerstner, *Laser physics: Extreme light*, Nature **446**, 16 (2007)
- [6] G. Mourou and D. Umstadter, *Development and applications of compact high intensity lasers*, Phys. Fluids B **4**, 2315 (1992).
- [7] M. D. Perry and G. Mourou, *Terawatt to petawatt sub-picosecond lasers*, Science **64**, 917 (1994).
- [8] T. Tajima, J. M. Dawson, *Laser Electron Accelerator*, Phys. Rev. Lett. **43**, 267 (1979);
- [9] J. M. Dawson, *Plasma Particle Accelerators*, Scientific American, 260, 54 (1989).
- [10] V. Malka, S. Fritzler, E. Lefebvre *et al.*, *Electron Acceleration by a Wake Field Forced by an Intense Ultrashort Laser Pulse*, Science **298**, 1596 (2002).
- [11] A. Pukhov, *Strong field interaction of laser radiation*, Rep. Prog. Phys. **66**, 47 - 101 (2003).
- [12] W. P. Leemans, B. Nagler, A. J. Gonsalves, Cs. Tóth, K. Nakamura, C. G. R. Geddes, E. Esarey, C. B. Schroeder and S. M. Hooker, *GeV electron beams from a centimeter-scale accelerator*, Nature Physics **2**, 696 (2006).

REFERENCES

- [13] A. Karmakar and A. Pukhov, *Collimated attosecond GeV electron bunches from ionization of high-Z material by radially polarized ultra-relativistic laser pulses*, Laser Part. Beams **25**, 371 (2007).
- [14] F. Brandl, B. Hidding, J. Osterholz, D. Hemmers, A. Karmakar, A. Pukhov and G. Pretzler, *Directed acceleration of electrons from a solid surface by sub-10-fs laser pulses*, Phys. Rev. Lett. **communicated** (2008).
- [15] A. M. Perelomov, V. S. Popov and M. V. Terent'ev, *Ionization of atoms in an alternating electric field*, Soviet Phys. JETP **23**, 924 (1966).
- [16] M. V. Ammosov, N. B. Delone and V. P. Krainov, *Tunnel ionization of the complex atoms and of atomic ions in an alternating electromagnetic field*, Sov. Phys. JETP **64**, 1191 (1986).
- [17] S. Augst, D. D. Meyerhofer, D. Strickland and S. I. Chin, *Laser ionization of nobler gases by Coulomb-barrier suppression*, J. Opt. Soc. Am. B **8** 858 (1991).
- [18] A. Scrinzi, Michael Geissler and Thomas Brabec, *Ionization above the Coulomb barrier*, Phys. Rev. Lett **83**, 706, (1999).
- [19] B. Hafizi, P. Sprangle, J. R. Penano and D. F. Gordon, *Electron distribution function in short-pulse photoionization*, Phys. Rev. **E67**, 056407 (2003).
- [20] A J. Kemp, R E. W. Pfund and J. Meyer-ter-Vehn, *Modeling ultrafast laser-driven ionization dynamics with Monte Carlo collisional particle-in-cell simulations*, Phys. Plasmas **11**, 5648 (2004)
- [21] J. Dawson and C. Oberman, *High-Frequency Conductivity and the Emission and Absorption Coefficients of a Fully Ionized Plasma*, Phys. Fluids **5**, 517 (1962).
- [22] J. M. Wallace, D. W. Kindel, G. L. Olson and J. C. Comly, *Short-pulse laser-plasma interaction including collisions and ionization*, Phys. Fluids B **3**, 2337 (1991).
- [23] J. M. Wallace, J. U. Brackbill, C. W. Cranfill, *et al.*, *Collisional effects on the Weibel instability*, Phys. Fluids **30**, 1085 (1987).
- [24] P. B. Corkum, N. H. Burnett, and F. Brunel, *Above-threshold ionization in the long-wavelength limit*, Phys. Rev. Lett. **62**, 1259 (1989).
- [25] A. Zhidkov and A. Sasaki, *Effect of field ionization on interaction of an intense subpicosecond laser pulse with foils*, Phys. Plasmas **7**, 1341 (2000).
- [26] V. T. Tikhonchuk, *Interaction of a beam of fast electrons with solids*, Phys. Plasmas **9**, 1416 (2002).
- [27] J. A. Stamper, K. Papadopoulos, R. N. Sudan, S. O. Dean, E. A. McLean, and J. M. Dawson, *Spontaneous Magnetic Fields in Laser-Produced Plasmas*, Phys. Rev. Lett. **26**, 1012 (1971).

REFERENCES

- [28] R. N. Sudan, *Mechanism for the generation of 109 G magnetic fields in the interaction of ultraintense short laser pulse with an overdense plasma target*, Phys. Rev. Lett. **70**, 3075 (1993).
- [29] M. Borghesi, A. J. MacKinnon, A. R. Bell, R. Gaillard, and O. Willi, *Megagauss Magnetic Field Generation and Plasma Jet Formation on Solid Targets Irradiated by an Ultraintense Picosecond Laser Pulse*, Phys. Rev. Lett. **81**, 112 (1998).
- [30] S. Kato, T. Nakamura, K. Mima, Y. Sentoku, H. Nagatomo, and Y. Owadano, *Generation of quasistatic magnetic field in the relativistic laser-plasma interactions*, J. Plasma Fusion Res. SERIES **6**, 658 (2004).
- [31] H. Cai, W. Yu, S. Zhu, and C. Zhou, *Generation of strong quasistatic magnetic fields in interactions of ultraintense and short laser pulses with overdense plasma targets*, Phys. Rev. E **76**, 036403 (2007).
- [32] G. Shvets, N. J. Fisch, A. Pukhov and J. Meyer-ter-Vehn, *Superradiant Amplification of an Ultrashort Laser Pulse in a Plasma by a counterpropagating Pump*, Phys. Rev. Lett. **81**, 004879 (1998).
- [33] O. Shorokhov, A. Pukhov, I. Kostyukov, *Self-compression of laser pulses in plasma*, Phys. Rev. Lett. **91**, 265002, (2003)
- [34] J. Faure, Y. Glinec, J. J. Santos, F. Ewald, J.-P. Rousseau, S. Kiselev, A. Pukhov, T. Hosokai, and V. Malka, *Observation of Laser-Pulse Shortening in Nonlinear Plasma Waves*, Phys. Rev. Lett. **95**, 205003 (2005).
- [35] S. C. Wilks, A. B. Langdon, T. E. Cowan *et al.*, *Energetic proton generation in ultra-intense laser-solid interaction*, Phys. Plasmas **8**, 542 (2001).
- [36] A. Pukhov, *Three-Dimensional Simulations of Ion Acceleration from a Foil Irradiated by a Short-Pulse Laser*, Phys. Rev. Lett. **86**, 3562 (2001).
- [37] S. Gordienko, A. Pukhov, O. Shorokhov, T. Baeva, *Relativistic Doppler effect: Universal spectra and zeptosecond pulses*, Phys. Rev. Lett. **93**, 115002 (2004).
- [38] S. Gordienko, A. Pukhov, O. Shorokhov, T. Baeva, *Coherent focusing of high harmonics: A new way towards the extreme intensities*, Phys. Rev. Lett. **94**, 103903 (2005).
- [39] B. Dromey, M. Zepf, A. Gopal, *et al.*, *High harmonic generation in the relativistic limit*, Nature Physics, **2**, 456 (2006).
- [40] S. Kiselev, A. Pukhov, I. Kostyukov, *X-ray generation in strongly nonlinear plasma waves*, Phys. Rev. Lett. **93**, 135004 (2004).

REFERENCES

- [41] H. Sumeruk, S. Kneip, D. Symes, I. Churina, A. Belolipetski, G. Dyer, J. Landry, G. Bansal, A. Bernstein, T. Donnelly, A. Karmakar, A. Pukhov and T. Ditmire, *Hot electron and x-ray production from intense laser irradiation of wavelength-scale polystyrene spheres*, Phys. Plasmas **14**, 062704 (2007).
- [42] S. Atzeni, *Laser-plasma interaction and high-pressure generation for inertial fusion and basic science*, Plasma Phys. Control. Fusion **42**, B143 (2000).
- [43] C. Gahn, G. D. Tsakiris, A. Pukhov, J. Meyer-ter-Vehn, G. Pretzler, P. Thirolf, D. Habs, and K. J. Witte, *Multi-MeV Electron Beam Generation by Direct Laser Acceleration in High-Density Plasma Channels*, Phys. Rev. Lett. **83**, 004772 (1999).
- [44] A. Pukhov & J. Meyer-ter-Vehn, *Laser wake field acceleration: the highly non-linear broken-wave regime*, J. Appl. Phys. **B74**, 355 (2002).
- [45] K. P. Singh, *Self-injection and acceleration of electrons during ionization of gas atoms by a short laser pulse* Phys, Plasmas **13**, 043101 (2006).
- [46] Y. Salamin, *Mono-energetic GeV electrons from ionization in a radially polarized laser beam*, Optics. Lett. **32**, 90 (2007).
- [47] R. ommasini, E. Fill, R. Bruch and G. Pretzler, *Generation of monoenergetic ultrashort electron pulses from a fs laser plasma*, Journal App. Phys. B: Lasers and Optics **79**, 923 (2004).
- [48] Max Tabak, James Hammer, Michael E. Glinsky, *et al.*, *Ignition and high gain with ultrapowerful lasers*, Phys. Plasmas **1**, 1626 (1994).
- [49] E. S. Weibel, *Spontaneously Growing Transverse Waves in a Plasma Due to an Anisotropic Velocity Distribution*, Phys. Rev. Lett. **2** 83, (1959).
- [50] J. A. Bittencourt, *Fundamentals of Plasma Physics* (Third Ed. 2004 Springer-Verlag, New York, 2004).
- [51] F. F. Chen, *Introduction to Plasma Physics and Controlled Fusion* (Second Ed., Plenum Press, New York, 1984).
- [52] D. R. Nicholson, *Introduction to Plasma Theory* (John Wiley & Sons, New York 1983).
- [53] B. T. Tsurutani and G. S. Lakhina, *Some Basic Concepts of Wave-Particle Interactions in Collisionless Plasmas*, Rev. Geophys. **35**, 491 (1997).
- [54] L. Robson, P. T. Simpson, R. J. Clarke, *et al.*, *Scaling of proton acceleration driven by petawatt-laser plasma interactions*, Nature Physics **3**, 58 (2007);
M. Roth, A. Blazevic, M. Geissel *et al.*, *Energetic ions generated by laser pulses: A detailed study on target properties*, Phys. Rev. ST Accelerators and Beams **5**, 061301 (2002);

REFERENCES

- M. Kaluza, J. Schreiber, M. I. K. Santala, *et al.*, *Influence of the Laser Prepulse on Proton Acceleration in Thin-Foil Experiments*, Phys. Rev. Lett. **93** 045003 (2004).
- [55] J. Liljo, A. Karmakar, A. Pukhov, M. Hochbruck, *One dimensional electromagnetic relativistic PIC-Hydrodynamic hybrid simulation code H-VLPL (Hybrid Virtual Laser Plasma Lab)*, Comp. Phys. Commn. **article in press**, DOI: 10.1016/j.cpc.2008.03.008 (2008).
- [56] L. V. Keldysh, *Ionization in the field of a strong electromagnetic wave*, Sov. Phys. JETP **20**, 1307 (1965).
- [57] N. A. Krall, A. W. Trivelpiece, *Principles of Plasma Physics*, McGraw-Hill, New York (1973).
- [58] E. S. Sarachik and G. T. Schappert, *Classical theory of the scattering of intense laser radiation by free electrons*, Phys. Rev. **D1**, 2738 (1970).
- [59] P. B. Corkum, N. H. Burnett, and F. Brunel, *Atoms in Intense Laser Fields*, ed. M. Gavrilu. (Academic, New York, 1992).
- [60] L. D. Landau and E. M. Lifschitz, *Mechanics (Course on Theoretical Mechanics)*, Third Ed. (Oxford, England: Pergamon Press, 1976).
- [61] W. L. Kruer, *The Physics of Laser-Plasma Interactions*, (Reading, MA: Addison-Wesley, New York, 1988).
- [62] D. Bauer, P. Mulser, and W.-H. Steeb, *Relativistic ponderomotive force, uphill acceleration, and transition to chaos*, Phys. Rev. Lett. **75**, 4622 (1995).
- [63] B. Quesnel and P. Mora, *Theory and simulation of the interaction of ultraintense laser pulses with electrons in vacuum*, Phys. Rev. E **58**, 3719 (1998).
- [64] A. Pukhov, Z. Sheng, and J. Meyer-Ter-Vehn, *Particle acceleration in relativistic laser channels*, Phys. Plasmas **6**, 2847 (1999).
- [65] G. D. Tsakiris, C. Gahn, and V. K. Tripathi, *Laser induced electron acceleration in the presence of static electric and magnetic fields in a plasma*, Phys. Plasmas **7**, 3017 (2000).
- [66] E. Esarey, P. Sprangle, J. Krall, A. Ting, *Overview of plasma-based accelerator concepts*, IEEE Trans. Plasma Sci. **24**, 252 (1996).
- [67] P. Sprangle, E. Esarey, J. Krall, and G. Joyce, *Propagation and guiding of intense laser pulses in plasmas*, Phys. Rev. Lett. **69**, 2200 (1992).
- [68] J. Faure, Y. Glinec, A. Pukhov, S. Kiselev, S. Gordienko *et al.*, *A laser plasma accelerator producing monoenergetic electron beams*, Nature **431**, 541 (2004).

REFERENCES

- [69] A. Rousse, Kim Ta Phuoc, R. Shah, A. Pukhov, *et al.*, *Production of a keV X-Ray Beam from Synchrotron Radiation in Relativistic Laser-Plasma Interaction*, Phys. Rev. Lett. **93**, 135005 (2004).
G. Drenkhahn and H. C. Spruit, *Efficient acceleration and radiation in Poynting flux powered GRB outflows*, Astron. Astrophys. **391**, 1141 (2002).
- [70] H. Lesch and G. T. Birk, *Particle acceleration by magnetic field-aligned electric fields in active galactic nuclei*, Astron. Astrophys. **324**, 461 (1997).
T. di Matteo, *Magnetic reconnection: flares and coronal heating in active galactic nuclei*, Mon. Not. R. Astron. Soc. **299**, L15 (1998).
G. T. Birk, A. R. Crusius-Wätzel, and H. Lesch, *Hard Radio Spectra from Reconnection Regions in Galactic Nuclei*, Astrophys. J. **559**, 96 (2001).
- [71] Y. Sentoku, W. Kruer, M. Matsuoka, A. Pukhov, *Laser Hole Boring and Hot Electron Generation in the Fast Ignition Scheme*, Fusion Sci. Tech. Rep. **49**, 278 (2006).
- [72] LHC - The Large Hadron Colliders, CERN, Switzerland.
- [73] NASA - www.nasa.gov .
- [74] G. Drenkhahn, *Acceleration of GRB outflows by Poynting flux dissipation*, Astron. Astrophys. **387**, 714 (2002).
- [75] M. V. Medvedev and A. Loeb, *Generation of Magnetic Fields in the Relativistic Shock of Gamma-Ray Burst Sources*, ApJ **526**, 697, (1999).
- [76] B. D. Fried, *Mechanism for Instability of Transverse Plasma Waves*, Phys. Fluids **2**, 337 (1959).
- [77] P. Sprangle, E. Esarey, and J. Krall, *Laser driven electron acceleration in vacuum, gases, and plasmas*, Phys. Plasmas **3**, 2183 (1996).
- [78] A. I. Akhiezer and R. V. Polovin, *Theory of wave motion of an electron plasma*, Sov. Phys. JETP, **3**, 696 (1956).
- [79] J. M. Dawson, *Nonlinear electron oscillations in a cold plasma*, Phys. Rev. **113**, 383 (1959).
- [80] K. Nakajima, D. Fisher, T. Kawakubo, H. Nakanishi, A. Ogata, Y. Kato, Y. Kitagawa, R. Kodama, K. Mima, H. Shiraga, K. Suzuki, K. Yamakawa, T. Zhang, Y. Sakawa, T. Shoji, Y. Nishida, N. Yugami, M. Downer, and T. Tajima, *Observation of ultrahigh gradient electron acceleration by a self-modulated intense short laser pulse*, Phys. Rev. Lett. **74**, 4428 (1995).
- [81] C. E. Clayton, C. Joshi, C. Darrow, and D. Umstadter, *Relativistic plasma-wave excitation by collinear optical mixing*, Phys. Rev. Lett. **54**, 2343 (1985).

REFERENCES

- [82] C. Varin & M. Piche, *Acceleration of ultra-relativistic electrons using high intensity TM_{01} laser beams*, App. Phys., B **74** [suppl.], S83 - s88 (2002).
C. Varin, M. Piché, and M. A. Porras, *Acceleration of electrons from rest to GeV energies by ultrashort transverse magnetic laser pulses in free space*, Phys. Rev. E **71**, 026603 (2005).
C. Varin and M. Piché, *Relativistic attosecond electron pulses from a free-space laser-acceleration scheme*, Phys. Rev. E **74**, 045602 (2006).
- [83] O. Shorokhov, A. Pukhov, *Ion acceleration in overdense plasma by short laser pulse*, Laser Part. Beams **22**, 175 (2004).
- [84] S. P. D. Mangles, C. D. Murphy, Z. Najmudin *et al*, *Monoenergetic beams of relativistic electrons from intense laser-plasma interactions*, Nature **431**, 535 (2004).
- [85] C. G. R. Gedder, Cs. Toth, J. Van. Tilborg *et al.*, *High-quality electron beams from a laser wakefield accelerator using plasma-channel guiding*, Nature **431**, 538 (2004).
- [86] Y. Glinec, J. Faure, A. Pukhov, S. Kiselev, S. Gordienko, B. Mercier & V. Malka, *Generation of quasi-monoenergetic electron beams using ultrashort and ultraintense laser pulses*, Laser Part. Beams **23**, 161 (2005).
- [87] L. Yin, B. J. Albright, B. M. Hegelich, & J. C. Fernandez, *GeV laser ion acceleration from ultrathin targets: The laser break-out afterburner*, Laser Part. Beams **24**, 291 (2006).
- [88] K. Koyama, M. Adachi, E. Miura, S. Kato, S. Masuda, T. Watanabe, *Monoenergetic electron beam generation from a laser-plasma accelerator*, Laser Part. Beams **24**, 95 (2006).
- [89] A. F. Lifschitz, J. Faure, Y. Glinec, V. Malka & P. Mora, *Proposed scheme for compact GeV laser plasma accelerator*, Laser Part. Beams **2004**, 255 (2006)
- [90] A. R. Bell, *Computational Simulation of Plasmas*, Astrophysics and Space Sciences **256**, 13 (1998).
- [91] C. K. Birdsall, A. B. Langdon, *Plasma Physics Via Computer Simulation*, (Adam Higer, 1991).
- [92] R. W. Hockney, J. W. Eastwood, *Computer Simulation Using Particles*, (McGraw-Hill, London 1981).
- [93] J. M. Dawson, *One-dimensional plasma model*, Phys. Fluids, **5**, 445 (1962).
- [94] K. Yamakawa, Y. Akahane, Y. Fukuda, M. Aoyama, N. Inoue and H. Ueda, *Ionization of many-electron atoms by ultrafast laser pulses with peak intensities greater than 10^{19} W/cm²*, Phys. Rev. A **68**, 065403 (2003).

REFERENCES

- [95] A. Pukhov, *Three-dimensional electromagnetic relativistic particle-in-cell code VLPL (Virtual Laser Plasma Lab)*, J. Plasma Phys. **61**, 425 (1999).
- [96] R. A. Fonseca, L. O. Silva, F. S. Tsung *et al.*, *OSIRIS: A Three-Dimensional, Fully Relativistic Particle in Cell Code for Modeling Plasma Based Accelerators*, Lecture Notes in Computer Science **2331** 342, (2002).
- [97] C. Nieter, J. R. Cary, *VORPAL: a versatile plasma simulation code*, J. Comput. Phys. **196**, 448 (2004).
- [98] J. P. Verboncoeur, A. B. Langdon, N. T. Gladd, *An object-oriented electromagnetic PIC code*, Comput. Phys. Commun. **87**, 199-211 (1995).
- [99] J. P. Verboncoeur, *Particle simulation of plasmas: review and advances*, Plasma Phys. Control. Fusion **47** A231 (2005).
- [100] C. Huang, V. K. Decyk, C. Ren, M. Zhou, W. Lu, W. B. Mori, J. H. Cooley, T. M. Antonsen Jr., T. Katsouleas, *QUICKPIC: A highly efficient particle-in-cell code for modeling wakefield acceleration in plasmas*, J. Comp. Phys. **217**, 658 (2006).
- [101] Ch. Karle, J. Schweitzer, M. Hochbruck, E. Laedke and K. H. Spatschek, *Numerical solution of nonlinear wave equations in stratified dispersive media*, J. Comp. Phys. **216**, 138 (2006).
- [102] R. Lee and M. Lampe, *Electromagnetic Instabilities, Filamentation, and Focusing of Relativistic Electron Beams*, Phys. Rev. Lett. **31**, 1390 (1973).
- [103] M. Honda, J. Meyer-ter-Vehn, and A. Pukhov, *Two-dimensional particle-in-cell simulation for magnetized transport of ultra-high relativistic currents in plasma*, Phys. Plasmas **7**, 1302 (2000).
- [104] T. Okada and K. Ogawa, *Saturated magnetic fields of Weibel instabilities in ultraintense laser-plasma interactions*, Phys. Plasmas **14**, 072702 (2007).
- [105] A. Pukhov and J. Meyer-ter-Vehn, *Relativistic Magnetic Self-Channeling of Light in Near-Critical Plasma: Three-Dimensional Particle-in-Cell Simulation*, Phys. Rev. Lett. **76**, 3975 (1996).
- [106] A. Pukhov and J. Meyer-ter-Vehn, *Laser Hole Boring into Overdense Plasma and Relativistic Electron Currents for Fast Ignition of ICF Targets*, Phys. Rev. Lett. **79**, 2686 (1997).
- [107] Y. Sentoku, K. Mima, P. Kaw and K. Nishikawa, *Anomalous Resistivity Resulting from MeV-Electron Transport in Overdense Plasma*, Phys. Rev. Lett. **90**, 155001 (2003).

REFERENCES

- [108] R. Jung, J. Osterholz, K. Löwenbrück, *et al.*, *Study of Electron-Beam Propagation through Preionized Dense Foam Plasmas*, Phys. Rev. Lett. **94**, 195001 (2005).
- [109] M. Tatarakis, F. N. Beg, E. L. Clark, *et al.*, *Propagation Instabilities of High-Intensity Laser-Produced Electron Beams*, Phys. Rev. Lett. **90**, 175001 (2003).
- [110] M. Wei, F. N. Beg, E. L. Clark, *et al.*, *Observations of the filamentation of high-intensity laser-produced electron beams*, Phys. Rev. E **70**, 056412 (2004).
- [111] L. O. Silva, R. A. Fonseca, J. W. Tonge, W. B. Mori, and J. M. Dawson, *On the role of the purely transverse Weibel instability in fast ignitor scenarios*, Phys. Plasmas, **9**, 2458, (2002).
- [112] P. H. Yoon and R. C. Davidson, *Exact analytical model of the classical Weibel instability in a relativistic anisotropic plasma*, Phys. Rev. **A35**, 2718, (1987).
- [113] F. Califano, F. Pegoraro and S. V. Bulanov, *Spatial structure and time evolution of the Weibel instability in collisionless inhomogeneous plasmas*, Phys. Rev. E **56**, 963 (1997).
- [114] M. Honda, *Eigenmodes and growth rates of relativistic current filamentation instability in a collisional plasma*, Phys. Rev. E **69**, 016401 (2004).
- [115] A. Bret, M.-C. Firpo and C. Deutsch, *Collective electromagnetic modes for beam-plasma interaction in the whole k space*, Phys. Rev. E **70**, 046401 (2004);
A. Bret, M.-C. Firpo and C. Deutsch, *Characterization of the Initial Filamentation of a Relativistic Electron Beam Passing through a Plasma*, Phys. Rev. Lett. **94**, 115002 (2005),
A. Bret, M.-C. Firpo and C. Deutsch, *Between two stream and filamentation instabilities: Temperature and collisions effects*, Laser Part. Beams, **24**, 27 (2006).
- [116] M. Honda, J. Meyer-ter-Vehn and A. Pukhov, *Collective Stopping and Ion Heating in Relativistic-Electron-Beam Transport for Fast Ignition*, Phys. Rev. Lett. **85**, 2128, (2000).
- [117] J. J. Honrubia and J. Meyer-ter-Vehn, *Three-dimensional fast electron transport for ignition-scale inertial fusion capsules*, Nucl. Fusion, **46**, L-25 (2006).
- [118] F. Califano, D. Del Sarto and F. Pegoraro, *Three-Dimensional Magnetic Structures Generated by the Development of the Filamentation (Weibel) Instability in the Relativistic Regime*, Phys. Rev. Lett. **96**, 105008 (2006).
- [119] O. Polomarov, A. B. Sefkow, I. Kaganovich and G. Schvets, *Computationally efficient description of relativistic electron beam transport in collisionless plasma*, Phys. Plasmas **14**, 043103, (2007).

REFERENCES

- [120] P. B. Corkum, *Plasma perspective on strong-field multiphoton ionization*, Phys. Rev. Lett. **71**, 1994 (1993).
- [121] T. Ditmire, *Simulations of heating and electron energy distributions in optical field ionized plasmas*, Phys. Rev. E **54**, 6735 - 6740 (1996).
- [122] D. L. Bruhwiler and D. A. Dimitrov, J. R. Cary, E. Esarey, W. Leemans and R. E. Giacone, *Particle-in-cell simulations of tunneling ionization effects in plasma-based accelerators*, Phys. Plasmas **10**, 2022 (2003).
- [123] M. Chen, Z-M. Sheng, Y-Y. Ma, and J. Zhang, *Electron injection and trapping in a laser wakefield by field ionization to high-charge states of gases*, J. Appl. Phys. **99**, 056109 (2006).
- [124] C. I. Moore, A. Ting, T. Jones, E. Briscoe, B. Hafizi, R. F. Hubbard, and P. Sprangle, *Measurements of energetic electrons from the high-intensity laser ionization of gases*, Phys. Plasmas **8**, 2481 (2001).
- [125] M. Hegelich, S. Karsch, G. Pretzler, D. Habs, K. Witte¹, W. Guenther, M. Allen, A. Blazevic, J. Fuchs, J. C. Gauthier, M. Geissel, P. Audebert, T. Cowan, and M. Roth, *MeV Ion Jets from Short-Pulse-Laser Interaction with Thin Foils*, Phys. Rev. Lett. **89**, 085002 (2002).
- [126] B. H. Failor, J. C. Fernandez, B. H. Wilde, A. L. Osterheld, J. A. Cobble and P. L. Gobby, *Hot, dense, millimeter-scale, high-Z plasmas for laser-plasma interactions studies*, Phys. Rev. E **59**, 6053 (1999).
- [127] S. Kawata, Q. Kong, S. Miyazaki, K. Miyauchi *et al.*, *Electron bunch acceleration and trapping by ponderomotive force of an intense short-pulse laser*, Laser Part. Beams **23**, 61-67 (2005).
- [128] T. A. Carlson, C. W. Nestor, Jr, N. Wasserman and J. D. McDowell, *Calculated ionization potentials for multiply charged ions*, Atomic Data **2**, 63 - 69, (1970).
- [129] S. X. Hu and A. F. Starace, *GeV Electrons from Ultraintense Laser Interaction with Highly Charged Ions*, Phys. Rev. Lett. **88**, 245003 (2002).
- [130] S. X. Hu and A. F. Starace, *Laser acceleration of electrons to giga-electron-volt energies using highly charged ions*, Phys. Rev. E **73**, 066502 (2006).
- [131] A. Karmakar, N. Kumar, A. Pukhov, and G. Shvets, *On collisions driven negative energy waves and Weibel instability of a relativistic electron beam in a quasi-neutral plasma*, to be submitted, (2008).
- [132] Cadjan and Ivanov, *Langevin approach to plasma kinetics with Coulomb collisions*, J. Plasma Phys. **61**, 89 (1999).

REFERENCES

- [133] C. K. Birdsall, *Particle-in-cell charged-particle simulations, plus monte carlo collisions with neutral atoms, pic-mcc*, IEEE Trans. Plasma Sci. **19**, 65 (1991).
- [134] D. L. Bruhwiler, R. E. Giacone, J. R. Cary *et al.*, *Particle-in-cell simulations of plasma accelerators and electron-neutral collisions*, Phys. Rev. ST Accel. Beams, **4**, 101302 (2001).
- [135] Takizuka and Abe, *A binary collision model for plasma simulation with a particle code*, J. Comp. Phys. **25**, 205 (1977).
- [136] D. J. Larson, *A Coulomb collision model for PIC plasma simulation*, J. Comp. Phys. **188**, 123 (2003).
- [137] S. Ma, R. D. Sydora and J. M. Dawson, *Binary collision model in gyrokinetic simulation plasmas*, Comp. Phys. Comm. **77**, 190 (1993).
- [138] M. E. Jones *et al.*, *A Grid-Based Coulomb Collision Model for PIC Codes*, J. Comp. Phys. **123**, 169 (1996).
- [139] C. D. Decker, W. B. Mori, J. M. Dawson and T. Kotsouleas, *Nonlinear collisional absorption in laser-driven plasmas*, Phys. Plasmas **1**, 4043 (1994).
- [140] V. P. Silin, *Interaction of a Strong High Frequency Electromagnetic Field Within a Plasma*, Sov. Phys.-JETP **20**, 1510 (1965).
- [141] G. Shvets and N. J. Fisch, *Electron-ion collisions in intensely illuminated plasmas*, Phys. Plasmas **2**, 428 (1997).
- [142] J. P. Verboncoeur, *Particle simulation of plasmas: review and advances*, Plasma Phys, Control. Fusion **47**, A231 (2005).
- [143] S. Pflanzner and P. Gibbon, *Many Body Tree Methods* (Cambridge, 1996).
- [144] R. P. J. Town and A. R. Bell, *Fokker-Planck simulations of short-pulse-laser solid experiments*, Phys. Rev. **E 50**, 1413 (1994).
- [145] W. L. Kruer, *The Physics of Laser Plasma Interactions*, Addison-Wesley, Redwood City (1988).
- [146] C. G. R. Geddes, Cs. Toth, J. van Tilborg *et al.*, *High-quality electron beams from a laser wakefield accelerator using plasma-channel guiding*, Nature **431**, 538 (2004).
- [147] J. Faure, C. Rechatin, A. Norlin, A. Lifschitz *et al.*, *Controlled injection and acceleration of electrons in plasma wakefields by colliding laser pulses*, Nature **444**, 737 (2006).
- [148] S. Bastiani, A. Rousse, J. P. Geindre *et al.*, *Experimental study of the interaction of subpicosecond laser pulses with solid targets of varying initial scale lengths*, Phys. Rev. **E 56**, 7179 (1997).

REFERENCES

- [149] L. M. Chen, J. Zhang, Y. T. Li, *et al.*, *Effects of Laser Polarization on Jet Emission of Fast Electrons in Femtosecond-Laser Plasmas*, Phys. Rev. Lett. **87**, 225001 (2001).
- [150] Y. T. Li, X. H. Yuan, M. H. Xu, Z. Y. Zheng *et al.*, *Observation of a Fast Electron Beam Emitted along the Surface of a Target Irradiated by Intense Femtosecond Laser Pulses*, Phys. Rev. Lett. **96**, 165003 (2006).
- [151] J. Osterholz, F. Brandl, T. Fischer *et al.*, *Production of Dense Plasmas with sub-10-fs Laser Pulses*, Phys. Rev. Lett. **96**, 085002 (2006).
- [152] M. E. Riley, C. J. MacCallum and F. Biggs, *Theoretical electron-atom elastic scattering cross sections : Selected elements, 1 keV to 256 keV*, At. Data Nucl. Data Tab. **15**, 444 (1975).
- [153] M. Tabak, J. H. Hammer, M. E. Glinsky *et al.*, *Ignition and high gain with ultra-powerful lasers*, Phys. Plasmas **1**, 1626 (1994).
- [154] R. J. Mason, *Monte Carlo hybrid modeling of electron transport in laser produced plasmas*, Phys. Fluids **23** 2204 (1980).
- [155] P. W. Rambo and J. Denavit, *Fluid and field algorithms for time-implicit plasma simulation*, J. Comp. Phys. **92**, 185 (1991).
- [156] P. W. Rambo and J. Denavit, *Interpenetration and ion separation in colliding plasmas*, Phys. Plasmas **1**, 4050 (1994).
- [157] J. R. Davies, A. R. Bell, M. G. Haines, and S. Guerin, *Short-pulse high-intensity laser-generated fast electron transport into thick solid targets*, Phys. Rev. E **56**, 7193 (1997).
- [158] L. Gremillet, G. Bonnaud, F. Amiranoff, *Filamented transport of laser-generated relativistic electrons penetrating a solid target*, Phys. Plasmas **9**, 941 (2002).
- [159] D. W. Hewett, *Elimination of electromagnetic radiation in plasma simulation: The Darwin or magneto inductive approximation*, Space Sc. Rev., **42**, 29 (1985).
- [160] D. R. Welch, D. V. Rose, R. E. Clark *et al.*, *Implementation of a non-iterative implicit electromagnetic field solver for dense plasma simulation*, Comput. Phys. Commun., **164**, 183 (2004).
- [161] F. Zheng, Z. Chen, *Numerical dispersion analysis of the unconditionally stable 3-DADI-FDTD method*, IEEE Trans. Microwave Theory Tech. **49** 1006 (2001).
- [162] G. H. Golub, C. Van L., *Matrix Computations*, (Johns Hopkins University Press, 3rd edition 1996).
- [163] N. Kumar, A. Pukhov, *New class of self-similar solutions for vacuum plasma expansion admitting monoenergetic ion spectra*, Phys. Plasmas, **in press** (2008).

REFERENCES

- [164] K. Molvig, *Filamentary Instability of a Relativistic Electron Beam*, Phys. Rev. Lett. **35**, 1504, (1975).
- [165] R. J. Briggs, *Advances in Plasma Physics*, Vol.4, Interscience, p-43 (1971).
- [166] H. S. Pécseli, *Instability caused by dissipation in plasmas carrying negative energy waves*, Plasma Phys., **17**, 493 (1975).
- [167] M. V. Nezlin, *Physics of Intense Beams in Plasmas*, IOP Publishing, p-62 (1993).
- [168] J. M. Dawson, *Particle simulation of plasmas*, Rev. Mod. Phys. **55**, 403 (1983).
- [169] J. Villasenor, O. Buneman, *Rigorous charge conservation for local electromagnetic field solvers*, Comp. Phys. Commn., **69**. 306 (1992).
- [170] Texas Advanced Computing Center - <http://www.tacc.utexas.edu> .

List of Publications

Published in Journal

- Jalo Liljo, Anupam Karmakar, A. Pukhov, M. Hochbruck, *One dimensional electromagnetic relativistic PIC-hydrodynamic hybrid simulation code H-VLPL (Hybrid Virtual Laser Plasma Lab)*, Comp. Phys. Commun. **article in press**, published online, DOI:10.1016/j.cpc.2008.03.008 (2008).
- A. Karmakar and A. Pukhov, *Collimated attosecond GeV electron bunches from ionization of high-Z material by radially polarized ultra-relativistic laser pulses*, Laser and Particle Beams **25**, 371, (2007).
- H.A. Sumeruk, S. Kneip, D. Symes, I. Churina, A. Belolipetski, G. Dyer, J. Landry, G. Bansal, A. Bernstein, T. Donnelly, A. Karmakar, A. Pukhov and T. Ditmire, *Hot electron and x-ray production from intense laser irradiation of wavelength-scale polystyrene spheres*, Phys. Plasmas **14**, 062704 (2007).
- M. R. Gupta, B. Roy, A. Karmakar, S. Sarkar, M. Khan, *A combined effect of secondary electron emission, plasma ion and electron number density variation due to charging and ionization-recombination processes on Dust Ion Acoustic Wave Propagation*, Physica Scripta **71**, 298 (2005).
- M. R. Gupta, B. Roy, A. Karmakar, S. Sarkar, M. Khan, *Effect of Secondary Electron on the Propagation of Dust Acoustic Wave in Dusty Plasma*, Phys. Plasmas **11**, 1850 (2004).

Under Review and Submitted to Journal

- F. Brandl, B. Hidding, J. Osterholz, D. Hemmers, A. Karmakar, A. Pukhov and G. Pretzler, *Directed acceleration of electrons from a solid surface by sub-10-fs laser pulses*, Phys. Rev. Lett. **under review**, April, (2008).
- B. I. Cho, J. Osterholz, A. C. Bernstein, G. M. Dyer, A. Karmakar, A. Pukhov, and T. Ditmire, *Observation of two distinct hot electron beams in intense laser-solid interactions*, Phy. Rev. Lett. **submitted**, April, (2008).
- Anupam Karmakar, Naveen Kumar, A. Pukhov, and G. Shvets, *On collision induced negative energy waves and Weibel instability of a relativistic electron beam in quasi-neutral plasma*, Phy. Rev. Lett. **submitted**, May, (2008).

Under Preparation

- Anupam Karmakar, Naveen Kumar, A.Pukhov, and G. Shvets, *Effects of collisions and temperature on the transport of a relativistic electron beam in Fast Ignition (FI) plasmas*, **under preparation**, (2008).

Acknowledgment

Any successful work is never a solitary pursuit. It requires input from several people in myriad aspects. My PhD is no exception. It is thus a pleasure to acknowledge the help and support of the many people that I owe my thanks to for making this PhD thesis possible.

I would like to begin by thanking my supervisor Prof. Alexander Pukhov for giving me the opportunity to work in his group and guiding me through the often intense debates and tangles of plasma physics research, and for always having an open door when I needed help and advice. This PhD has been a milestone in my life, and the thesis would have never been conceived let alone being achieved without his sound advice, wide understanding, bold suggestions, critical comments and constant encouragement.

I am also grateful to Prof. K. H. Spatschek for extending the organisational support throughout the duration of my research work and fruitful scientific discussions.

The financial support of DFG–Sonderforschungsbereich Transregio 18 is gratefully acknowledged. I would like to thank Prof. M. Hochbruck for scientific discussions and her remarkable leadership of the project TR-18 B5 together with Prof. Pukhov.

My PhD also owes a great deal to Prof. Gennady Shvets of University of Texas at Austin, for inviting me to visit his institute and work in collaboration with his group.

My family has been the bedrock upon which I have built so much in my life, and if it was not for their love and constant support, I would have never been able to complete my PhD. With utmost regard and affection I dedicate this thesis to my parents. It is only their love and care that kept me motivated during the long spells away from home. I would also like express my gratitude to my sisters Anusree and Tanusree, and my brother-in-law Uttam Karmakar for their encouragement whenever I felt low.

Furthermore, without a dedicated team of friends, life as a PhD student can be very intimidating, and so I am duty-bound to thank (amongst others) Souvik and Susmita Prasad, Dr. S. P. Das, Pratyush Bhartiya and Sabyasachi Bagchi. A special word of thank has to be said for Dr. (Med.) Sujal Ghosh for being unconditionally supportive and making sure I did have a life outside work during the last three years.

I would also like to kindly acknowledge Frau Elvira Gröters for her efficient management of all official formalities and the ever welcoming personality. She has always been my inspiration to learn German. I also take this opportunity to thank Mr. E. Zügge for taking care of all my needs of computer hardware and software. Their friendliness and warm attitude always contributed to a homely atmosphere in the Institute.

Since this thesis has been an inter-disciplinary research work with inputs from not only my own group but from other quarters at the school as well, I cannot finish without mentioning the academic discussions with Daniel an der Brügge, Dr. Naveen Kumar and Jalo Liljo which helped me enrich my understanding about the subject and the

research work. In addition to this, I would like to specially thank Mr. an der Brügge for helping me proof-read this thesis. Teodora Baeva needs to be thanked specially for being supportive on all matters right from the early days in the institute. Whilst it has been fun to share the office with Vasily Seredov, it has also been a great learning experience to work with colleagues Götz Lehmann and Dr. Christoph Karle for their expertise on Linux systems.

Finally, I am eternally indebted to my fiancé Piya Sarker, to whom I owe more than I can possibly describe here. I feel extremely lucky in life to have her besides me: she was happy for me when I did well, and pulled me up when I was felt low. What can I say, thank you very much for being there for me ... through the thick and the thin ... whenever, forever.

Anupam Karmakar
Düsseldorf, May 2008

Erklärung

Hiermit erkläre ich, vorliegende Dissertation selbstständig verfaßt, keine anderen als die angegebenen Quellen und Hilfsmittel benutzt, sowie Zitate kenntlich gemacht zu haben.

Düsseldorf, den

Index

- acceleration
 - electron
 - collision, 57
 - directed, 57
 - scattering, 57
 - atomic field strength, 16
- barrier suppression (BSI), 16
- basic PIC equations, 113
- basic plasma physics, 16
- beam propagation, 15
- betatron frequency, 24
- bubble regime, 27
- bubble scaling laws, 27
- cloud-in-cell (CIC), 70
- collision, 12, 51
 - algorithm, 51
 - implementation, 51
- binary, 51
- electron beam, 55
- module
 - benchmarking, 55
 - implementation, 52
- Courant algorithm, 67
- Darwin approximation, 67
- Debye length, 19
- direct laser acceleration, 24
- dispersion relation, 75
 - x-component, 75
 - y and z-component, 76
- electron acceleration
 - radially polarized pulse, 37
- electron bunches
 - collimated attosecond, 36
- electron phase space, 84
- Fast-Ignition, 28
- fluid simulations, 14
- H-VLPL, 12, 67
 - benchmarking, 79
 - collisional absorption, 86
 - energy conservation, 80
 - reflection & refraction, 80
 - skin fields, 84
 - TNSA, 82
 - numerical method, 70
 - overview, 68
- hot electron, 45
- hybrid
 - electron, 69
 - ion, 69
 - particles, 69
- hybrid code, 67
 - particle-fluid, 67
- hybrid model, 69
- ionization, 12, 16
 - ADK formula, 33
 - high-Z material, 36
 - implementation, 33
 - tunnel ionization, 33
- kinetic simulations, 14
- laser
 - beam
 - radially polarized, 37
 - beam
 - radially polarized, 36
- Laser wakefield acceleration, 26

- LWFA, 26
- MHD, 69
- Nearest Grid Point (NGP), 70
- numerical simulations, 14
- optical field ionization (OFI), 16
- particle
 - motion, 20
 - motion equation, 113
- particle acceleration, 13
 - mechanism, 24
- Particle-in-cell, 113
- PIC, 113
- PIC codes, 14
- PIC-MCC, 51
- plasma frequency, 19
- polystyrene spheres, 45

- quasi-monoenergetic spectrum, 27

- relativistic threshold, 20

- simulation
 - electron acceleration, 37
 - laser droplet interaction, 45
 - Weibel
 - 2D, 89
 - 3D, 89, 104
- simulation code
 - H-VLPL, 67
 - PIC-Hydrodynamic, 67
 - VLPL, 67
- simulation details, 92
- SM-LWFA, 26

- thesis
 - motivation, 11
 - overview, 12
- tunneling ionization, 16
- two-stream instability, 28

- VLPL, 113, 115

- Weibel
 - instability, 15, 28, 89
 - analytical theory, 105
 - longitudinal simulation geometry, 90
 - results
 - 3D geometry, 104
 - longitudinal geometry, 98
 - transverse geometry, 92
 - simulation, 92, 98, 104
 - simulation models, 90
 - transverse geometry, 90
- Weibel geometry, 92